Investigation of HF-based Electrochemical Etching Solutions for Porous Silicon

Von der Naturwissenschaftlichen Fakultät
der Gottfried Wilhelm Leibniz Universität Hannover

zur Erlangung des Grades
DOKTORIN DER NATURWISSENSCHAFTEN
– Dr. rer. nat. –

genehmigte Dissertation von

Dipl. Chem. Julia-Beatrix Nehmann
geboren am 17.09.1983 in Hannover

2014

Referent: Prof. Dr. Detlef W. Bahnemann
Korreferent: Prof. Dr. Rolf Brendel
Tag der Promotion: 15.10.2014

INVESTIGATION OF HF-BASED ELECTROCHEMICAL ETCHING SOLUTIONS FOR POROUS SILICON

In this thesis, the behavior of electrolytes is investigated that are used for the electrochemical processing of porous silicon (Si) at the Institute for Solar Energy Research Hamelin (ISFH). The investigated electrolytes consist of aqueous hydrofluoric acid ($HF_{(aq)}$) and an organic wetting agent, whereas the reaction product hexafluorosilicic acid (H_2SiF_6) enriches in the electrolyte with increasing etching processes. Mesoporous Si is used in the PSI process as a base for a modern concept for the fabrication of Si solar cells with a thickness below 100 µm, while macroporous Si can be used as an absorber layer in a different concept for solar cells (MacPSI).

In the technical part of this thesis, chemical analysis methods are evaluated concerning their applicability and are employed on the PSI as well as on the MacPSI etching bath. The focus is on the reliability of the methods in the presence of high HF concentrations, and, in addition, on the practicability for industrial processes. The methods that are investigated in the context of this work are the precipitation titration with lanthanum nitrate as well as the fluoride ion-selective electrode that are both used for the determination of the HF concentration. The concentrations of the wetting agents ethanol and acetic acid are performed with the commercially available cuvette test method. The analysis of the reaction product H_2SiF_6 is challenging since only traces exist in the electrolyte and the determination is disturbed by the presence of HF. However, the determination with ion-chromatography is possible, if the system is equipped with a post-column derivatization device and an ion-exclusion column is used.

The application of the chemical analysis methods on the PSI etching bath leads to the possibility of replenishing the electrolyte. Thus, the usability is raised from about 250 etched wafers to more than 700 wafers. Moreover, it is found that the wetting agent is oxidized during the etching process and is thus consumed. It is required to balance this loss by appropriate replenishment in order to prevent an abbreviated bath lifetime of the electrolyte.

In the chemical part of this thesis, the PSI electrolyte is investigated concerning the surface tension, the viscosity, the density, and the ability to permeate through porous Si as a function of the remaining ethanol concentration. With these, the size of hydrogen bubbles is estimated that form during the etching process on the Si surface. These bubbles are presumably critical for the homogeneous formation of the separation layer in the mesoporous Si. In addition, the effect of the enrichment of H_2SiF_6 is investigated concerning the PSI etching bath. It is investigated if H_2SiF_6 is able to dissolve porous Si. Furthermore, the effect of the rising concentration of the reaction product is discussed in terms of the electrochemical reactions of the etching processes investigated in this work.

KEYWORDS

Electrochemical etching process, technical aspects, thin film silicon solar cells.

UNTERSUCHUNGEN VON HF-BASIERTEN ELEKTROCHEMISCHEN ÄTZLÖSUNGEN FÜR DAS POROSIZIEREN VON SILICIUM

In dieser Arbeit wird das Verhalten von Elektrolyten näher untersucht, die zur elektrochemischen Herstellung von porösem Silicium (Si) am Institut für Solarenergieforschung Hameln (ISFH) verwendet werden. Die untersuchten Elektrolyte bestehen aus wässriger Flusssäure ($HF_{(aq)}$) und einem organischen Benetzungsmittel, wobei sich mit zunehmenden Ätzprozessen das Reaktionsprodukt Siliciumhexafluorid (H_2SiF_6) im Elektrolyten anreichert. Mesoporöses Si dient im PSI Prozess als Basis für ein modernes Konzept für die Herstellung von Si-Solarzellen mit einer Dicke von weniger als 100 µm, während makroporöses Si als Absorberschicht in einem anderen Solarzellenkonzept verwendet werden kann (MacPSI).

Im technischen Teil dieser Arbeit werden chemische Analysemethoden auf ihre Eignung evaluiert und auf das PSI sowie das MacPSI Ätzbad angewendet. Der Schwerpunkt liegt dabei sowohl in der Beständigkeit der Methoden gegenüber der hohen HF-Konzentration, als auch in der Integrierfähigkeit in industrielle Abläufe. Die im Rahmen dieser Arbeit untersuchten Methoden sind die Fällungstitration mit Lanthannitrat sowie die Fluorid-Ionenselektive Elektrode, die beide für die Bestimmung von HF untersucht werden. Die Konzentrationen der Benetzungsmittel Ethanol und Essigsäure werden mit der kommerziell erhältlichen Küvettentestmethode bestimmt. Anspruchsvoll ist die Analyse des Reaktionsproduktes H_2SiF_6, da es nur in Spuren vorhanden ist und die Bestimmung durch die Anwesenheit von HF gestört wird. Eine Bestimmung mit Ionenchromatographie ist jedoch möglich, wenn das System über eine Nachsäulenderivatisierungseinheit verfügt und eine Anionenausschlusssäule verwendet wird.

Die Anwendung der Analysemethoden auf das PSI Ätzbad haben dazu geführt, dass der Elektrolyt nachdosiert werden konnte und die Verwendbarkeit von etwa 250 geätzten Wafern auf mehr als 700 Wafer gesteigert werden konnte. Ferner hat sich herausgestellt, dass das Benetzungsmittel während des Ätzprozesses oxidiert und damit verbraucht wird. Dieser Verlust muss durch geeignetes Nachdosieren ausgeglichen werden um eine Verkürzung der Badlebensdauer zu verhindern.

Im chemisch orientierten Teil der Arbeit werden die Oberflächenspannung, die Viskosität, die Dichte und die Fähigkeit zur Durchdringung von porösem Si in Abhängigkeit von der verbliebenden Ethanolkonzentration im PSI Elektrolyten experimentell bestimmt. Diese werden zur Abschätzung der Größe der Wasserstoffbläschen herangezogen, die sich während des Ätzprozesses auf der Si-Oberfläche bilden; sie sind wahrscheinlich kritisch für die homogene Ausbildung der Trennschicht im porösen Si. Außerdem wird die Auswirkung der Anreicherung von H_2SiF_6 auf das PSI Ätzbad diskutiert indem untersucht wird, ob H_2SiF_6 in der Lage ist poröses Si aufzulösen. Darüber hinaus wird der Einfluss der Anreicherung von H_2SiF_6 auf die elektrochemischen Reaktionen der hier betrachteten Ätzprozesse behandelt.

SCHLAGWORTE

Elektrochemischer Ätzprozess, technische Aspekte, Dünnschicht-Solarzellen aus Silicium.

LIST OF SYMBOLS AND CONSTANTS

The following symbols and constants are used in this work.

Symbol	Unit	Description
a	-	Activity of ion in sample
A	cm^2	Etching area
δ	-	Constrictivity
d	µm	Thickness
D	$cm^2\ s^{-1}$	Diffusion coefficient
D_e	$cm^2\ s^{-1}$	Effective diffusion coefficient
ε_t	%	Porosity (available for transport)
e	$1.602 \cdot 10^{-19}$ C	Elementary charge
E	mV	Measured potential
E^0	mV	Standard electrode potential
F	$96485\ C\ mol^{-1}$	Faraday's constant
g	$9.81\ m\ s^{-2}$	Gravitation constant
$\Delta_R G^0$	$kJ\ mol^{-1}$	Gibbs energy
η	mPa s	Dynamic viscosity
h	m	Height of liquid in a capillary tube
ΔH	$kJ\ mol^{-1}$	Enthalpy
θ	°	Contact angle
J	$mA\ cm^{-2}$	Current density
k_B	$1.380658 \cdot 10^{-23}\ J\ K^{-1}$	Boltzmann constant
K	e.g. $mol\ l^{-1}$	Equilibrium constant
m	g	Mass
M	$g\ mol^{-1}$	Molar mass
M_{Si}	$28.0855\ g\ mol^{-1}$	Molar mass of silicon
M_{HF}	$20.01\ g\ mol^{-1}$	Molar mass of HF
ν	$m\ s^{-1}$	Velocity
n	-	Valence
N_A	$6.022 \cdot 10^{23}\ mol^{-1}$	Avogadro's constant

Symbol	Unit	Parameter
P	%	Porosity
Q	C	Electric charge
R	m	Radius
R	8.3145 J mol^{-1} K^{-1}	Universal gas constant
R_R	%	Recovery rate
R_0	m	Hydrodynamic radius
ρ	kg m^{-3}	Density
ρ_{Si}	2336 kg m^{-3}	Density of silicon
σ	N m^{-1}	Surface tension
τ	-	Tortuosity
t	s	Time
T	K	Temperature
V	l mol^{-1}	Volume
V_{mol}	22.41 l	Molar volume
z	-	Charge of ion

CONTENT

1 POROUS SILICON IN PHOTOVOLTAICS

Cost reduction in photovoltaic (PV) solar cells is still an important issue for industry and researchers. In recent years, the cost of PV modules has decreased drastically in Germany. This is, on the one hand, a result of the energy policy of the German government, and, on the other hand, due to the increased PV module production especially in Asia. Most PV modules are made from crystalline silicon (Si) wafers having the advantage of unrestricted resources. Thus, many modern concepts for Si solar cells deal particularly with the cost reduction of the production from which the material costs of Si are crucial.

Usually a Si ingot is cut into wafers by wire sawing. The wafers have a target thickness between 300-700 µm depending on the aspired Si cell process. The sawing process provokes a considerable loss of Si material due to the width of the saw. Therefore, kerfless methods, i.e., methods that require no sawing, are investigated as an alternative process for the production of thin Si solar cells reducing the loss of material. These thin Si solar cells have a thickness below 100 µm. The reduction of the Si cell thickness is further promoted by the fact that the Si wafer accounts for 57% of the Si cell production cost [1].

Promising approaches to kerfless technology are the layer transfer processes that include the re-use of a Si substrate wafer, some of which are the VEST approach at Mitsubishi, the ELTRAN process developed at Canon, or the SPS process from Sony and the University of Stuttgart [2]. The ISFH focuses on the porous silicon (PSI) as a kerfless technology for many years now and has gained considerable attention from research and industry [3–5]. The potential of the PSI process is demonstrated through the appreciable solar cells with an efficiency of 19.1% processed at the ISFH in 2012 as well as the recently reported efficiency of 20.1% from Solexel, both have a thickness of only 43 µm [4,6]. At ISFH, another approach in kerfless technology is the macroporous silicon (MacPSI) process that involves macroporous Si as an absorber layer with a thickness of about 30 µm for solar cells [7–9]. Cell efficiencies of up to 13.1% were achieved with an additional epitaxial layer at ISFH [10].

The following chapter introduces the PSI process exemplary for the application of porous Si layers in PV. The challenges that arise from this modern concept for the production of Si solar cells from kerfless technologies demonstrate the options and advantages provided by chemical analysis.

1.1 THE PSI PROCESS

Independently from one another, Brendel and Tayanaka have developed the idea of a manifold re-usable Si substrate in the 90ths of the last century [11–13]. On this basis, the ISFH has established the PSI process, the schematic representation of which is illustrated in Figure 1.

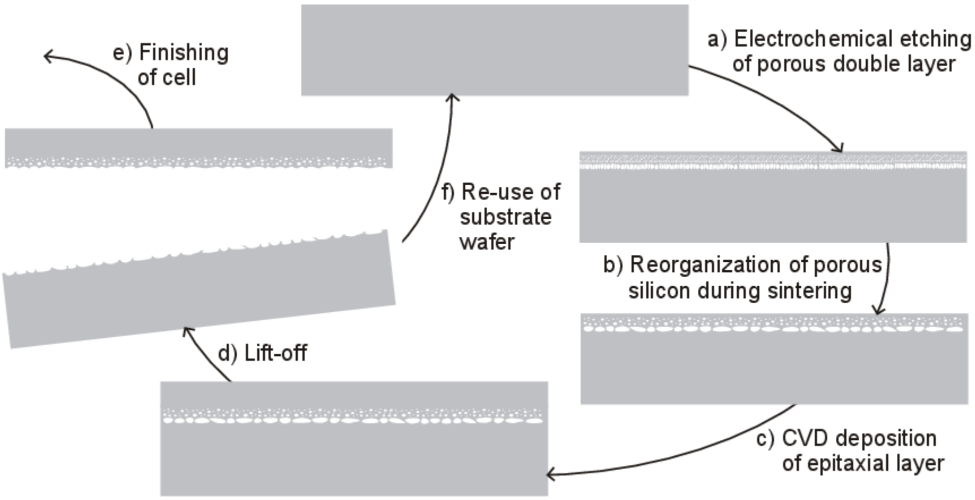

Figure 1: Schematic representation of the PSI Process as developed at ISFH [14]. (a) Electrochemical etching of a porous double layer into a Si substrate wafer. (b) The porous double layer reorganizes during a sintering step in hydrogen atmosphere at 1100 °C. (c) Epitaxial growth of a Si layer by chemical vapor deposition at 1100 °C. (d) Lift-off of the epitaxial layer enabled by the porous layer serving as breaking point. (e) Further processes to finish the epitaxial Si solar cell are required. (f) The substrate wafer can be re-used for the next PSI process cycle.

In the first process step of the PSI process, a porous double layer is etched into the Si substrate wafer using a high concentrated hydrofluoric acid (HF) containing electrolyte. The double layer consists of a starting layer with a porosity of about 22% and a thickness of 1.1 µm; underneath there is a separation layer of much higher porosity of about 40% with a thickness of 0.2 µm. The porous double layer serves as the substrate for a subsequent epitaxial step and later on as the predetermined breaking point for the lift-off of the solar cell from the growth Si substrate wafer. The epitaxial step grows a boron-doped monocrystalline Si layer on top of the porous Si layer. The porous layer closes due to the annealing step prior to epitaxy and the pores reorganize. The monocrystalline Si represents the basis for the solar cell, for which existing cell processes are applicable. The epitaxial layer could either be mechanically supported by means of a glass substrate or a metal, however, even processing as a free-standing layer after lift-off has been demonstrated [4,14]. The schematic structure of a PSI solar cell is demonstrated in Figure 2.

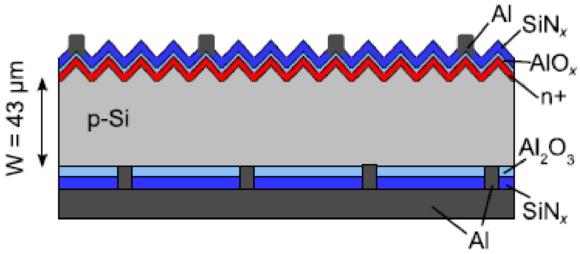

Figure 2: Schematic representation of a PSI solar cell with a thickness of 43 µm [4].

The removal of the remaining porous Si from the substrate wafer enables the re-use after lift-off. Steckenreiter et al. demonstrated a 13-fold re-use of the Si substrate [15], however, a 20-fold re-use is achievable if technical limitations are solved. The most important issue concerning the re-use is the mechanical stability of the substrate, which can be damaged through scratches or occupied by residual porous Si after inhomogeneous lift-off.

1.2 ACCEPTING THE CHALLENGE: CHEMICAL ANALYSIS

The potential of the PSI process for high cell efficiencies on thin Si solar cells has been demonstrated recently [4,6]. However, for an industrial application the economics of the process have to be considered. Therefore, it is indispensable that the re-use of the substrate can be performed as often as possible because this is the crucial part and most beneficial for cost reduction. Since the formation of a homogeneous porous double layer is a prerequisite for a defect-free detachment, it is necessary to investigate the behavior of the etching bath during the lifetime of the bath. The knowledge and understanding of the development of the constituent's concentration in the electrolyte is essential for replenishment in order to increase the bath lifetime. In addition, it will allow calculations concerning the economics of the PSI process for which the HF consumption is a crucial point due to the observation of high HF consumption during etching in laboratory scale so far.

For the investigation of the development of the etching bath constituents suitable chemical analyses methods are required. The main constituent of the PSI etching bath is HF in a high concentration of 19.5 mol/l. Ethanol as the wetting agent and the reaction product H_2SiF_6 complete the constituents. Chemical analyses of PV baths so far have been performed by the group of Acker [16–19]. They have analyzed chemical etching baths as used for the acidic texturization containing HF, HNO_3 and H_2SiF_6 using various method, e.g. titration, fluoride ion-selective electrode (F-ISE), and ion-chromatography (IC). The chemical etching baths investigated in this group have in common with the PSI etching bath the high HF concentration but they differ in the H_2SiF_6 concentration, which is considerably lower for the PSI process. Due to the amount of H_2SiF_6 in the samples, Acker and co-workers were able to demonstrate the practicability of two methods: acid-base titration and an indirect determination by IC including the precipitation as K_2SiF_6. Additionally, the determination of the HF concentration by precipitation reaction with lanthanum nitrate has been invented by the group of Acker. Another group (Zimmer et al.) has reported the investigation of the Si concentrations in chemical PV baths with regard to the application of IC [20–22]. However, the determined Si concentration has again been far away from the traces expected for H_2SiF_6 in the electrochemical electrolyte for the PSI and MacPSI processes.

This work focuses on the analysis of the constituents of the electrolytes used for the electrochemical formation of porous Si at the ISFH. Prior to this work, an enormous HF loss was observable in the PSI etching setup that contradicted an industrial application. Thus, the motivation for this thesis was to investigate and evaluate chemical analysis methods for the electrolyte. The aim was to localize the source of HF loss as well as to gain a considerable understanding of the etching setup in general. In addition, the possibility for reproducible etching results was required even after many hundreds of wafers as well as considerations concerning the economics of the PSI process in case of an industrial application. The chemical analysis opens the possibility of enlarging the lifetime of the electrolyte through minimization of the HF loss and through replenishment. Furthermore, a deeper understanding of the etching process with regard to the changes in the composition concerning the ethanol and the H_2SiF_6 was desired. So, it is important for the PSI process to detach the hydrogen bubbles from the Si surface that form during etching. The rising concentration of H_2SiF_6 could potentially impact the electrochemical equilibria in the etching setup.

The following chapter introduces the electrochemical etching process in general with the focus on the chemical reactions. Subsequently, the investigated chemical methods are described in detail followed by their application on the PSI and MacPSI etching bath (chapter 3 and 4). The adaptability of given methods is investigated and expanded to further suitable analysis methods. With it, the development of the chemical concentrations of HF, ethanol and the reaction product H_2SiF_6 are followed over time and give information concerning the behavior of the bath during bath lifetime. In chapter 5, the properties of the PSI electrolyte are studied in terms of the surface tension, the viscosity, and the ability to permeate through porous Si for decreasing ethanol concentrations. The knowledge of the development of these properties allows investigating a suitable concentration range for the ethanol concentration. In addition, the influence of the reaction product H_2SiF_6 on the etching process is discussed in chapter 6.

2 ETCHING PROCESSES FOR POROUS SILICON

This chapter starts with the introduction of methods for the modification of a Si surface as commonly applied in photovoltaics. The electrochemical etching processes investigated in this work are discussed in detail focusing on the electrochemical reactions and the dissolution mechanisms of Si. Furthermore, the chemistry of aqueous solutions of HF and of HF-ethanol mixtures is addressed.

2.1 MODIFICATION OF SILICON SURFACES

The modification of the Si surface by means of polishing or roughening is essential for the fabrication of solar cells in PV; these are most commonly etching procedures. Etching processes for the formation of porous Si are chemical or stain etching, and electrochemical etching. Before investigating the electrochemical etching in detail, the chemical methods used in PV for the alteration of the Si surface are briefly discussed in the following.

The random pyramid texturization is already a standard process in PV that covers the Si surface with upright or inverted pyramids; an example is demonstrated in Figure 3.

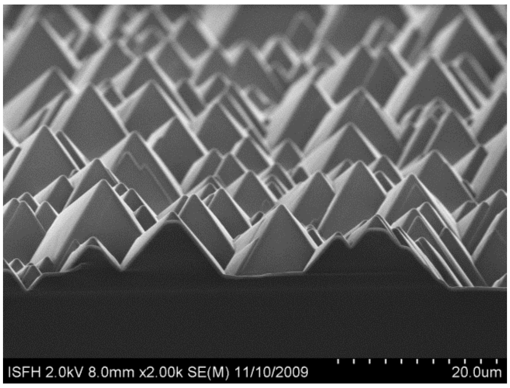

Figure 3: Random pyramid texture of a Si surface for enhanced light-trapping that increases the efficiency of the solar cell.

The purpose of the texturization is to improve the performance of the cell by decreasing the front surface reflectance. Furthermore, an enhanced path length of the light through the cell improves the absorption which is referred to as “light trapping” [23,24]. The formation of the pyramidal structure is an anisotropic process, i.e., the etch rates differ depending on the orientation of the Si planes – (100) or (111). An isotropic etching process dissolves the Si independent on the crystal orientation and accordingly polishes the surface. The distribution of the pyramids is either random or locally and defined through the use of photolithographic masks.

For the texturization of crystalline Si hot aqueous solutions based on sodium hydroxide (NaOH) or potassium hydroxide (KOH) are used commercially. Furthermore, K_2CO_3 solutions are used for the formation of randomly distributed pyramids with an average height of 1 - 2 µm [25]. However, the texturization of multi-crystalline Si surfaces requires acidic solutions since anisotropic etching is not possible due to the lack of a dominant crystal orientation. Here, hydrofluoric acid (HF) solutions with nitric acid (HNO_3) are used in mixtures varying from 1:90 to 1:10 for HF(50%):HNO_3(70%) [26]. Acidic etching is performed at room temperature. Further modification of the performance is possible by adding phosphoric acid (H_3PO_4) or sulfuric acid (H_2SO_4) [27].

One kind of modification of the pyramidal texturing is reported by Hezel and co-workers [28–31]. They have invented the truncated pyramids-concept facilitating the formation of small point contacts on the front side of the solar cell; a schematic representation of such a solar cell is demonstrated in Figure 4. The truncated pyramids are performed by a chemo-mechanical polishing step using a slurry of SiO_2-particles that follows the conventional anisotropic texturization in KOH solutions [32].

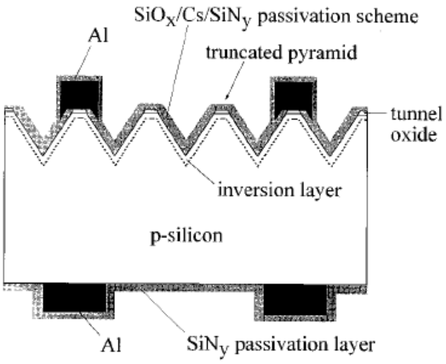

Figure 4: Schematic representation of the solar cell concept using truncated pyramids from Hezel et al. [29]. The tops of the anisotropic etched pyramids are removed by a mechanical polishing step.

Etching processes for the porosification of Si are performed in acidic solutions with HF and require holes at the Si/HF interface for the dissolution of the Si. In chemical or stain etching processes, the holes are provided by chemical oxidant species in the etch solution. A proper chemical oxidant is HNO_3 with NO^+ as the reactive species as identified in the group of Acker [33,34]. Instead of HNO_3 also transition metal ions, i.e., Fe^{3+}, V^{5+}, or Ce^{4+}, are appropriate chemical oxidants with the benefit of reduced bubble formation during the etching process [35–37].

The electrochemical etching process for the formation of porous Si requires holes for the Si dissolution as well. An electric field, i.e., a current that is applied to the Si wafer, forces the holes to move to the Si/HF interface where they react with the fluoride ions. The holes are either present in the bulk Si in case of *p*-type doping or they are generated through illumination in *n*-type doped wafers. The following chapter introduces the electrochemical etching processes used in this work in detail.

2.2 ELECTROCHEMICAL ETCHING OF POROUS SILICON

The chemical reactions for the formation of porous Si via etching are complex and subject of ongoing discussion in literature [38–40]. A mechanism concerning the reactions in the electrochemical setups at ISFH for the formation of porous Si is presented here.

2.2.1 PORE FORMATION

The formation of porous Si by electrochemical etching was discovered by Uhlir and Turner in the 1950s. Independently they found that a thick porous surface layer forms if Si is electrochemically dissolved below a critical current density [41,42]. Since then, the characteristics of porous Si as well as the required etching parameters have been investigated by many research groups. Today, porous Si finds widespread application, e.g., as a sensor material [43] or in medicine application [44]. Besides, it is under investigation as an explosive for airbag igniters [45] or as an ingredient of chewing gum [46]. Additionally, porous Si is a promising material in photovoltaics as well.

In this work, two electrochemical etching processes for the formation of meso- and macroporous Si are investigated, the PSI and the MacPSI process. According to IUPAC, structures with pores of less than 2 nm in diameter are referred to as micropores, between 2 nm and 50 nm as mesopores, and pores with more than 50 nm in diameter are called macropores [47].

The PSI process as performed at ISFH was introduced in chapter 1.1 on page 2. It requires a mesoporous double layer that consists of a starting layer with a thickness of 1.1 µm and a porosity of about 22% and a separation layer with a thickness of 0.2 µm and a porosity of about 40%. The starting layer is used as a substrate layer for a subsequent epitaxial growth of crystalline Si on top. The separation layer is required for the lift-off of the stack of porous Si and epitaxial Si and serves as a predetermined breaking point. The appearance of a mesoporous double layer before and after sintering in hydrogen atmosphere is illustrated in Figure 5.

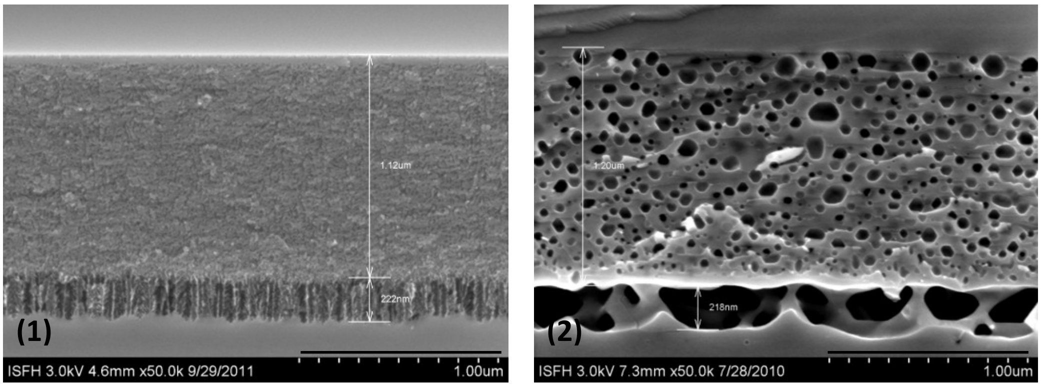

Figure 5: SEM images of a mesoporous Si double layer that is used for the PSI process; (1) before and (2) after sintering in hydrogen atmosphere.

The images were taken at ISFH by scanning electron microscopy (SEM) with a Hitachi S-4800. The unsintered porous Si shows pore diameters of about 2 nm and, therefore, it is referred to as mesoporous. For mesoporous Si that was etched with similar parameters a surface area of about 230 m^2/cm^3 was reported by Herino et al. [48]. They investigated nitrogen adsorption isotherms using the Brunauer-Emmett-Teller (BET) model.

The SEM image in Figure 6 shows the appearance of a MacPSI layer that was processed at ISFH. The pores are macropores according to IUPAC due to the average pore diameters of (4.7 ± 0.2) µm [9,47]. The porous layer has a thickness of 30 µm and can be used as an absorber layer in solar cells after further process.

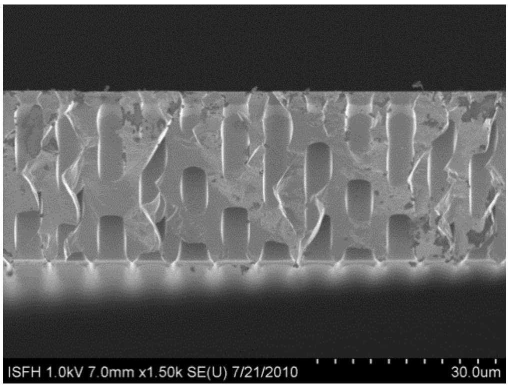

Figure 6: SEM image of a macroporous Si layer etched at ISFH that is used as an absorber layer in the MacPSI process.

Under the applied conditions investigated in this work, anodic dissolution of a *p*-type Si wafer in the dark leads to the formation of mesopores, whereas the macropores grow if the rear-side of an *n*-type Si wafer is illuminated. Both processes require the existence of holes at the Si/HF interface. The holes are either incorporated by doping with boron as in the case of the *p*-type Si wafer or they are generated by illumination on the rear-side of an *n*-type Si wafer. The holes are driven by an external voltage to the Si/HF interface, where they react with the fluoride species present in the electrolyte as illustrated in Figure 7.

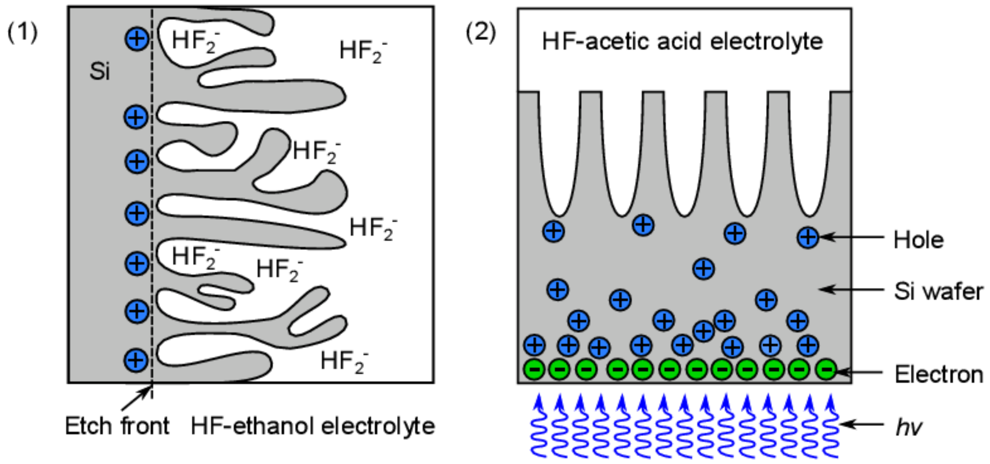

Figure 7: Anodic etching of porous Si in HF electrolytes. (1) Anodic etching of *p*-type Si in the dark and (2) of *n*-type Si under illumination, the latter is adapted from [49]. Essential for both processes is the existence of holes at the Si/HF interface that are consumed during the etching.

Various porosities are accessible through the variation of the current density applied during the etching process. Figure 8 depicts the correlation for the PSI process at ISFH.

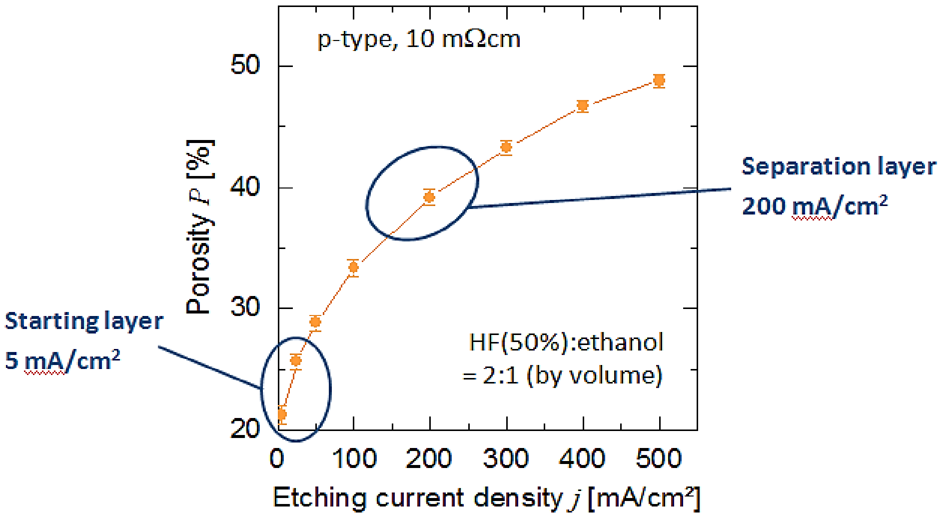

Figure 8: Dependency of the porosity of the PSI layers at ISFH on the etching current density according to [50].

In this work, the porosity *P* [%] is determined according to the description in [51] by gravimetric analysis following

$$P = \frac{m_1 - m_2}{m_1 - m_3} \qquad (2.1).$$

Here, m_1 denotes the weight of the porosified Si substrate before and m_2 after porosification. Finally, m_3 is related to the weight of the remaining substrate and determined by gravimetric analysis of the remaining substrate wafer after the porous Si has been selectively dissolved in aqueous KOH.

Before the chemical dissolution of the Si is investigated in more detail, it is interesting to see how the etching parameters current and voltage influence the porosification process. Therefore, Figure 9 illustrates characteristic *J*-*V* curves for the dissolution of *p*-type Si and *n*-type Si, respectively.

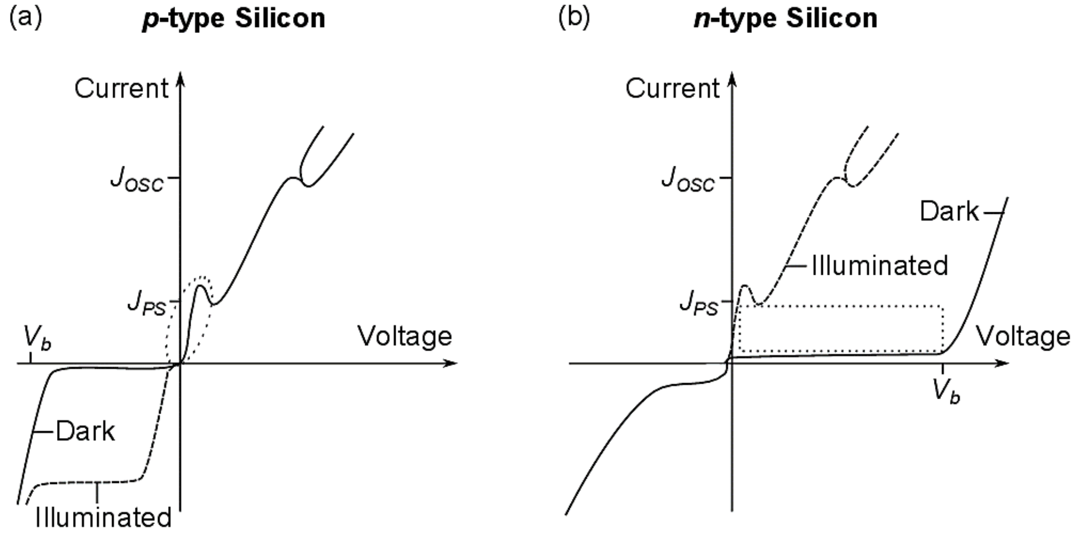

Figure 9: Characteristic *J*-*V* curves for the formation of porous Si on (a) *p*-type Si and (b) *n*-type Si [51]. PSI process: The formation of mesopores in the dark takes place at current densities below J_{PS} as indicated by the dotted ellipse in (a). MacPSI process: The macropores form under illumination at current densities below J_{PS} in the range marked by the dotted box in (b).

The *J*-*V* curves indicate the correlation of the applied current density with the voltage. Most important for the understanding of pore formation is the peak at the current density J_{PS} (PS = porous silicon). Pore formation takes generally place in the current density region below the J_{PS} peak. The dotted ellipse in Figure 9(a) shows the parameter region where mesopores are obtained on *p*-type Si; in more detail, mesoporous Si is obtained only for etching parameters that lay directly on the curve. This region is very narrow compared to the parameter region for the formation of macroporous Si on *n*-type Si, which is indicated by the dotted box in (b). The macropores are formed at a current density below J_{PS} with a sufficiently high voltage above V_{PS}. This leads to the three etching parameters for the MacPSI process: the current density, the voltage, and the intensity of the rear-side illumination. In Figure 9, current densities above J_{PS} exceed the parameters used for electrochemical dissolution investigated in this work; this is where electropolishing takes place until oscillations occur at current densities above J_{OSC}.

The following paragraph deals with the chemical processes during the electrochemical dissolution of Si.

2.2.2 CHEMICAL DISSOLUTION MECHANISMS

There are two dissolutions mechanisms for Si discussed in literature: the divalent dissolution mechanism requires two charge carriers, whereas the tetravalent requires four charge carriers for the dissolution [38,39].

The divalent dissolution

The divalent dissolution

$$\mathrm{Si} + 4\,\mathrm{HF_2^-} + 2\,h^+ \rightarrow \mathrm{SiF_6^{2-}} + 2\,\mathrm{HF} + \mathrm{H_2} \qquad (2.2)$$

is dominant for the formation of micro- and mesoporous Si and is obtained at current densities below J_{PS}. The mechanism is demonstrated in Figure 10.

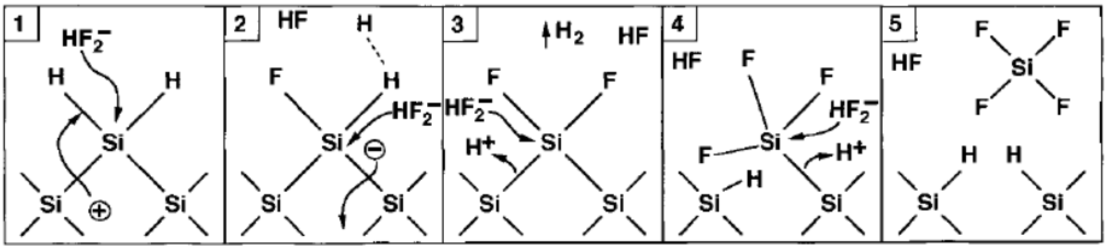

Figure 10: Reaction scheme for the divalent dissolution mechanism of bulk Si through $\mathrm{HF_2^-}$ as suggested by Lehmann [52].

Here, the applied current initiates the drift of holes (h^+) in the valence band. At the Si/HF interface, a hole recombines with one of the binding electrons from the Si–H bond and leaves a positive charge on the oxidized Si atom (Figure 10, picture 1).

$$\mathrm{R_3Si{-}H} + h^+ \rightarrow \mathrm{R_3Si^+} + \tfrac{1}{2}\,\mathrm{H_2}\uparrow \qquad (2.3)$$

The number of available holes at the Si/HF interface is the rate-limiting parameter in the divalent dissolution mechanism. The positive charge on the Si according to equation (2.3) enables the nucleophilic attack by $\mathrm{HF_2^-}$ as the active etching species (picture 1). This initial substitution of Si–H with Si–F is the origin of pore formation. Since the Si–F bond is much stronger (6 eV) than the Si–H bond (3.5 eV), a second $\mathrm{HF_2^-}$ attacks the weakened Si–H bond leading to a second Si–F bond (picture 2) [39]. Simultaneously, molecular hydrogen leaves the reaction site (picture 3). Furthermore, for each $\mathrm{HF_2^-}$ molecule that reacts with the Si a HF molecule is released. The initial bond formation between Si and fluoride facilitates further bonds to fluoride and, thus, the detachment of a Si atom from the surface. This is due to the strong polarizing effect of fluoride that weakens the Si backbonds whenever a bond between a fluorine atom and a Si atom is established [39]. Thus, the weakened bonds are attacked by further HF_2^- as shown in Figure 10 (pictures 2-4).

$$Si^+ + 4\ HF_2^- \rightarrow SiF_4 + 4\ HF + 3\ e^- \qquad (2.4)$$

The liberated SiF_4 (picture 5) further reacts according to [53] in

$$SiF_4 + 2\ HF \rightarrow SiF_6^{2-} + 2\ H^+ \qquad (2.5)$$

with SiF_6^{2-} as the reaction product, which is stable in aqueous solutions and remains in the electrolyte. The Si is not dissolved completely but develops a porous structure due to the limited number of available holes at a time.

The protons from equation (2.5) and two electrons from equation (2.4) lead to the formation of hydrogen gas on the cathode.

$$2\ H^+ + 2\ e^- \rightarrow H_2\uparrow \qquad (2.6)$$

This is the reduction that accompanies the anodic oxidation of the Si and keeps the pH of the electrolyte constant. Therefore, there are two sources of hydrogen release associated with the formation of porous Si: Hydrogen release from the Si surface during porosification and hydrogen release on the cathode due to equation (2.6).

Noteworthy, the redundant electron in equation (2.4) recombines with a second hole from the bulk Si [38].

The tetravalent dissolution

At current densities above J_{PS} the quantity of holes increases. As a result, the fluoride ions become the rate-determining species for the dissolution in contrast to the mechanism discussed before. The dissolution mechanism obtained above J_{PS} requires four holes and, therefore, it is a tetravalent mechanism. It is also referred to as electropolishing leading to a planar Si surface free of porosity. The tetravalent dissolution is a two-step mechanism that begins with the formation of an anodic oxide on the Si surface as it is shown in Figure 11.

$$Si + 2\ H_2O + 4\ h^+ \rightarrow SiO_2 + 4\ H^+ \qquad (2.7)$$

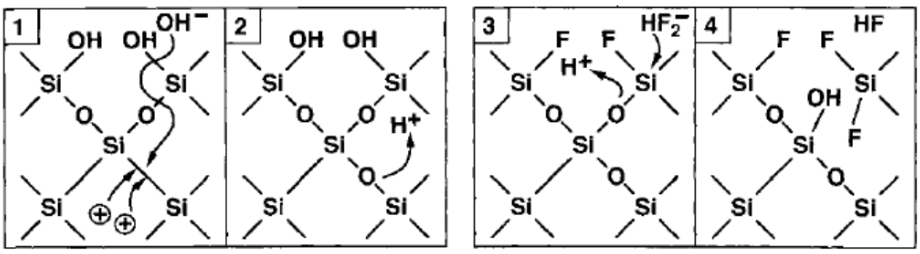

Figure 11: Reaction schemes for the tetravalent dissolution mechanism as suggested by Lehmann [52].

Pictures 1 and 2 in Figure 11 illustrate the oxidized Si surface. Due to the attack of oxygen-species, further backbonds are oxidized. The applied potential enables the drift of those species into the bulk Si leading to the formation of Si–O–Si, thereby consuming two holes [39]. The second step of the tetravalent dissolution mechanism is the dissolution of the formed oxide by a nucleophilic attack of HF_2^- on the Si–O–Si bridges according to pictures 3 and 4 in Figure 11.

$$SiO_2 + 6\ HF \ \rightarrow\ SiF_6^{2-} + 2\ H^+ + 2\ H_2O \qquad (2.8)$$

At the same time, H^+ ions perform an electrophilic attack on the oxygen backbonded to the Si. In summary, four charge carriers are required for the dissolution of one single Si. The reaction product is SiF_4 again, which forms SiF_6^{2-} in the aqueous hydrogen fluoride surrounding. The tetravalent dissolution mechanism involves no release of hydrogen from the Si surface; however, the formation of hydrogen on the cathode is still present.

The valence n defines how many electrons are available for the dissolution of a single Si atom. It quantitatively describes which of the dissolution mechanisms occurs due to the applied etch conditions. If $n = 2$, the divalent dissolution mechanism occurs, whereas for $n = 4$ the tetravalent dissolution takes place. The valences for the porous layers in the PSI process were determined in this work according to Appendix A. The valence of the starting layer calculated to $n = (2.6 \pm 0.4)$ indicating that the formation of mesopores is caused by the divalent dissolution mechanism. The valence for the separation layer was determined to $n = (9 \pm 5)$, which is a hint for the tetravalent dissolution taking place. The large uncertainty could be explained by the strong influence of the porosity and thickness of the layer on the valence. The valence for a combination of the starting and separation layer in the MacPSI process was determined by Ernst and is $n = (2.91 \pm 0.34)$ [54]. This indicates that the formation of macropores involves both mechanisms, divalent and tetravalent dissolution.

As a result of the electrochemical etching processes described above the surface of the Si in an HF electrolyte is covered by silicon dihydride SiH_2 and hydrogen-associated silicon fluorides as $SiH_2(SiF)$ and SiH_2F_2 with their concentrations depending on the HF content of the electrolyte [55,56]. A thorough rinse with distilled water after etching leaves the silicon surface hydrogen-terminated [56,57].

2.2.3 EXPERIMENTAL SETUP AND ELECTROCHEMICAL REACTIONS

This paragraph deals with the experimental parameters used for the porosification at ISFH and discusses the electrochemical reactions. The PSI and the MacPSI process are investigated separately.

The PSI process

We use (100)-oriented, monocrystalline, Czochralski (Cz)-grown, single-side polished *p*-type Si wafers with a boron-doping of about 10^{18} - 10^{19} cm^{-3} and a resistivity between 8 - 20 mΩcm. These substrate wafers have a diameter of 6” and a thickness of (675±15) µm. The electrolyte is prepared by mixing 50 wt% HF (Hydrofluoric Acid 50%, VLSI PURANAL®, Honeywell, Germany) and ethanol (Ethanol absolute, PURANAL®, Honeywell, Germany) in the ratio of 2:1, leading to initial concentrations of 19.5 mol/l for HF and 5.7 mol/l for ethanol; the total volume of the electrolyte used at ISFH is 14.9 liter taking the volume contraction into consideration (see chapter 2.4.2 on page 22). The etching current density varies between 5 and 200 mA/cm^2 for the preparation of the starting and separation layers, respectively. The according voltages are 9 V for the starting layer and about 23 - 24 V for the separation layer. The etching area is 145 cm^2.

The setup of the PSI etching bath is illustrated in Figure 12. The anode consists of a coated Si wafer that is highly *p*-doped, whereas the cathode is made from a highly doped *n*-type Si wafer. The Si substrate wafer is fixed in the mid distance of anode and cathode separating the electrolyte into two parts of about the same volume. The tunnels cause a homogeneous distribution of the current density from the electrodes to the wafer. For the formation of mesoporous Si, the current density is the controlled variable in the etching system. That means, the etching software adjusts the voltage according to the current density under consideration of the resistances in the system, i.e., mainly the resistances of the electrolyte and the Si substrate.

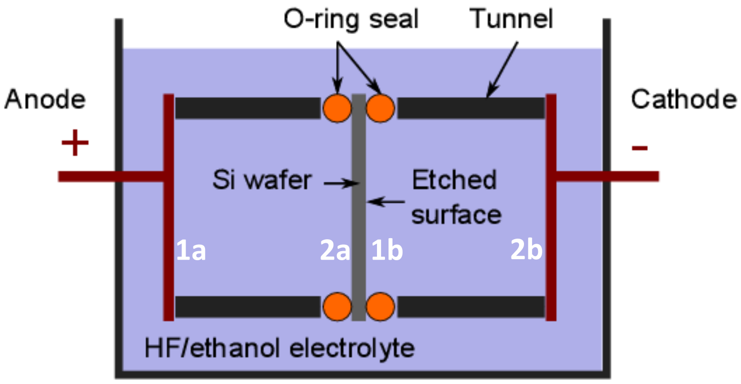

Figure 12: Schematic representation of the setup of the etching tool for the PSI process. Positions 1a and 1b indicate locations for oxidation reactions, positions 2a and 2b locations for reduction reactions.

In the following the chemical reactions that occur during the etching process are discussed. The reactions simplify the reality since the mechanisms and dependencies are still subject of discussion in literature [38–40].

The dissolution of the Si is an anodic oxidation on the Si surface facing the cathode on position (1b) in Figure 12. The standard electrode potentials E^0 given here are related to the standard hydrogen electrode (SHE) as a reference and reported in literature [58,59]. The general dissolution of Si is described by

$$Si + 6\,F^- \rightarrow SiF_6^{2-} + 4\,e^- \qquad E^0 = -1.37\ V \qquad (2.9).$$

The electrons are injected into the bulk Si and recombine with the holes [38]. The balancing reduction reaction is the hydrogen formation on the cathode on positions (2a) and (2b) in Figure 12.

$$2\,H^+ + 2\,e^- \rightarrow H_2 \qquad E^0 = 0\ V \qquad (2.10)$$

In the following, we will estimate the likelihood of side reactions with the wetting agent ethanol and the dissolution product SiF_6^{2-} in the PSI etching bath to take place without the claim of completeness. Our considerations require the knowledge of the electrode potentials as well as the determination of the voltage that remains for the side reactions. In general, the following reactions concerning the fluoride species may occur during the etch process in addition to equations (2.9) and (2.10). The standard potentials are listed in [59].

$$2\,F^- \rightarrow F_2 + 2\,e^- \qquad E^0 = 2.87\ V \qquad (2.11)$$

$$2\,HF \rightarrow F_2 + 2\,H^+ + 2\,e^- \qquad E^0 = 3.05\ V \qquad (2.12)$$

$$HF_2^- \rightarrow F_2 + H^+ + 2\,e^- \qquad E^0 = 2.98\ V \qquad (2.13)$$

Furthermore, the oxidation of the ethanol (CH_3CH_2OH) may occur in the PSI etching tool leading to the formation of acetaldehyde (CH_3CHO), acetic acid (CH_3COOH), and subsequently carbon dioxide (CO_2).

$$CH_3CH_2OH \rightarrow CH_3CHO + 2\,H^+ + 2\,e^- \qquad E^0 = -0.25\ V \qquad (2.14)$$

$$CH_3CHO + H_2O \rightarrow CH_3COOH + 2\,H^+ + 2\,e^- \qquad E^0 = 0.18\ V \qquad (2.15)$$

$$CH_3COOH + 2\,H_2O \rightarrow 2\,CO_2 + 8\,H^+ + 8\,e^- \qquad E^0 = -0.13\ V \qquad (2.16)$$

The electrode potentials for these reactions were calculated according to

$$E^0 = -\frac{\Delta_R G^0}{z\,F} \qquad (2.17)$$

with $\Delta_R G^0$ as the Gibbs energy [kJ/mol] taken from [58] and listed in Table 2.1, z as the number of transferred electrons, and F as Faraday's constant.

Table 2.1: Gibbs energy for the oxidation of ethanol [58]. The states are indicated with (aq) = aqueous and (l) = liquid.

Chemical formula	State	Gibbs energy, ΔG [kJ/mol]
CH_3CH_2OH	(aq)	-177.00
CH_3CHO	(l)	-128.12
CH_3COOH	(aq)	-399.60
CO_2	(aq)	-385.98
H_2O	(l)	-237.13

With these electrode potentials we check whether the reactions could take place in the environment of the PSI etching bath. Therefore, we investigate the resistitivites that exist in the etching setup in more detail and determine the voltages that are applicable for the reactions cited above.

The Si wafer in the PSI process has a thickness d of about 675 µm and a bulk resistivity ρ of 8 - 20 mΩcm. The resistance R_{Wafer} [Ω] of the wafer is

$$R_{Wafer} = \frac{\rho}{d} \tag{2.18}$$

and, hence, in the range of 0.12 - 0.30 Ω. The current I [A] is calculated by multiplying the applied current density J [5 mA/cm^2 and 200 mA/cm^2] with the etching area A [145 cm^2].

$$I = J \cdot A \tag{2.19}$$

The current required for the formation of the starting layer in the PSI process calculates to I = 0.725 A and for the separation layer to I = 29 A. With this, the potential difference V_{Wafer} [V] across the wafer is calculated with Ohm's law.

$$V_{Wafer} = R_{Wafer} \cdot I \tag{2.20}$$

As a result, the potential difference for the starting layer V_{Wafer} is 87 - 218 mV and for the separation layer it is 3.5 - 8.7 V. The calculations demonstrate the dependency of the potential difference on the resistance of the wafer R_{Wafer}, i.e, 8 - 20 mΩcm.

We will discuss the consequences for the side reactions addressed above in the following considerations. The applied voltages for electrochemical etching V_{PSI} are 9 V for the starting layer and up to 24 V for the separation layer in the PSI process. Therefore, the potential difference that is left over for the HF electrolyte V_{HF} calculates to

$$V_{HF} = \frac{V_{PSI} - V_{Wafer}}{2} \tag{2.21}$$

taking into account the separation of the etching bath into two parts by the wafer according to Figure 12. Therefore, 4.4 - 4.5 V remain for possible side reactions according to equations (2.14) to (2.16) for the starting layer and 7.7 - 10.3 V remain for the separation layer. These voltages include the potential difference for the HF solution – which we expect to be negligible due to the high ionic strength in the electrolyte – furthermore all potential differences related to the resistivities on the interfaces solid/electrolyte as well as the overvoltage due to the gas formation. Nevertheless, the oxidation of ethanol is very likely to occur under the applied voltage; position (1a) in Figure 12 indicates where the oxidation takes place. It has to be noted that the results base upon thermodynamic data and do not take into consideration the kinetics of the reactions. Thus, reliable statements related to the yield or the reaction rates are not possible. If the oxidation would complete to CO_2, it is not likely to stay in the electrolyte. This is due to the solubility in water, which is moderate with 1.5 g CO_2 dissolving in 1 l of water [60]. The formation of carbonate species as HCO_3^- and CO_3^{2-} is not expected due to the low pH in the etching electrolyte, i.e., pH 1.

It should be taken into consideration that the PSI setup does not include a reference electrode. Therefore, it is difficult to compare the parameters to standard electrode potentials. Further investigations would require the determination of the overvoltages for the formation of hydrogen and CO_2 on the electrodes used in the PSI process. This would enable reliable statements concerning the electrochemical reactions in the electrolyte and in particular the likeliness of the existence of the oxidation products.

The MacPSI process

The substrate in the MacPSI process as performed at ISFH is a (100)-oriented, monocrystalline, Cz-grown, shiny-etched, *n*-type Si wafer of 6” in diameter. The phosphorous doping is $2.8 - 3.8 \cdot 10^{15}$ cm^{-3} due to a resistivity of (1.5 ± 0.2) Ωcm and the thickness of the wafer is (305 ± 20) µm. The electrolyte consists of a 1.43 mol/l aqueous HF solution with 1.14 mol/l acetic acid as the surface wetting agent; the total etching bath volume is 4.585 l. The temperature is fixed at 20 °C.

The etching setup (from ET&TE, Etch and Technology GmbH, Germany) with rear-side illumination through a LED-array for macroporous Si is illustrated in Figure 13.

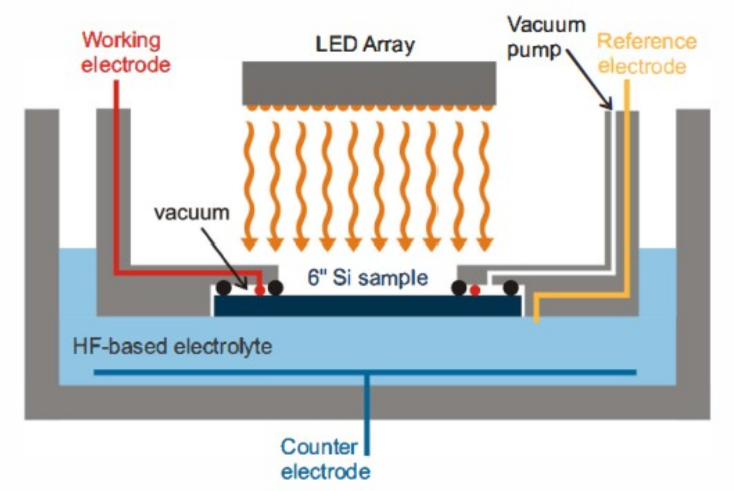

Figure 13: Schematic representation of the setup of the etching tool for the MacPSI process [8], © [2012] IEEE.

In Figure 13, the working electrode (red) is a platinum wire that contacts the Si wafer on the rear side. The reference electrode (yellow) is also made from platinum and is located close to the Si substrate in order to take into account the potential drop in the electrolyte. Besides, a platinum coated plate represents the counter electrode (blue). The etching area is 133 cm^2. For this tool, periodic tilting of a rocking table is implemented at ISFH leading to a continuous movement of the electrolyte as well as to a facilitated release of the hydrogen bubbles from the Si surface.

The resulting macroporous layers typically have a thickness of about 30 µm and a porosity of (23 ± 2)%. They are formed at an etching current density of 6 mA/cm^2 at 2 V for 40 min; the separation layers are formed with an enhanced current density of up to 24.8 mA/cm^2 at 4 V within 6 min until a porosity of almost 100% is reached [61].

Here, we discuss the likelihood of the oxidation of acetic acid in the etching setup as used at ISFH during the formation of the macroporous layer. The approach differs to the appraisal for the PSI process as discussed above. The main difference is that the Si wafer in the PSI setup is contacted through the electrolyte on both sides, whereas the wafer in the MacPSI setup is directly contacted with only one side of the wafer exposed to the electrolyte. In the MacPSI setup of the ISFH, the potential measured between the reference electrode and the working electrode is 2 V. Taking into consideration the standard electrode potential for the reaction between Si and fluoride of -1.37 V as denoted in equation (2.9), we assume that the oxidation of acetic acid is reasonable due to the electrode potential of -0.13 V even in the presence of some overvoltage.

2.3 PORE HOMOGENEITY AS THE DESIRED PROPERTY IN THE PSI PROCESS

The mesoporous layers sinter during the high temperature step that is part of the epitaxial growth at about 1100 °C in hydrogen atmosphere. The surface on top closes and forms an ideal seed layer for the epitaxial growth of monocrystalline Si. Furthermore, the porous layers reorganize through material transport from the separation layer with high porosity to the starting layer with a lower porosity [51,62]. Accordingly, the voids in the separation layer grow and only small bridges remain, which serve as predetermined breaking points. The more homogeneous the etching succeeds the more homogeneous bridges in terms of their width form during the high temperature step. A narrow distribution of the widths of the bridges in the separation layer is desirable since the bridges are the crucial point for the lift-off of the PSI cell from the substrate wafer. For example, if some bridges are thicker and accordingly more stable than others, residual porous Si remains on the substrate wafer. Moreover, cracks could originate in the detached layer leading to a decreased yield. A homogeneous distribution of similar formed bridges is therefore essential for an industrial application of the PSI process. In this work, the term “homogeneity” will be related from now on to the distribution of the thicknesses of the bridges in the separation layer.

We found that the thickness of the bridges in the separation layer affects the detachability of the mesoporous layers. Figure 14 shows the appearance of PSI layers etched at ISFH after reorganization in a hydrogen atmosphere, the left one etched in a fresh electrolyte with the initial ethanol concentration of 5.7 mol/l, the right one etched in a used electrolyte containing less than 4.0 mol/l.

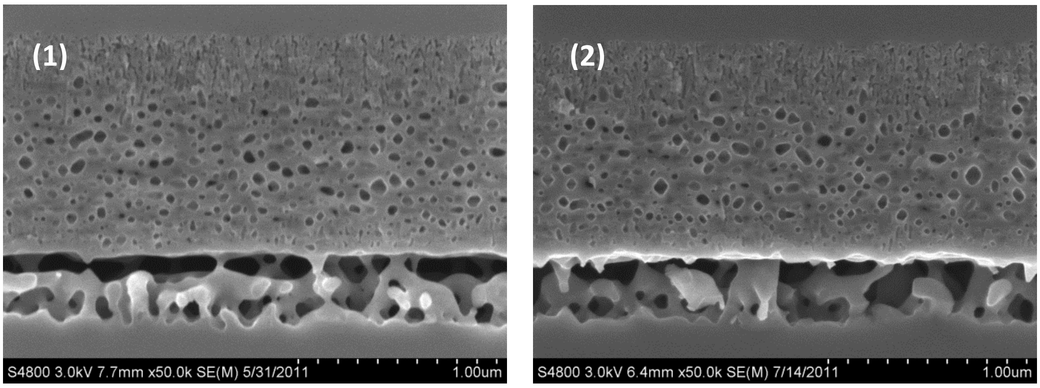

Figure 14: SEM images of mesoporous Si layers etched at ISFH after reorganization. (1) Detachable PSI layer, (2) Non-detachable PSI layer. Note that the remaining Si bridges in (2) are thicker than in (1).

Figure 14 depicts that the bridges in the non-detachable porous layer on the right image are thicker than in the detachable layer on the left. Chapter 5 discusses if the thickness of the bridges might be related to the ethanol concentration in the electrolyte.

Benefits of chemical analysis

Homogeneously distributed bridges of a similar width require a homogeneously etched separation layer. The etching result depends on various parameters: The applied current density, the doping level of the substrate, and the HF concentration of the electrolyte [48,63]. Only a constant combination of these three parameters allows expecting similar etching results in terms of porosity. For an industrial application a constant quality of the porous layers is necessary, i.e., the etching layers of the first wafer of a batch should be fabricated under the same conditions as the 10 000th wafer. The prerequisite is to keep the three etching parameters constant. The doping of the substrate wafer is given by its resistivity and varies in a certain range, i.e., 8 - 20 mΩcm, as set by the manufacturer. Thus, the doping of the substrate wafer is predetermined. The parameters of the applied current density and voltage depend on this doping of the substrate; the process window for a specific porosity is pictured in Figure 8 on page 9. Therefore, the determination of suitable current density parameters requires experience of the operator as well as considerable experimental amount of work. This is the reason why the parameters should be kept constant if possible. In addition, the HF concentration of the electrolyte affects the homogeneity of the pore formation. Due to the chemical dissolution of Si, the HF concentration decreases with the number of etched wafers. In more detail, the concentration of the free fluoride decreases, whereas the reaction product silicon hexafluoride (SiF_6^{2-}) consumes six fluorides and accumulates in the electrolyte. A replenishment of the electrolyte with HF counteracts the decrease of the free fluoride concentration. For the calculation of the appropriate amount of HF it is necessary to know the correct concentration of free fluoride ions in the etching bath.

$$[F^-]_{free} = [F^-]_{total} - [F^-]_{bonded} \qquad (2.22)$$

The access to the total fluoride concentration $[F^-]_{total}$ and to the dissolved Si $[SiF_6^{2-}]$ is possible through chemical analysis methods. Those methods were investigated in the context of this work evaluating their practicability concerning the electrochemical etching bath and the benefit for a prospective industrial application of the PSI process. Figure 15 illustrates the theoretical proportions of the chemical concentrations in the PSI etching bath after the porosification of 200 wafers. The analysis of the traces of the reaction product SiF_6^{2-} beneath the overwhelming amount of fluoride is one of the challenges in this work.

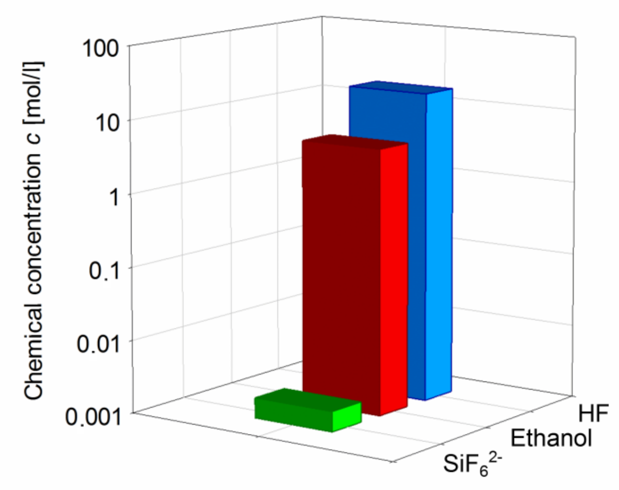

Figure 15: Theoretical proportions of the chemical concentrations in the PSI etching bath after porosification of 200 wafers in a logarithmic scale.

2.4 CHEMISTRY OF THE ELECTROLYTE

The etching electrolyte of the PSI process consists of hydrofluoric acid (HF, 50 wt%) and ethanol, mixed in a volume ratio of 2:1. This paragraph introduces the chemistry of aqueous HF solutions as well as of mixtures of HF and ethanol.

2.4.1 HYDROFLUORIC ACID

HF is a week acid with a pK_S of 3.17 at 25 °C [64]. Common fluoride species in aqueous HF solutions are HF, HF_2^-, H_2F_2, and F^-. Their concentration depends on the pH of the solution according to Figure 16. In the PSI electrolyte at pH 1, the dominant components are HF and H_2F_2 [39,65]. It should be mentioned that the existence of H_2F_2 is still subject of discussion in literature [66].

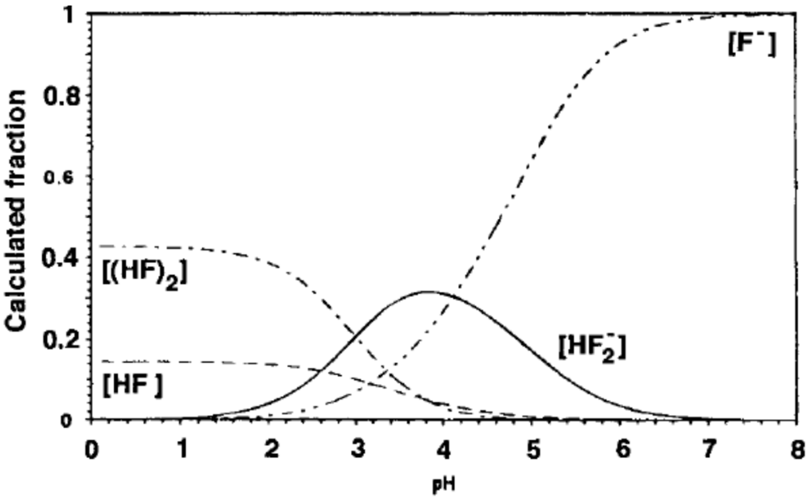

Figure 16: Calculated fraction of each component in an aqueous HF solution as a function of the pH for a fixed total fluoride concentration of 7.5 mol/l adapted from [39,65].

The total concentration of HF in the electrolyte includes HF, HF_2^-, H_2F_2, and F^- with the following reactions and equilibrium constants *K* (at 25 °C) [67,68]:

$$\mathrm{HF} \rightleftharpoons \mathrm{H^+} + \mathrm{F^-} \qquad \text{with } K_1 = \frac{[\mathrm{H^+}][\mathrm{F^-}]}{[\mathrm{HF}]} = 6.71\cdot 10^{-4}\,\frac{\mathrm{mol}}{\mathrm{l}} \tag{2.23}$$

$$\mathrm{HF} + \mathrm{F^-} \rightleftharpoons \mathrm{HF_2^-} \qquad \text{with } K_2 = \frac{[\mathrm{HF_2^-}]}{[\mathrm{HF}][\mathrm{F^-}]} = 3.86\,\frac{\mathrm{l}}{\mathrm{mol}} \tag{2.24}$$

$$2\,\mathrm{HF} \rightleftharpoons \mathrm{H_2F_2} \qquad \text{with } K_3 = \frac{[\mathrm{H_2F_2}]}{[\mathrm{HF}]^2} = 2.7\,\frac{\mathrm{l}}{\mathrm{mol}} \tag{2.25}$$

The equilibrium constants give evidence for HF as a weak acid. HF differs in its dissociation behavior from the other hydrohalic acids HCl, HBr, and HI. This was attributed in literature to the greater strength of the H–F bond, to the existence of the dimer H_2F_2, or to ring structures as discussed in [39].

Solutions of HF are extremely harmful to human skin and tissue. Therefore, suitable protective equipment as well as the strict obedience of the safety instructions is of great importance.

2.4.2 ETCHING ELECTROLYTE: HF AND ETHANOL

Ethanol is added to the etching electrolyte as a wetting agent. Wetting agents reduce the surface tension and, thus, support the release of hydrogen gas that forms on the Si surface during the etching process [69]. If the bubbles stick to the surface, they hinder the access of the fluoride ions and, therefore, lead to inhomogeneous etched porous layers [70,71].

Ethanol and HF are miscible in all proportions. However, the volume contraction needs to be taken into consideration for the determination of the total volume. The volume contraction in this work $V_{vol.cont.}$ was calculated according to

$$V_{\mathrm{vol.cont.}} = \left(V_{\mathrm{HF}} + V_{\mathrm{Ethanol}}\right) - \left(\frac{\rho_{\mathrm{HF}}\cdot V_{\mathrm{HF}} + \rho_{\mathrm{Ethanol}}\cdot V_{\mathrm{Ethanol}}}{\rho_{\mathrm{Electrolyte}}}\right) \tag{2.26}$$

Here, V denotes the volumes of the pure HF and ethanol solutions, respectively, and ρ the densities. In equation (2.26) we considered the density of the electrolyte as 1050 g/l according to information given by a former manufacturer of the electrolyte. As a result, $V_{vol.cont.}$ is calculated to be below 100 ml for the PSI etching bath prepared from 5 liter ethanol and 10 l HF (50 wt%).

The addition of ethanol impacts the chemical equilibria of the HF species as given in equation (2.23) to (2.25). Since the ethanol content in the PSI etching bath is 25 wt%, literature values for aqueous HF solutions containing 30 wt% of ethanol are comparable as reported by Luxenberg and Kim [72]. They report for $K_1 = 0.84 \cdot 10^{-4}$ mol/l and for $K_2 = 8.84$ l/mol. The lower equilibrium constant K_1 in case of ethanol addition indicates that the dissociation of HF is reduced if ethanol is present. As a result, the fluoride concentration is lower in comparison to aqueous HF solutions. The reduced dissociation is due to the stronger electrostatic dipole-dipole interactions in low dielectric media [73]. Furthermore, the addition of ethanol to aqueous HF solutions leads to a shift of the chemical equilibrium to an increased HF_2^- concentration as indicated by K_2. Since HF_2^- is suggested as the major active etching species in ethanol containing aqueous HF solutions [73], the addition of ethanol has reasonably a positive impact on the etching process.

3 CHEMICAL ANALYSIS OF THE ETCHING SOLUTIONS

The previous chapter states the advantages and benefits of chemical analysis for the formation of mesoporous Si within the PSI etching process. In the context of this work, a variety of methods was considered for the determination of the constituents of the etching baths with the attention focusing on the industrial applicability of the methods. Titration, i.e., precipitation titration with lanthanum nitrate $La(NO_3)_3$ and the fluoride ion-selective electrode (F-ISE) were investigated for the determination of the fluoride concentration in the PSI and MacPSI etching baths. Ion-chromatography (IC) was chosen for the analysis of the Si concentration and the cuvette test method for the determination of the total organic carbon content (TOC). Titration was adapted at ISFH since 2009; F-ISE, IC, and the cuvette test method were established and verified within the scope of this work.

There are a couple of other methods conceivable for the determination of the etching bath constituents. For example, the most common analysis methods for Si traces are AAS (atomic absorption spectroscopy), ICP-OES (inductively coupled plasma optical emission spectrometry), and ICP-MS (ICP combined with mass spectrometry) [74]. However, the acquisition of these methods was out of scope of the project. Furthermore, the compatibility of the methods with the high concentration of fluoride in the PSI etching bath is at least questionable and could require a specialized setup. In this work, the decision to use the IC for the investigation of the Si content in the etching baths was due the fact that the IC is a multifunctional tool with the possibility of prospective applications for further wet chemical baths at ISFH. Besides the investigated cuvette test method for the total organic carbon content, the ethanol and acetic acid concentrations are available by an automated TOC device. However, the high fluoride content in the samples has prevented its use since it contains gold-covered metal plates which corrode in the presence of fluoride according to the manufacturer. This could be overcome by the implementation of a gas washing bottle, however, the disadvantage of a lower general sensitivity of the device led to the exclusion of this method. The fluoride concentration could be determined indirectly by NIR (near infrared spectroscopy) or directly by IC [21,22]. It is reasonable to suggest the extension of the IC analysis from the determination of the Si to the fluoride concentration in this work. However, the fluoride samples in this work have been analyzed before the IC was implemented at ISFH. Since the scope of the PSI project only allowed low effort methods for economic reasons, the titration and F-ISE were the methods of choice for the fluoride analysis.

This chapter discusses the theory and experimental details of the methods investigated in this work. Each paragraph examines the applicability and notes if special adjustments were necessary to adapt the method to be suitable for the PSI and MacPSI etching baths. The results obtained are verified by the determination of the recovery rate for all analysis methods in order to evaluate the accuracy of the method. Furthermore, the results are compared to external reference measurements in case of the fluoride determining methods. The uncertainty of each method is addressed; a detailed determination of the measurement uncertainties is attached to Appendix B, where exemplarily calibration curves for each method can be found.

3.1 DETERMINATION OF FLUORIDE

HF is essential for the dissolution mechanisms of Si and, therefore, an important parameter for homogeneous etching results in terms of the separation layer formation as discussed in chapter 2.3 on page 19. However, a great amount of fluoride – as is the case for the PSI etching baths – limits the number of suitable analysis methods since glassware or metals are not resistant against HF. The following chapter describes the analysis methods that were found to be suitable for the etching baths discussed in this work, i.e., titration with lanthanum nitrate and F-ISE. Both methods determine the total amount of fluoride in the solution, which is the sum of the free fluoride and the reaction product silicon hexafluoride (SiF_6^{2-}).

3.1.1 TITRATION WITH LA(NO_3)$_3$

Titration is a well-established analysis method, especially for the determination of acids and bases. In addition, a precipitation titration was developed for the determination of the fluoride concentration in acidic texturization baths containing HF and HNO_3 by the group of Acker [16]. The precipitation titration is performed with lanthanum nitrate $La(NO_3)_3$. It bases on the high affinity of fluoride to heavy ions, like thorium or lanthanum, leading to the formation of precipitated ThF_3 and LaF_3, respectively. Since the pH is monitored during analysis and the fluoride concentration is calculated from the required volume of $La(NO_3)_3$, it is referred to as an indirect analysis method.

The two-step analysis is performed as follows: In the first step, the adjustment of the pH of the diluted sample to 6.5 - 7.5 with sodium hydroxide solution (NaOH) is required to free the fluoride ions from SiF_6^{2-}.

$$SiF_6^{2-}{}_{(aq)} + 4\ OH^-{}_{(aq)} \rightarrow Si(OH)_{4\,(s)} \downarrow + 6\ F^-{}_{(aq)} \tag{3.1}$$

Above pH 7 all the fluoride in the sample exists as uncombined fluoride ions as Figure 16 demonstrates on page 21 [75]. Subsequently, the addition of $La(NO_3)_3$ leads to the reaction of the fluoride with the La^{3+}. This is the second step of the precipitation titration; the solubility product of LaF_3 is $K_S = 2.5 \cdot 10^{-18}$ l/mol as taken from [76].

$$La^{3+}_{(aq)} + 3\ F^-_{(aq)} \rightleftharpoons LaF_{3\ (s)}\downarrow \tag{3.2}$$

Once all the fluoride from the sample reacted properly, the following reaction takes place. The solubility product of $La(OH)_3$ is $K_S = 1.1 \cdot 10^{-19}$ [77].

$$La^{3+}_{(aq)} + 3\ H_2O_{(l)} \rightleftharpoons La(OH)_{3\ (s)}\downarrow + 3\ H^+_{(aq)} \tag{3.3}$$

This reaction is the reason for the fast decrease of the pH at the equivalence point indicating the endpoint of the titration. The knowledge of the required volume of $La(NO_3)_3$ to reach the equivalence point is necessary for the calculation of the amount of substance of the fluoride ions taking part in the reaction described by equation (3.2). Therefore, the precise $La(NO_3)_3$ concentration is essential for the accuracy of the measurement.

Experimental details

An automatic titration device from Mettler Toledo (Model DL28, Mettler Toledo, Greifensee, Switzerland) is equipped with a stirrer, a fluoride resistant glass pH-electrode (InLab 429 from Mettler Toledo), a thermal element, and two burettes. The method requires dilution of the PSI etching bath sample in order to obey the tolerance zone of the electrode regarding the fluoride concentration. In most cases, dilution of 1:200 is sufficient.

In the first step of the titration, the pH of the diluted sample is adjusted to 6.5 - 7.5 with sodium hydroxide solution (NaOH, 1 mol/l, standardized solution, Alfa Aesar, Germany). After successful adjustment of the pH, the determination step follows in which lanthanum nitrate ($La(NO_3)_3$, 0.1 mol/l, volumetric solution, Sigma-Aldrich, Germany) is added to the sample solution. The total time of the two-step determination is about 15 minutes. We repeated each measurement in order to estimate the result's accuracy. Please see chapter 3.4 below as well as Appendix B for a detailed investigation of the measurements uncertainty.

We found the pH-electrode plugged with precipitated lanthanum hydroxide $La(OH)_3$ after about 20 services according to equation (3.3). The plugging was indicated by a calibration slope that was beyond the limit of tolerance as given by the manufacturer. Therefore, cleaning of the electrode is recommended [78] and performed by storage of the electrode in 0.1 mol/l hydrochloric acid (diluted from HCl, 37%, semiconductor grade VLSI PURANAL®, Honeywell, Germany) overnight and, subsequently, in saturated potassium chloride solution (KCl, p.a., Merck KGaA, Germany) for at least one hour. The calibration of the electrode is mandatory before further analysis and is performed with four buffer solutions of pH 1, pH 4, pH 7 and pH 9; a weekly calibration is adequate.

Since the concentration of the $La(NO_3)_3$ solution affects the accuracy of the result, the concentration was monitored once a month by a nitrate ion-selective electrode (DX 262 by Mettler Toledo).

Practical issues

The titration has several advantages, since it is an operational method that allows for fast analysis. Furthermore, it enables the determination of the whole fluoride concentration range of the PSI etching bath through adjustment of the sample volume. The concentration range of the initial electrolyte ranges from 19.5 mol/l to 13 mol/l of fluoride.

The disadvantages of titration are mainly the cost-intensive lanthanum nitrate solution (132 € per liter standard solution in June 2014, Sigma-Aldrich) and the fact that only the total fluoride concentration of the sample is accessible. Since the concentration of free fluoride is important for etching, the identification of the bound fluoride concentration is essential. Thus, a method for the determination of the reaction product SiF_6^{2-} is required. The periodic observable plugging with precipitated $La(OH)_3$ is a further disadvantage concerning the maintenance of the electrode.

3.1.2 FLUORIDE ION-SELECTIVE ELECTRODE (F-ISE)

In the present work, the fluoride ion-selective electrode (F-ISE) was investigated as an alternative method for the determination of the fluoride concentration in the etching baths. The F-ISE was developed by Frant and Ross in 1966 [79]. Figure 17 shows the schematic structure of the F-ISE consisting of the internal Ag/AgCl reference electrode and the fluoride sensitive membrane at the tip. The membrane is a crystal of lanthanum fluoride LaF_3, which is doped with Eu^{2+} in order to increase the conductivity. While the potential of the internal Ag/AgCl electrode is fixed by the activity of the chloride ions (from KCl), the activity of the fluoride ions inside the electrode (from KF) controls the potential of the LaF_3 crystal. Therefore, if the tip of the ISE is immersed into a fluoride containing sample solution, an electrical potential difference is established across the LaF_3 crystal, whose magnitude depends on the ratio of the fluoride ion activities in the inner and outer solution [80]. The determination of the fluoride concentration in the sample solution results from the Nernst equation

$$E = E^0 + \frac{RT}{zF} \ln a \qquad (3.4)$$

where E [mV] is the measured total potential between the ISE and the internal reference electrode, E^0 [mV] is the standard electrode potential, R is the universal gas constant [8.3145 J mol^{-1} K^{-1}], T the temperature [K], z is the charge of the ion, F is Faraday's constant [96485 C mol^{-1}], and a the activity of the analyte ions in the sample. Contrary to titration, the determination of the fluoride concentration with the F-ISE is a direct analysis method due to the measurable effect of the fluoride ions on the potential.

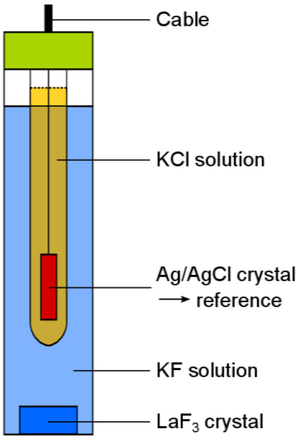

Figure 17: Schematic representation of the F-ISE.

The Nernst equation involves the activity of the fluoride ions. In order to access the concentration instead, an inert and highly concentrated electrolyte is added to the sample solution resulting in a high ionic strength. In the present work, TISAB II (Total Ionic Strength Adjustment Buffer of type II, especially for the determination of fluoride) is used for this purpose. This electrolyte has the advantage to protect the ISE from interferences with OH^- ions since the pH is kept constant at about 5.5 [81]. Hydroxide ions would lead to the formation of lanthanum hydroxide $La(OH)_3$, and consequently to the liberation of fluoride ions from the LaF_3 crystal according to:

$$LaF_{3\,(s)} + 3\,OH^-_{(aq)} \rightleftharpoons La(OH)_{3(s)}\downarrow + 3\,F^-_{(aq)} \qquad (3.5).$$

Experimental details

The titrator from Mettler Toledo is applicable for the operation of ion-selective electrodes. For the determination of fluoride we used a perfectION^{TM} combination fluoride electrode from Mettler Toledo. The calibration of the F-ISE is performed with aqueous standard solutions of sodium fluoride (NaF, BioXtra, Sigma-Aldrich, Germany) in the range from 0.53 mmol/l to 53 mmol/l (corresponding to 10 - 1000 ppm) with the latter being the stock solution. An exemplary calibration curve is attached to Appendix C.

Before measurement, the etching bath samples are diluted from an initial fluoride concentration of 19.5 mol/l to about 6 mmol/l by a dilution factor of 1:3700. The sample preparation is completed by the addition of 1 ml of TISAB solution (TISAB II solution, Sigma-Aldrich, Germany) to 50 ml of the diluted sample, keeping the pH at 5.8. TISAB is added to both, sample solution and calibration solution, before measurement. A period of five minutes is sufficient for the establishment of the equilibrium resulting in an acceptable stability of the measured potential with a reproducibility within 1 mV. Again, we repeat the determination in order to ensure the accuracy of the result. A detailed investigation of the measurements uncertainty is attached to Appendix B.

Practical issues

The advantage of the F-ISE is clearly the stability of the measured potential in combination with a strong sample dilution that permits less strict safety arrangements during the analysis. However, the barely existing disadvantages are the long preparation time and the calibration required prior to the analysis [78].

Generally, the appropriate dilution of the etching bath samples lead to satisfying results without further adjustment of the method.

3.2 DETERMINATION OF SURFACE WETTING AGENTS

The surface wetting agents are used in electrochemical etching baths to reduce the surface tension of the electrolyte. At the ISFH, the wetting agent in the MacPSI etching bath is acetic acid, whereas in the PSI etching bath the wetting agent is ethanol. The wetting agents support the release of the hydrogen that is formed during the etching process at the Si surface according to equation (2.2) [69]. The detachability of the hydrogen bubbles is significant especially for static etching baths without movement of the electrolyte, i.e., for the PSI etching bath. In comparison, the MacPSI bath at ISFH is moved through a periodic tilting of a rocking table. We found that acetic acid is beneficial for the etching process but not mandatory as ethanol is for the PSI process.

The high reactivity of the fluoride ions in the etching baths – especially in the PSI bath – restricts the number of applicable methods for the analysis of the organic wetting agents. A precondition is the capability of resistance against fluoride. Methods that detect organics in very low concentrations are adequate since they allow the strong dilution of the samples in order to diminish the influence of the fluoride ions. This is the case for the cuvette test method by Hach Lange. Here, the total organic carbon content (TOC) is detectable. The TOC is the difference from the total carbon (TC) and the total inorganic carbon (TIC) in the sample; each of it is determined by its own cuvette [82]. The inorganic carbon represents the carbonate, for example, which is not expected to be present in the etching solutions of pH 1. Thus, the appropriate inorganic carbon cuvette is filled with distilled water for the measurement and has no impact on the result. The organic carbon in the electrolyte is represented by the total carbon content; accordingly, the total carbon cuvette is used for the determination of the concentration of the wetting agents in the investigated electrolytes for the PSI and MacPSI process. Figure 18 shows the schematic representation of a typical total carbon cuvette.

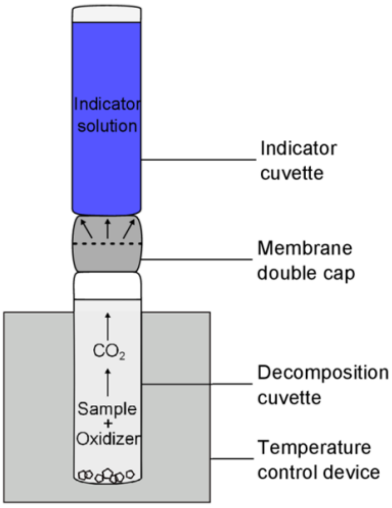

Figure 18: Schematic representation of a cuvette LCK 380 for the determination of the total carbon content in electrochemical etching baths [78].

In Figure 18, the lower part of the cuvette depicts the decomposition cuvette containing lithium hydroxide (LiOH), sodium sulfate (Na_2SO_4), and sodium persulfate ($Na_2S_2O_8$) as an oxidizing agent. Moreover, the decomposition cuvette contains the diluted sample. The upper cuvette contains thymol blue as an indicator solution and is connected to the decomposition cuvette via a semipermeable membrane double cap. Following the difference method of Hach Lange [82], the connected cuvettes are heated to 100 °C for two hours in a temperature control device. Thereby, the organic wetting agent is oxidized to CO_2 which passes the gas permeable membrane double cap. The CO_2 causes a color change of the indicator solution; Figure 19 shows the color of thymol blue solutions after analysis of various concentrated ethanol samples in the range of 0 to 50 mg/l TOC. After cooling down to room temperature, the color of the indicator solution is evaluated by photometry and the result of total organic carbon is given in mg/l. In order to gain uniformity in this work, the results will be converted to mol/l in the following from now on.

Figure 19: Color changes of the cuvette test indicator solutions according to the concentration of total carbon in the sample: Initial color, 10 mg/l, 25 mg/l, 35 mg/l, and 50 mg/l TOC (from left to right) [78].

Experimental details

We use the cuvette test method by Hach Lange (HACH LANGE GmbH, Düsseldorf, Germany) with the LCK 380 cuvettes for the determination of the total organic content (TOC). The method is sensitive to organic compounds in concentrations of 0.08 mmol/l to 2.7 mmol/l representing the calibration range. The calibration is performed with aqueous solutions of potassium hydrogen phthalate ($C_8H_5KO_4$, primary standard, ACS, Alfa Aesar, Germany).

Samples from the PSI etching bath contain ethanol concentrations ranging from about 3.0 mol/l to 5.7 mol/l. Therefore, the samples are diluted by a factor of 1:3300 to be within the calibration range. For the MacPSI etching bath with an acetic acid concentration of about 1.14 mol/l a dilution of 1:550 is sufficient.

The photometric measurements are performed at a wavelength of 430 nm with an ISiS 6000 photometer (Hach Lange). Figure 20 shows the characteristic absorbance spectrum of thymol blue according to [83].

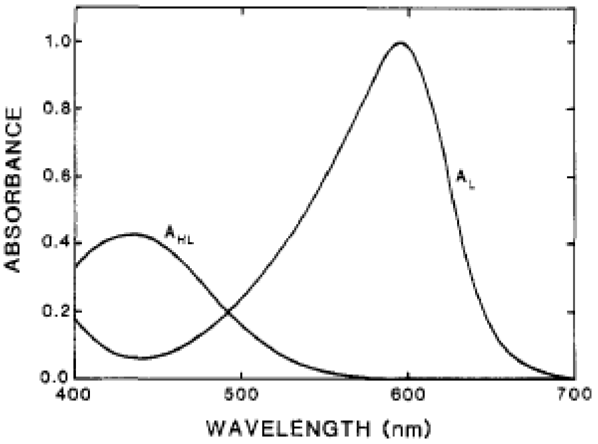

Figure 20: Characteristic absorbance curves for thymol blue at 25 °C, reprinted with permission from [83]. *HL* indicates the protonated form, *L* the unprotonated form.

Practical issues

The cuvette test method is – despite its complex configuration – comfortable to handle. The advantage of the system is its accuracy for low organic concentrations enabling the determination of the organic wetting agents in the presence of fluoride. However, the analysis requires four hours, which is clearly a disadvantage of the method. Furthermore, it is not capable for inline analysis and, thus, for industrial application.

3.3 DETERMINATION OF DISSOLVED SILICON

The concentration of the reaction product silicon hexafluoride (SiF_6^{2-}) increases during the lifetime of the etching bath leading to a decrease in the concentration of the HF species. From here, the remaining HF species in the bath that are not bonded to Si are termed as "free fluoride" $[F^-]_{free}$. The concentration $[F^-]_{free}$ is calculated as the difference of the total fluoride concentration in the etching bath $[F^-]_{total}$ and the concentration of the reaction product SiF_6^{2-}, i.e., the bonded fluoride $[F^-]_{bonded}$.

$$[F^-]_{free} = [F^-]_{total} - [F^-]_{bonded} \qquad (2.22)$$

The determination of $[F^-]_{total}$ is performed by the methods described in chapter 3.1, which is titration and F-ISE. The concentration of the fluoride bonded as SiF_6^{2-} is accessible through the dissolved Si concentration in the etching bath.

$$[F^-]_{bonded} = 6\,[SiF_6^{2-}] \qquad (3.6)$$

We found that the concentration of SiF_6^{2-} of the PSI etching bath is not amenable to titrimetric acid-base analysis methods reported in literature [17,18]. The reason is the large difference in the concentration between fluoride and SiF_6^{2-} of 19.5 mol/l and 0.05 mmol/l, respectively, after porosification of 200 wafers as demonstrated in Figure 15 on page 21. A requirement for the Si determination by titration is a strong dilution of the sample in order to prevent the electrode from damage by the high fluoride concentration used in the PSI etching bath. Consequently the Si concentration decreases by dilution, too, and is not accessible for titration anymore.

Ion-chromatography (IC) is a standard analysis tool for the precise determination of ionic analyte traces in aqueous solutions. Therefore, it is applicable for strongly diluted samples of the etching baths investigated in this work. Details concerning the IC can be found in literature [84,85]. In general, the analyte sample is forced by high pressure to flow through the system that is permanently flushed with an eluent solution. The heart of the IC is the separation column that splits the sample according to the charge or size of the constituents. Various separation techniques are available; columns are either applicable to separate anions or cations. The detector measures the conductivity of the eluent in the system with respect to the time. The identification of the analyte is related to the time the analyte requires to pass the column and the measured peak area correlates to the amount of the analyte in the sample.

The IC system used in this work is equipped with an anion-exclusion column, which separates weak acids or non-ionic substances from strong ionic systems. This column contains a totally sulfonated high-capacity cation exchange resin made from a polystyrene-divinylbenzene copolymer. Water molecules form a hydration shell around the sulfonic acid groups leading to a negatively charged layer, which is analogous to a Donnan layer depicted in Figure 21. This layer excludes negatively charged ions like SiF_6^{2-} and is only permeable for non-dissociated acids like HF that could diffuse into the pores of the resin [84,85]. Considering the pH of the eluent, i.e., pH 3, and Figure 16 on page 21, the main fluoride species in our samples are HF and H_2F_2.

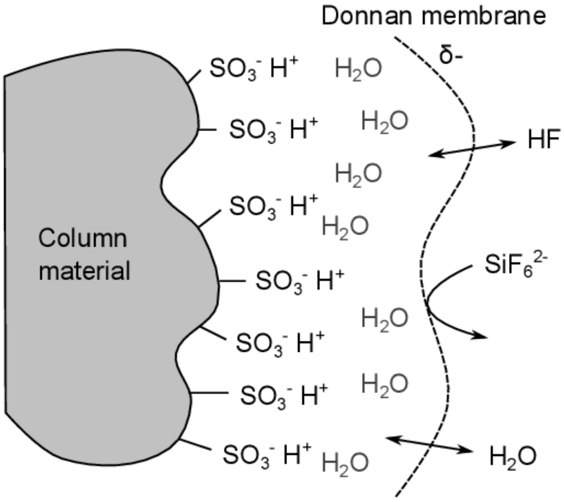

Figure 21: Schematic representation of the separation process in an anion-exclusion column redrawn from [85].

The determination of the dissolved silicon SiF_6^{2-} requires the upgrade of the standard IC system with a post-column derivatization device. Figure 22 illustrates the schematic setup of the IC system used for the analysis of the etching baths in this work.

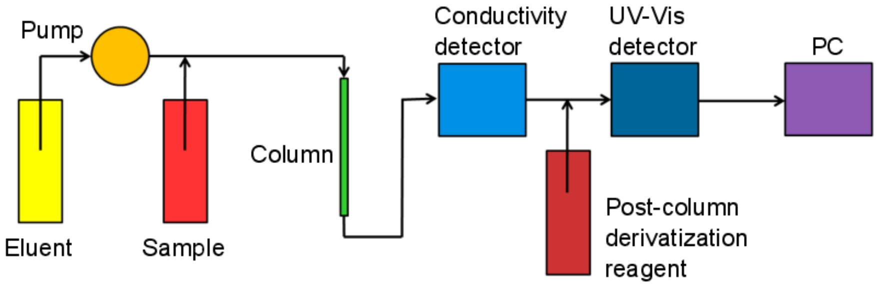

Figure 22: Schematic setup of the IC system with post-column derivatization.

The SiF_6^{2-} is only stable in acidic aqueous solutions and will decompose in contact with the eluent used in this work. The separated fluoride ions are detected by the conductivity detector after passing the anion-exclusion column. The analysis of the Si^{4+} ions is performed by post-column derivatization and subsequent determination with a UV-Vis detector. The origin of this well-established method is based on the phosphorantimonylmolybdenum blue method for the analysis of the phosphate concentration in brackish water [86,87]. Sodium molybdate dihydrate $Na_2MoO_4 \cdot 2H_2O$ is used as the post-column derivatization reagent. In acidic media, the monomolybdates convert to polymolybdates through condensation reactions. Polymolybdates form a UV active complex with silica ions according to equation (3.7) [88]. This complex is of a yellow color and has an extinction of 0.720 reported for a wavelength of 400 nm [89]. However, the appropriate wavelength range for measurements is either located between 330-340 nm or 370-440 nm according to Lange and Vejdělek [90].

$$[Mo_{12}O_{40}]^{6-} + Si^{4+} \rightleftharpoons [Si(Mo_{12}O_{40})]^{2-} \tag{3.7}$$

Experimental details

A Compact IC 881 (Deutsche Metrohm, Filderstadt, Germany) is equipped with an anion-exclusion column (Metrosep Organic Acids, Metrohm). The IC system is further equipped with a post-column derivatization device. The post-column derivatization reagent is added to the sample solution after passing the anion-exclusion column and, subsequently, forms a UV active complex with the silica ions. The yellow silicomolybdate complex is detected in the present work at a wavelength of 410 nm with a UV-Vis photospectrometer (wavelength range 190-900 nm, BlueShadow Detector 50D, Wissenschaftlicher Gerätebau Dr. Ing. Herbert Knauer GmbH, Berlin, Germany). The peak areas are integrated automatically by the software MagIC Net 2.4 (Metrohm), in which a grading of the UV-Vis detection signal is performed using a Savitzky-Golay filter (length 5).

The eluent is 0.5 mmol/l sulfuric acid (from H_2SO_4, 96%, VLSI Selectipur®, BASF SE, Germany), the post-column derivatization reagent 20 mmol/l sodium molybdate dihydrate ($Na_2MoO_4 \cdot 2\,H_2O$, ACS reagent, Alfa Aesar, Germany) with 200 mmol/l nitric acid (from HNO_3, 69%, VLSI Selectipur®, BASF SE, Germany). Calibration is performed with standard solutions between 0.02 and 0.36 mmol/l Si prepared from hexafluorosilicic acid H_2SiF_6 solution (35 wt% in H_2O, Alfa Aesar, Germany).

Dilution of the etching bath samples is required in order to avoid damage of the system with respect to the fluoride concentration. For PSI samples, a dilution of 1:500 is convenient for both, the determination of the Si traces as well as for safety reasons. Samples with expected Si concentrations below 0.04 mmol/l after dilution – representing the detection limit as reported by the manufacturer – have their Si concentrations raised with a 0.18 mmol/l standard solution prepared from H_2SiF_6 solution. MacPSI etching bath samples experience a dilution of 1:250 leading to a Si concentration above 0.3 mmol/l. Therefore, a concentration raise is not necessary.

The consistency of the analysis is followed with check standards of 0.18 mmol/l and 0.36 mmol/l. The calibration solutions are renewed if the deviation is more than 10%.

Practical issues

The high amount of fluoride in the PSI samples prevents the use of a standard anion-exchange column due to an observed disturbance in the Si signal. The disturbance caused negative peaks in the chromatogram located where the Si peak was expected. This observation is in contrast to the work of Zimmer et al. who used a standard anion-exchange column for the determination of the Si^{4+} in acidic texturization baths [22]. However, as a result of this work, for the PSI etching bath an anion-exclusion column is required due to the great difference of the Si^{4+} to the fluoride concentration. The column delays the outlet of the main fluoride species in the samples, i.e., HF and H_2F_2 due to the reaction with the Donnan layer. However, HF_2^- is able to pass the column without interaction. In summary, the disturbance of the Si signal is delayed and the detection of Si is possible. Figure 23 shows the difference in the Si signals as obtained with the anion-exchange column and the anion-exclusion column.

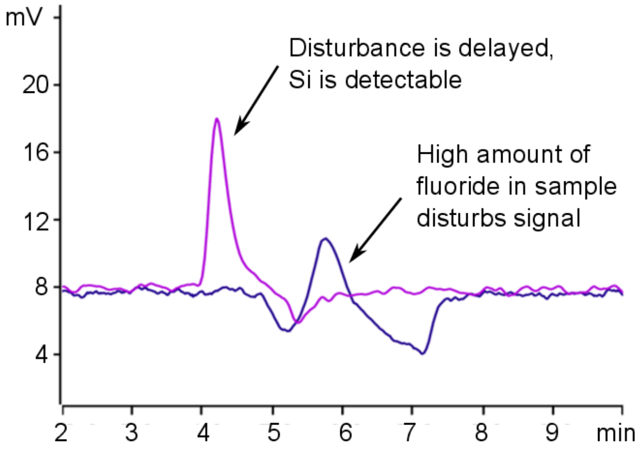

Figure 23: Silicon signals obtained with the anion-exchange column (in blue) and anion-exclusion column (in lavender) for samples of the PSI etching bath.

Special attention has to be paid to the UV-Vis detector whose lamps apparently require a couple of hours for stabilization before analysis. Thus, leaving the UV-Vis detector switched on overnight enables stable measurements the following day. Furthermore, the post-column derivatization reagent ages within days. This becomes noticeable by precipitation and non-reproducible analysis results. However, if those issues are considered, IC is a reliable, inline-capable analysis method for the Si determination of the etching baths investigated in this work. The advantage of the IC is clearly the possibility of the direct Si^{4+} determination in contrast to the indirect methods reported in the literature [17,18]. These indirect methods require complex sample preparations and are, therefore, limited for the use of very low concentrations of Si.

3.4 EVALUATION OF METHODS

The accuracy of the fluoride determining methods is essential for the replenishment of the PSI etching bath discussed in chapter 4.1.2 on page 46. Therefore, the reliability of the fluoride determining methods is investigated here: the quality of the measurements is estimated with respect to the comparability of both methods and their recovery rates. Furthermore, the results are compared to reference measurements obtained from a well-established analytical laboratory. The recovery rates of the cuvette test method and of IC are evaluated in addition. Moreover, the uncertainties of the measurements are addressed. A detailed description of the determination of the uncertainties as well as the corresponding recovery rate data for all methods investigated in this work are attached to Appendix B and C.

The determination of the recovery rate of an analytical method allows for statements concerning the quality and the accuracy of the obtained results with respect to the surrounding matrices. Therefore, the recovery rate R_R is calculated for the methods introduced above following

$$R_R = \frac{[\mathrm{Analyte}]_{\mathrm{actual}}}{[\mathrm{Analyte}]_{\mathrm{target}}} \cdot 100 \tag{3.8}$$

where $[Analyte]_{actual}$ is the measured concentration of the analyte determined by the investigated analysis method and $[Analyte]_{target}$ is the target concentration of the analyte. The analytes are the total fluoride ions, ethanol or the silicon ions. The target concentrations cover the relevant range for each chemical analysis method. A perfect recovery rate equals 100%.

3.4.1 ANALYSIS METHODS FOR FLUORIDE

Titration and F-ISE were selected for the determination of the fluoride concentration in the PSI etching bath. For the determination of the recovery rate, fluoride samples were prepared with and without ethanol. The fluoride concentration varied from 65-110% of the common etching bath concentration and covered the relevant range for chemical analysis. The recovery rate R_R is calculated according to equation (3.8) and gives values of (100±1)% for both fluoride determining methods.

The uncertainties of the titration and F-ISE were determined to 0.3 mol/l for PSI samples (see Appendix B). Figure 24 shows a comparison of titration and F-ISE results within the analysis of 39 samples [78]. Two data points correspond to each sample; the fluoride concentration determined by F-ISE is marked by the white diamonds and is always below the result of the titration as marked in black circles. Replenishments are indicated by steps in the fluoride concentration, the first replenishment of the etching bath has been performed after 13 samples with 50 wt% HF to increase the fluoride concentration in the electrolyte. Subsequently, rising fluoride concentrations indicate further replenishments. For these particular titration results, the concentration of the lanthanum nitrate solution was determined to 0.096 mol/l with a nitrate ion-selective electrode. The deviation between the analysis results is within the experimental uncertainty. Thus, titration and F-ISE are considered as comparable methods for the determination of the fluoride concentration.

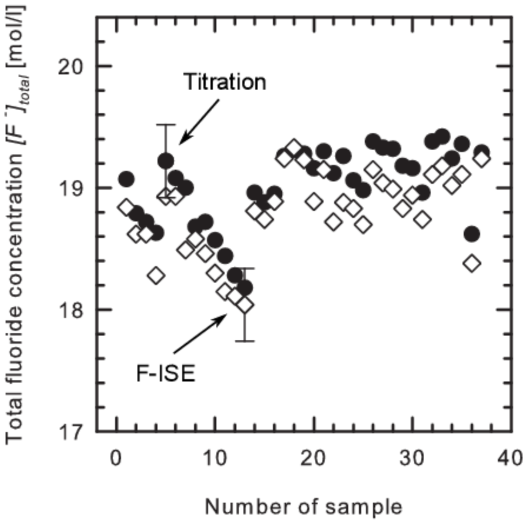

Figure 24: Conformity test of data points obtained from titration (black circles) and F-ISE (white diamonds) for 39 etching bath samples of different fluoride concentrations [78]. For each method, just an example of the uncertainty is given for the sake of clarity.

The validation of the titration and F-ISE results was further verified by reference measurements at BASF SE (Ludwigshafen, Germany) as shown in Table 3.1. These reference measurements at BASF SE were performed by IC. The etching bath samples under investigation were taken initially after preparation of a fresh electrolyte and after etching of about 250 wafers. Furthermore, a sample without ethanol was analyzed in order to demonstrate that the measured result is independent of the existence of ethanol in the sample. Small deviations in the results between the F-ISE and the reference measurements are observable. However, the overall accuracy is still satisfying; especially concerning the consistency of the titration results compared to the reference measurements.

As a result, the titration was the method of choice for the investigation of the fluoride concentration of the PSI etching bath as described in detail in chapter 4.1.

Table 3.1: Verification of the accuracy of the chemical analysis methods used at ISFH by measurement of three different sample types. BASF SE used High Performance Ion Chromatography (HPIC) for the determination of the fluoride content. All samples were measured twice, given is the mean value.

	Titration (ISFH) [mol/l]	F-ISE (ISFH) [mol/l]	HPIC (BASF SE) [mol/l]
Initial etching bath	20.0 ± 0.3	19.4 ± 0.3	20.3 ± 0.6
Used etching bath	19.9 ± 0.3	19.1 ± 0.3	19.4 ± 0.7
Etching bath without ethanol	20.5 ± 0.3	19.6 ± 0.3	20.5 ± 0.5

In this work, the precipitation method of Acker et al. [16] was adapted to the electrochemical etching bath containing aqueous HF and ethanol. It was demonstrated, that ethanol has no influence on the accuracy of the result. Furthermore, the detectable fluoride concentration range was slightly increased for the titration method to > 0.1 mol/l after dilution compared to the work of Acker et al.

3.4.2 CUVETTE TEST METHOD FOR WETTING AGENTS

The determination of the recovery rate of the cuvette test method was performed for ethanol samples in EtOH-H_2O and HF-EtOH-H_2O solutions in order to investigate whether the HF has an impact on the result. The investigated solutions contain 70% and 130% of the initial ethanol concentration in the PSI etching bath, which is 5.7 mol/l. The recovery rate R_R for the cuvette test method is (100 ± 1.5)%, an exception being the 130% EtOH-H_2O sample with a deviation of 2.9%. Altogether, the recovery rate testing demonstrates satisfying results without an observable impact of the HF.

The uncertainty of the cuvette test method was determined to 0.01 mol/l for the PSI and to $5 \cdot 10^{-3}$ mol/l for the MacPSI electrolyte; the difference is due to the initial sample concentration in the bath. Therefore, the determination of the organic contents indicates a high accuracy concerning the etching baths investigated in this work.

3.4.3 ION-CHROMATOGRAPHY FOR DISSOLVED SILICON

The PSI etching bath samples require a dilution of 1:500 due to the high concentration of fluoride in order to avoid the damage of the system and for safety reasons. As a consequence, the PSI etching bath samples should contain at least about 7 mmol/l Si before dilution in order to be detectable by IC.

The recovery rate R_R of the IC measurements was verified by the determination of synthetic solutions containing SiF_6^{2-} in water and in HF-EtOH-H_2O. The concentrations of Si were 0.07 mmol/l, 0.18 mmol/l, and 0.29 mmol/l. Recovery rates between 94.4% and

110.4% were found, indicating an accuracy of the measurements that is to some extent satisfying taking into consideration the low Si concentration in the samples.

The uncertainty for the PSI samples exhibits to be 1.7 mmol/l, whereas the uncertainty of the more concentrated MacPSI samples is 18.2 mmol/l.

Due to the low Si concentrations, the PSI samples have their original concentrations raised with a 0.18 mmol/l stock solution made from H_2SiF_6. The accuracy of this procedure was investigated in terms of the accuracy. Therefore, 10-fold measurements were performed for a 0.18 mmol/l and a 0.21 mmol/l Si stock solution, respectively, in order to determine the standard deviations. For the 0.18 mmol/l stock solution an accuracy of (0.180 ± 0.002) mmol/l was found, whereas the accuracy for the 0.21 mmol/l stock solution is (0.223 ± 0.006) mmol/l. As a result, IC measurements are able to detect differences in the Si concentration of about 0.04 mmol/l. If the PSI sample contains less than 0.04 mmol/l the concentration raise is performed.

Finally, IC is generally applicable for the determination of low Si concentrations in the electrochemical etching baths investigated in this work.

3.5 CONCLUSIONS

In this chapter, the analysis methods for electrochemical etching baths used in this work were introduced. Theoretical and experimental details were given for each method. Furthermore, the results obtained were evaluated according to their accuracy and reliability.

For the determination of the total fluoride content in the PSI bath two methods were evaluated, precipitation titration with $La(NO_3)_3$ and fluoride ion-selective electrode. Both give accurate results and are applicable for inline-analysis in case of an industrial application of the PSI process. From both methods, we chose the titration method for everyday analysis in the laboratory. The main advantage of titration is the quick attendance of the system since calibration is required only once a week. In addition, the titration results harmonize with the external arranged reference measurements.

The cuvette test method by Hach Lange was introduced and investigated in terms of the analysis of the organic wetting agents. Although the cuvette test method requires four hours for analysis, the accuracy of the method and the resistance against HF are convincing.

Ion-chromatography with post-column derivatization was evaluated for the determination of the dissolved silicon as Si^{4+}. A challenge in the implementation of the method surely was the very low amount of dissolved Si near the overwhelming amount of fluoride. However, the use of the anion-exclusion column in combination with an appropriate use of the post-column derivatization reagent Na_2MoO_4 led to a reasonable recovery rate. Therefore, the method proved its benefit for the determination of low SiF_6^{2-} concentrations near high amounts of fluoride.

In the following chapter, these methods are applied to the electrochemical etching baths for the formation of meso- and macroporous Si at ISFH.

4 APPLICATIONS OF CHEMICAL ANALYSIS

This chapter deals with the application of the chemical analysis methods as introduced in chapter 3. The concentrations of the constituents of the electrochemical etching baths for the PSI and the MacPSI process are investigated here. The PSI bath, on the one hand, consists of HF as the etching reagent, ethanol as the wetting agent and SiF_6^{2-} as the reaction product. On the other hand, the MacPSI electrolyte contains HF, acetic acid as the wetting agent, and of course the reaction product SiF_6^{2-}.

The benefits of chemical analysis for the PSI etching bath are addressed, which are the identification of the source of HF loss as well as the possibility of replenishment. Furthermore, the results are merged into the development of an improved etching tool design with industrial relevance that has been established at ISFH during this work. For a better comparability, all concentrations are given as a function of the number of etched wafers. The concentrations are not related to the lifetime of the electrolyte. This is due to the various periods of time that the baths have been used until they were disposed of.

The measurement uncertainties shown in the figures of this chapter are related to the determination of the uncertainties in Appendix B. Besides, detailed information concerning the data points of each figure is given in Appendix D.

4.1 PSI ETCHING BATH

Before the implementation of the chemical analysis at ISFH, the constituents of the PSI etching bath have not been analyzed at all. As a result, the electrolyte has been disposed of as soon as the porous layers have not been detachable from the substrate or the lift-off was incomplete leading to cracked, imperfect layers as mentioned in chapter 2.3 on page 19. Consequently, the disposal rate has been high with an average bath lifetime of about 10 - 14 weeks or about 250 etched wafers. Hence, the institute has suffered from high personnel effort for PSI etching (change of barrels, preparation of new electrolyte solutions under strict safety instructions) as well as from high financial costs (disposal of about 15 liter of exhausted electrolyte). Therefore, the possibility to replenish the PSI electrolyte has been highly desired in order to extent the bath lifetime.

4.1.1 SITUATION BEFORE THE START OF CHEMICAL ANALYSIS

A motivation to start with chemical analysis has been the high HF consumption observed for the PSI process. Thus, there were two aims considering the chemical analysis: The possibility to replenish the electrolyte in order to keep the HF concentration constant as well as the identification and, resultant, the minimization of the reasons for the observed loss of HF.

All HF concentrations of this paragraph were determined with precipitation titration with lanthanum nitrate according to chapter 3.1.1 on page 26.

Figure 25 illustrates exemplarily the development of the total fluoride concentration $[F^-]_{total}$ in the ISFH etching tool at the beginning of the chemical analysis.

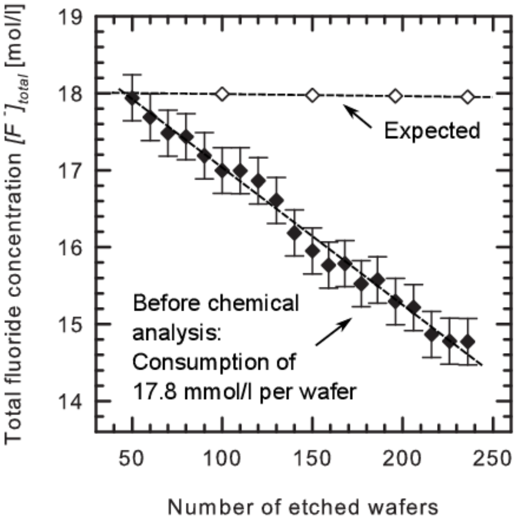

Figure 25: Decrease of the total fluoride concentration $[F^-]_{total}$ (in black diamonds, each representing two measurements) at the beginning of the chemical analysis in the ISFH etching tool determined by titration. The theoretical concentration of $[F^-]_{total}$ (in white diamonds) is constant throughout the investigated period.

The samples of the etching bath were analyzed during the bath lifetime of 14 weeks. The concentration $[F^-]_{total}$ decreased rapidly within 236 porosified wafers leading to a theoretical consumption of 17.8 mmol F^-/l per etched wafer. However, by taking into consideration the moles of reacted fluoride, the theoretical concentration of fluoride is expected to be constant. Table 4.1 provides details concerning the amount of HF (50 wt%) that is required to replace the loss of HF. The data were calculated considering the consumption of 6 mol fluoride per mol dissolved Si according to equation (2.2) and an etching bath volume of 14.9 l. As a result, the experimentally observed amount of HF required for porosification was more than 60-times the expected amount. Therefore, the PSI process was far from being economically acceptable for an industrial application at this point.

Due to the high HF consumption, the electrolyte of the etching bath presented in Figure 25 was exhausted and disposed after 236 wafers. The replenishment of the bath in order to replace the consumed HF has not been realized so far.

Table 4.1: Comparison of the HF consumption for the electrochemical etching of PSI layers in theory and with the ISFH tool before chemical analysis. It is assumed that 20 mg Si per wafer are dissolved. Experimental data are labeled with an asterisk *.

	Dissolved Si [g]	Dissolved Si [mmol]	Consumed HF [mmol]	Consumed HF [mol/l]	Replenishment with HF (50 wt%) [ml]
Theoretical					
1 wafer etched	0.02	0.71	4.3	0.0003	0.01
100 wafers etched	2.00	71.21	427.3	0.0287	1.00
236 wafers etched	4.72	168.1	1008.3	0.0677	2.36
ISFH tool*					
1 wafer etched	0.02	0.71	265.2*	0.0178*	0.62
100 wafers etched	2.00	71.21	26 522*	1.7800*	61.94
236 wafers etched	4.72	168.1	62 591*	4.2008*	146.19

The large discrepancy of theoretical and experimental data indicates that the consumption of HF in the etching process was not the sole reason for the observed high total consumption. Therefore, the evaporation of the electrolyte from the reservoir was investigated. We monitored the HF concentration for a couple of days without etching. Figure 26 shows the decrease of the HF concentration in the electrolyte caused by evaporation.

The average loss of HF is about 0.08 mol/l per day. An explanation is that the ISFH etching tool is not hermetically sealed due to safety reasons because the electrolyte is a potentially explosive mixture. Consequently, the loss of HF due to evaporation out of the reservoir had to be accepted and clearly demonstrated the importance of chemical analysis for the PSI process.

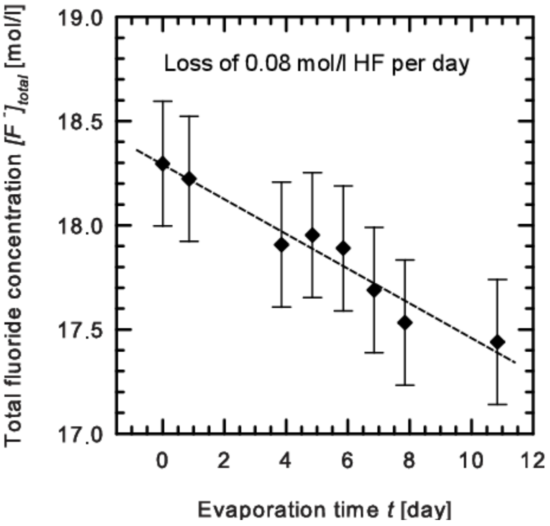

Figure 26: Loss of HF due to evaporation of electrolyte out of the reservoir of the ISFH tool without etching.

The longer the lifetime of the electrolyte, the more HF evaporates and the earlier the performance of the electrolyte is below expectations. This is the reason why the comparison of the electrolytes is difficult. For example, electrolyte A might be used for six weeks and etch 200 wafers during that time; electrolyte B might stand for a month without etching and might be discarded after only 130 wafers but a lifetime of three months. Therefore, the concentrations of the etching bath constituents will be followed over the number of etched wafers from now on.

4.1.2 BENEFITS OF CHEMICAL ANALYSIS FOR THE PSI PROCESS

Replenishment

The chemical analysis of the PSI electrolyte enables the investigation of the development of the HF concentration in relation to the number of etched wafers. Possible losses of HF – as described above – were identified and led to a better understanding of the ISFH tool. Another positive aspect of chemical analysis is the possibility to replenish the fluoride that evaporated or was consumed through the porosification of the Si wafer. The replenishments keeps the free fluoride concentration $[F^-]_{free}$ constant and, therefore, enlarges the usability the electrolyte.

At ISFH, the replenishment of the PSI electrolyte is usually performed with HF (50 wt%) at the beginning of a laboratory day. The required volume of HF $V_{Replenish}$ is calculated from the analytical results for the total fluoride concentration $[F^-]_{total}$ according to

$$V_{Replenish} = \frac{\left([F^-]_{initial} - [F^-]_{total}\right) \cdot V_t \, M_{HF}}{a \cdot \rho_{HF}} \qquad (4.1).$$

Here, $[F^-]_{initial}$ indicates the initial fluoride concentration, V_t is the volume of the etching bath at the replenishment time t, M_{HF} is the molar mass of HF, a is the percentage of the replenishment solution, and ρ_{HF} is the density of the replenishment solution. As a simplification for the calculation $[F^-]$ may be regarded as $[HF]$.

The final HF concentration is checked again by titration before the first etching process with this electrolyte. The limit for replenishment is defined by the maximal volume of the reservoir, which is 30 liter. Figure 27 illustrates the development of the total fluoride concentration $[F^-]_{total}$ in a replenished electrolyte. If two data points correspond to an equal number of etched wafers, the lower one of them refers to $[F^-]_{total}$ before, and the other refers to $[F^-]_{total}$ after replenishment. The black diamond symbols represent the $[F^-]_{total}$ concentration and the white circles the ethanol concentration.

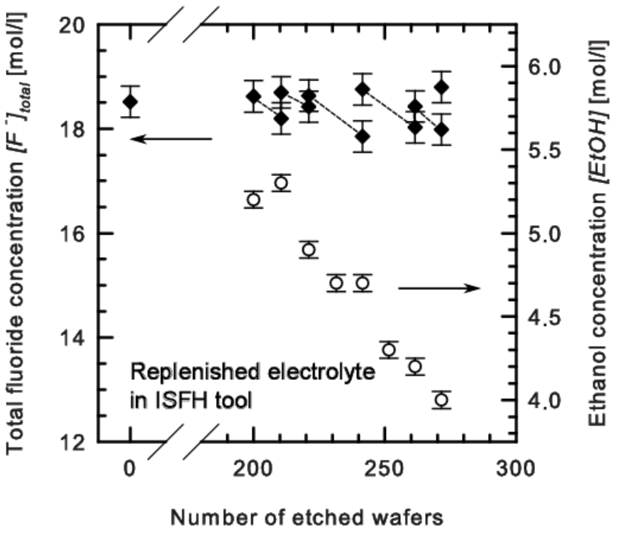

Figure 27: Development of the total fluoride concentration $[F^-]_{total}$ (black diamond symbols) and of the ethanol concentration *[EtOH]* (white circles) in a replenished electrolyte in the ISFH tool. The analysis was performed by titration with two measurements per data point; the lines are guides to the eyes only.

Consequences of the replenishment are on the one hand that the lifetime of the bath was extended from 236 etched wafers in Figure 25 to 272 wafers. On the other hand, the ethanol concentration of the electrolyte decreased caused by dilution with replenishment as is shown in Figure 27 by the white circles. Furthermore, evaporation contributes to the observed decrease as the data in Table 4.2 indicates. Hence, the ethanol concentration has to be considered as a further limiting factor for the definition of the electrolyte lifetime. Replenishing the bath with a mixture of HF and ethanol would diminish the decrease of the ethanol concentration. This was the method of choice for further etch processes.

Table 4.2: Enthalpies of evaporation [91,92] and vapor pressures [93] of the PSI electrolyte constituents.

	Enthalpy of evaporation [kJ/mol]	Vapor pressure at 25 °C [kPa]
HF	7.11	110
Ethanol	37.47	7.87
H_2O	40.64	3.17

It could be argued that replenishment with a more concentrated HF solution than the 50 wt% HF could diminish the water content in the electrolyte and, therefore, could decelerate the decrease of the ethanol concentration. A possible alternative is 70 wt% HF, which is available from industry manufacturers as a fuming chemical in a 200 liter barrel. However, the handling of 70 wt% HF requires even stricter safety instructions than of 50 wt% HF. Therefore, the enlarged personal hazard does not compensate the benefits of an extended bath lifetime for PSI etching.

Development of a new etching tool design

Altogether, the chemical analysis of the PSI etching electrolyte results in an improved understanding of the relationship between the HF concentration und the construction of the etching tool. The outcome of this is the construction of a new etching tool design by the project partner and an international company in cooperation with the ISFH. The prototype is currently located at the ISFH and is subject to further chemical analysis. It will be referred to as “SSE tool” in the following.

The SSE tool has several advantages in comparison to the ISFH tool. First, it was designed to satisfy industrial requirements and enables a high wafer delivery rate due to its increased electrolyte volume of 29.8 liter (taking the volume contraction into consideration). Second, the HF loss during the wafer exchange was rigorously diminished. The electrolyte is removed from the wafer by a gentle blow of nitrogen and collected for further etching before the chamber opens for wafer exchange. This particular development was a result of the chemical analysis of the ISFH tool. Furthermore, safety instructions allow the operation of the SSE tool without wearing a gas mask. The SSE tool is a closed construction that allows for the security relevant nature of the electrolyte with innovative technology: a blanket of nitrogen gas covers the electrolyte and restricts the evaporation of the chemicals as well as the latent danger of explosion. The importance of a closed construction was another aspect discovered by means of the chemical analysis performed in this work and is related to the decrease of the fluoride concentration as shown in Figure 25 and 26.

Chemical analysis of the PSI electrolyte in the SSE tool

The chemical analysis was applied to the SSE tool with its implementation at ISFH. Figure 28 gives an overview of the development of the etching bath constituents during the whole lifetime of the bath. In order to avoid confusion, more details concerning the individual constituents will be given in the following Figures 29 to 31.

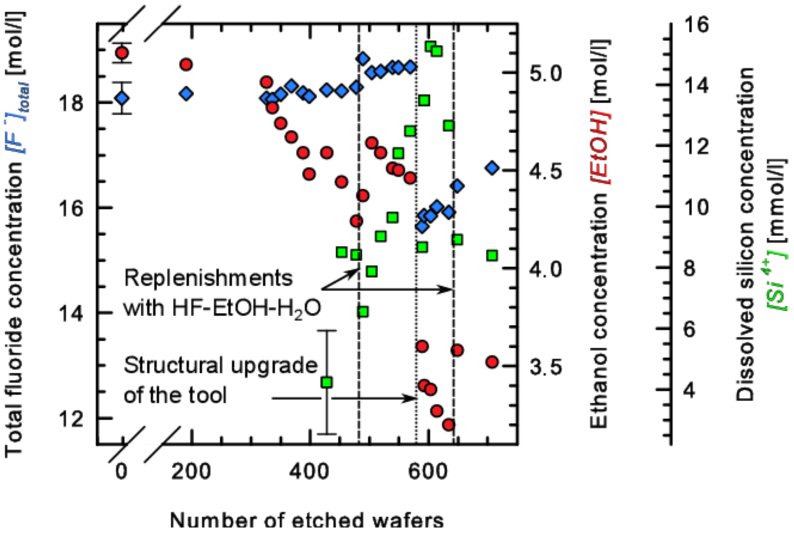

Figure 28: Development of the etching bath constituents for the SSE tool over the whole bath lifetime of 17 weeks. The fluoride concentration is indicated by blue diamonds, the ethanol concentration by red circles, and the Si concentration by green squares. An exemplary error (according to Appendix B) is given for each constituent. The lines demonstrate the replenishments with fresh HF-EtOH-H_2O electrolyte of the initial concentrations as well as the structural upgrade of the tool that had required a water rinse of the complete tool.

In Figure 28, the total number of 708 wafers was etched in the SSE tool within 17 weeks. The development of the electrolyte's constituents is depicted: the total fluoride concentration with blue diamonds, the ethanol concentration with red circles, and the concentration of the dissolved Si with green squares. Each of them is discussed in detail below. The electrolyte was replenished only two times, which is after 489 and after 649 porosified wafers. The replenishment solution contained HF and ethanol with their initial concentrations of 19.5 mol/l and 5.7 mol/l, respectively. Therefore, the concentrations of HF and ethanol rose after replenishment. This kind of replenishment is a result of the observed decrease of the ethanol concentration due to the former replenishment with HF (50 wt%) as illustrated in Figure 26; it should prevent the premature decrease of the wetting agent. The influence of the replenishment on the concentrations of the etching bath constituents is included in the individual discussions below. A structural upgrade of the tool was necessary during the observation period after 589 porosified wafers and required a thorough rinse of water. As a result, the concentrations in the electrolyte decreased due to the residual water in the hoses of the system. These events of replenishment and rinsing are marked in Figure 28 with dashed lines.

Figure 29 shows details concerning the development of the total fluoride concentration in the SSE tool, as given in Figure 28, before the structural upgrade became necessary after 589 wafers. As a consequence of etching with the SSE tool, less HF was consumed and it was possible to manage etching with just a single replenishment of the electrolyte in the investigated period. In this case, the replenishment became necessary because the filling level of the etching bath fell below the recommended value; details can be found in Table D4 in Appendix D on page 136. Thus, the replenishment was not due to a decrease in the HF concentration. There is no measurable consumption of HF within 489 porosified wafers; the deviations are within the uncertainty of the analytical measurement device, i.e., titration. The replenishment is indicated by the dashed line; the increased HF concentration remains until the structural upgrade was performed.

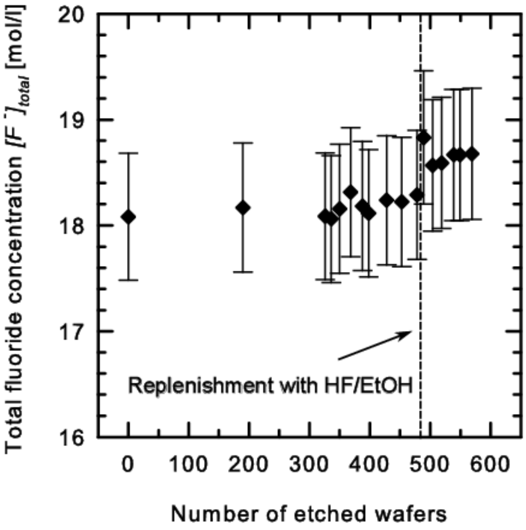

Figure 29: Details to the total fluoride concentration in the SSE tool as given in Figure 28 over a period of 17 weeks. The indicated replenishment was performed with an HF-EtOH-H_2O electrolyte of the initial concentrations used for the PSI process (19.5 mol/l for HF and 5.7 mol/l for ethanol).

Figure 30 shows the development of the ethanol concentrations in the ISFH tool as well as in the SSE tool – before the first replenishment – as a function of the number of etched wafers. The investigation period was about four weeks for both electrolytes. The loss of ethanol was decreased by about an order of magnitude from 18 mmol/l per etched wafer in the ISFH tool to 3 mmol/l in the SSE tool as indicated by the slopes of the regression lines.

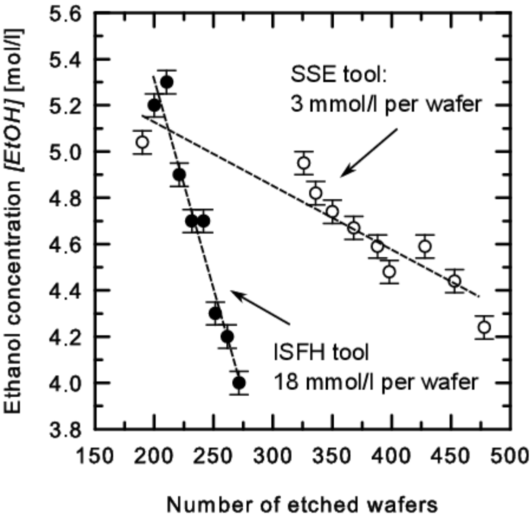

Figure 30: Comparison of the development of the ethanol concentration at the ISFH tool (black circles) and the SSE tool (white circles). The investigation period was four weeks for each electrolyte. The SSE data are taken from the overview in Figure 28, the ISFH data from Figure 27. The analysis was performed by the cuvette test method and the uncertainties determined according to Appendix B.

The origin of the ethanol loss could be evaporation (as discussed above), replenishment, or oxidation during the electrochemical process (chapter 2.2.3 on page 15). Evaporation could be a reason for the ethanol loss in the ISFH tool but should be neglected for the SSE tool due to the technical improvements of the closed etching tool. Several replenishments were performed to keep the HF concentration constant in the investigated electrolyte of the ISFH tool as indicated by Figure 27. However, at the SSE tool no replenishments were necessary during the observed period. Therefore, the decrease of the ethanol concentration should be regarded to the oxidation in the electrochemical environment to acetaldehyde, acetic acid, and then to CO_2 as illustrated Figure 31 and in equations (2.14) to (2.16).

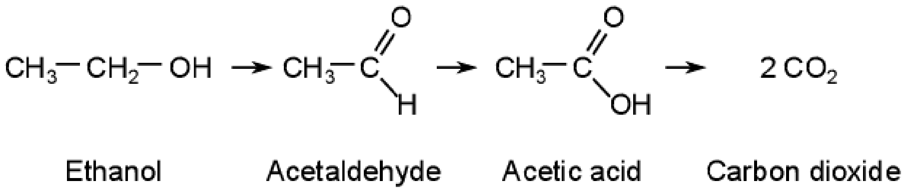

Figure 31: Oxidation of ethanol.

The ethanol concentration in the PSI etching bath is determined by the cuvette test method in this work. The cuvette test method is sensitive for all organic substances in the analyte, i.e., the result is the sum of the ethanol, acetaldehyde, and acetic acid concentration in the bath. In order to determine the amount of oxidized ethanol species in the bath, IC measurements were performed. However, no acetic acid was found due to the fact that the huge fluoride peak hides the acetate peak if this was present.

We suggest that evaporation of ethanol is the least probable explanation for the observed decrease in the SSE tool due to the technical improvements of the tool. If indeed the oxidation of ethanol takes place in reasonable amounts, it could progress to the formation of gaseous CO_2 which might leave the electrolyte as discussed in chapter 2.2.3 on page 17. The decrease of the ethanol concentration would then be due to the oxidation process during the electrochemical etching. We conclude that the decreasing ethanol concentrations illustrated in Figure 30 are probably due to evaporation, replenishment, and oxidation of ethanol with regard to the ISFH tool, whereas oxidation of ethanol might be the main cause for the decrease concerning the SSE tool. As a result of the implementation of the SSE tool and the received deceleration of the decrease of the ethanol concentration, a larger number of porosified wafers was processed within a single etching bath.

We observed qualitatively that a certain amount of ethanol in the electrolyte seems to be necessary for a homogeneous distribution of the widths of the bridges in the separation layer of mesoporous Si. If less than about 3.5 mol/l ethanol remained in the electrolyte, the detachability of the porous layers with the epitaxial grown Si on top was not sufficient. Pieces of the porous Si held on to the substrate wafer and the layer exhibited cracks and holes. Therefore, the influence of the ethanol concentration on the electrolyte's performance is further investigated in chapter 5.

As a conclusion of the analysis so far, we recommend the determination of the ethanol content in the electrolyte. The observed decrease of ethanol implicates the oxidation during the electrochemical process to acetic acid or even further to CO_2. Thus, for the PSI process as performed at ISFH, it is at least as important to determine the ethanol concentration as it is advisable to determine the HF concentration in order to obtain detachable porous layers.

Figure 32 shows the development of the dissolved Si concentration in the SSE tool from December 2011 to March 2012. The analysis was performed by ion-chromatography with post-column derivatization as was introduced in chapter 3.3 on page 33. Due to the very low SiF_6^{2-} concentrations in the first period of the electrolyte lifetime the experimental analysis starts at 428 etched wafers. Furthermore, the samples concentrations were raised with 0.18 mmol/l Si – prepared from an H_2SiF_6 solution – in order to meet the analysis method's requirements.

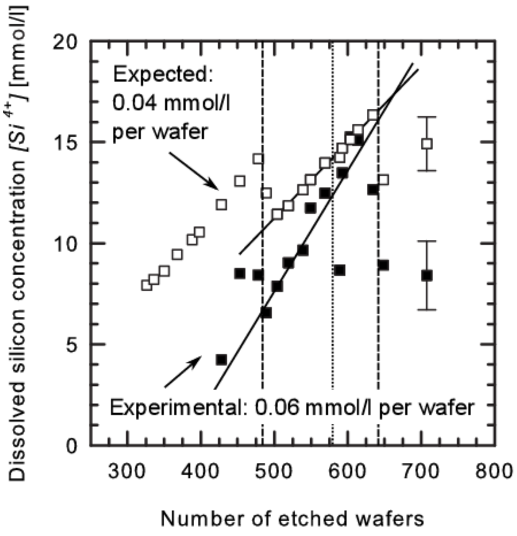

Figure 32: Development of the dissolved Si concentration of the PSI electrolyte in the SSE tool as determined by ion-chromatography with post-column derivatization. The expected concentration of dissolved Si is indicated by the white squares, the experimental concentration by the black squares. An exemplary error is given for each. The dotted and dashed lines are the same as in Figure 27 (see the detailed explanation there); the lines are related to a structural upgrade of the tool as well as to replenishments of the electrolyte.

For comparison, the theoretical concentration of Si $[Si]_{theo}$ is included in Figure 32 determined by

$$[\mathrm{Si}]_{\mathrm{theo}} = \frac{\Delta m_{\mathrm{Si}}}{M_{\mathrm{Si}}\, V_{\mathrm{Bath}}} \tag{4.2}$$

where M_{Si} is the molar mass of Si [g/mol], V_{Bath} is the volume of the etching bath [l], and Δm_{Si} is the estimated amount of dissolved Si per etch process. Gravimetric measurements of the wafer before and after the etch process give the theoretical amount of approximately 20 mg Si to be dissolved through formation of a porous double layer. The uncertainty of the theoretical amount of dissolved Si was determined taking into consideration the uncertainty of the bath volume as well as the above mentioned gravimetric analysis of the dissolved Si. The bath volume is roughly indicated by a filling level, which is, however, very error-afflicted: The replenishment of the bath with 7.5 liter corresponds to an indicated increase of the bath volume of about 4 liter. Therefore, the uncertainty of the bath volume is set to ±3.5 liter leading to the uncertainties of the estimated Si concentrations as illustrated in the graph in Figure 32.

The experimental determined development of the dissolved Si concentration demonstrates not a straight forward linear behavior. This is due to the fact that the SSE tool is a prototype and, therefore, some adjustment was necessary in the observed period. The tool was rinsed completely with water after 569 etched wafers, leading to a dilution of the electrolyte for the next process run according to an estimated volume of about 400 ml of water left in the hoses of the system. This structural upgrade of the tool is marked by the dotted line in Figure 32. Furthermore, the steps to a lower concentration at 489 and 649 etched wafers correspond to replenishments of the electrolyte resulting in a dilution. The replenishments are indicated by dashed lines in the graph and were performed with an HF-EtOH-H_2O electrolyte with the 19.5 mol/l HF and 5.7 mol/l ethanol. These events are the reason for the experimental outliers in the graph at 569, 649, and about 700 wafers. They were considered for the determination of the theoretical concentration of dissolved Si.

In Figure 32, the results of the expected and the experimentally determined amount of dissolved Si approach with an increasing number of etched wafers as indicated by the regression lines. The observed differences at the beginning of the experimental determination of the Si content are attributed to the difficulties with the very low Si content in the sample. This leads to the conclusion that the analysis data obtained with IC is more precise if the sample contains more than 10 mmol/l dissolved Si. However, the results obtained above this limit fit well to the expected development of the Si concentration. The amounts of dissolved Si per etched wafer were determined by means of the regression lines included in Figure 32. The theoretical amount is 0.04 mmol/l dissolved Si, whereas the experimental amount is 0.06 mmol/l. This means that the experimental and expected values agree reasonably. The mass of dissolved Si per etched wafer is not accessible due to the uncertainty of the bath volume as discussed above. Therefore, the result is given “per liter”.

The Si concentration after 708 etched wafers is about 8 mmol/l and, therefore, still very low. An influence of SiF_6^{2-} on the etched porous layers is not observable so far and is expected for far more etched wafers than processed recently with the SSE tool. However, chapter 6.3 discusses the possible effect of SiF_6^{2-} on the electrochemical equilibria of the etch process.

Determination of the free fluoride concentration

The knowledge of the amount of dissolved Si in the PSI electrolyte enables the determination of the free fluoride concentration $[F^-]_{free}$ according to

$$[F^-]_{free} = [F^-]_{total} - [F^-]_{bonded} \qquad (2.22).$$

The development of $[F^-]_{free}$ in the electrolyte of the SSE tool is shown in Figure 33. There is no significant difference between the total and the free fluoride concentrations within 700 etched wafers in the SSE tool. This means that the consumption of HF due to the reaction with Si is low compared to the amount of remaining HF in the electrolyte.

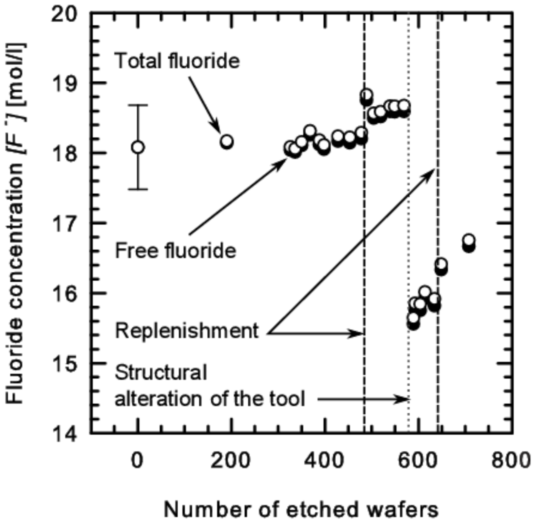

Figure 33: Development of the free fluoride concentration in the PSI electrolyte of the SSE tool. The white data points correspond to the total fluoride concentration $[F^-]_{total}$, whereas the black ones are correlated to the free fluoride concentrations $[F^-]_{free}$.

4.1.3 IMPACT ON THE ECONOMY OF THE PSI PROCESS

The HF consumption is one of many important issues for considering the PSI process for the fabrication of solar cells in terms of the economical rating. An industrial application is conceivable if the PSI process proves to be economic and, moreover, provides the possibility of cost reduction in comparison to conventional processes. The following paragraph deals with the SSE tool, which is – in comparison with the ISFH tool – relevant for an industrial application.

Table 4.3 compares the theoretical consumption of HF with the measured data of the SSE tool. The consumption of HF is calculated by means of the dissolved Si that is removed from the wafer during the etching process. The data was calculated assuming that no evaporation of the chemicals occurs. Therefore, considering equation (2.2), the gravimetrically determined weight difference of 20 mg Si per etched wafer, and the electrolyte volume of 29.8 liter, the theoretical consumption of HF results in 0.01 mol/l after etching of 100 wafers. Accordingly, the theoretical consumption of HF for a single wafer is 0.1 mmol/l, which is compensable by the addition of 0.15 ml HF (50 wt%) per etched wafer.

Table 4.3: Comparison of the HF consumption for the electrochemical etching of PSI layers in theory and in the SSE tool. It is assumed that 20 mg Si per wafer are dissolved. Since no HF consumption is observed within 569 etched wafers with the SSE tool, it is reasonable to suggest an agreement with the theoretical data.

	Dissolved Si [g]	Dissolved Si [mmol]	Consumed HF [mmol]	Consumed HF [mol/l]	Replenish-ment with HF (50 wt%) [ml]
Theoretical and SSE tool					
1 wafer etched	0.02	0.71	4.3	0.0001	0.15
100 wafers etched	2.00	71.21	427.3	0.0143	14.61
569 wafers etched	11.38	405.2	2 431.1	0.0816	83.14

The experimental HF consumption is determined by means of the SSE tool over a period of 17 weeks as was illustrated in Figures 28 and 29. During this period, 569 wafers were etched in the same electrolyte without replenishing the HF concentration. The maximum number of etched wafers in the same electrolyte has not been reached yet. Presumably, the ethanol concentration is a limiting factor for the usability of the electrolyte. This will be discussed in detail in chapter 5.

The adjustment of the etching parameters is closely related to the HF concentration in the electrolyte as discussed in chapter 2.3 on page 20. The experience at the ISFH shows that the first adjustments concerning the etching parameters is necessary if the HF concentration decreased for more than 1.0 mol/l in the electrolyte. To gain this decrease from etching only, about 7000 wafers need to be etched if evaporation is neglected.

As a result and in contrast to the ISFH tool, the HF concentration is not a particularly crucial issue for the economical rating of the PSI process if the SSE tool is used. Experimentally, no decrease in the HF concentration within 569 etched wafers was observed so far. A measurable decrease of the HF concentration, i.e., measureable with the fluoride determining analysis methods investigated in this work, is not expected before 2000 wafers are etched. A reliable statement concerning the quality and homogeneity of the etching process is possible through the detachability of the porous layers. The ethanol concentration might have a considerable impact on the homogeneity of the porous layers, however, which was not observed within the 569 wafers etched before the structural upgrade of the SSE tool. Therefore, a feasible prediction of the etching bath's lifetime and, thus, of the economy of the PSI process requires further long-term investigations.

The investigations demonstrate that the electrochemical etching of a porous Si double layer as required for the PSI process is theoretically possible without adjustment of the etching parameters for about 7000 wafers, as discussed above. Even then, the lifetime of the electrolyte can be enlarged by replenishment of the consumed fluoride. This is most effective if the ethanol concentration is replenished, too. Ethanol has to be taken into consideration as a further limiting factor for the bath lifetime. In the SSE tool, we found a loss of 3 mmol/l ethanol per etched wafer according to Figure 30. Considering the ethanol limit to be somewhere below 4 mol/l, we assume that about 600 wafers could be etched before a replenishment of the ethanol concentration is recommended.

4.2 MACPSI ETCHING BATH

This chapter discusses the application of the chemical analysis methods on the MacPSI etching bath for the formation of macroporous Si used as an absorber layer in an innovative concept for Si solar cells [61]. The electrolyte consists initially of 1.43 mol/l HF and 1.14 mol/l acetic acid.

The MacPSI etching tool at ISFH works with an implemented software (SiPor by ET&TE) that controls the replenishment of the HF concentration in the electrolyte through calculation of the valence as described in chapter 2.2.2 on page 13. Due to the etched surface area of 133 cm^2 and the layer thickness of 30 µm the dissolution of 0.5 g of Si is expected per etched wafer due to gravimetric measurements. The software replenishes the electrolyte automatically with 4.7 to 5 ml of 40 wt% HF towards the end of the etching process while the separation layer is etched. Since the tool and the reservoir of the electrolyte are closed, evaporation is neglected in the following.

This paragraph deals with analyses of the composition of the MacPSI electrolyte during the bath's lifetime. The experimental increase of the fluoride concentration is determined and compared to the theoretical expected values. Besides, the development of the wetting agent acetic acid is investigated to decide if the replenishment impacts the acetic acid concentration and, as a result, a replenishment of acetic acid is necessary. During the investigations within the scope of this work, the bath lifetime of the MacPSI tool was limited to about 30 to 40 wafers due to technical circumstances.

The determination of the fluoride concentration was performed with F-ISE. Titration was not suitable since the acetic acid in the sample prevents the adjustment of the pH with NaOH. Figure 34 depicts the development of the total fluoride concentration in the MacPSI etching bath within 30 etched wafers. The experimental and theoretical data are in excellent agreement. The total fluoride concentration increases due to the replenishment implemented in the software.

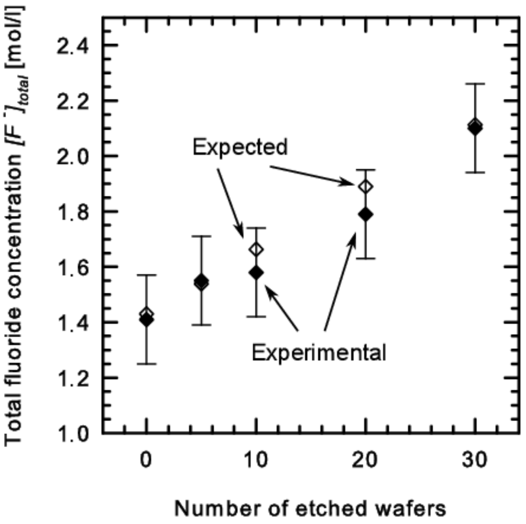

Figure 34: Development of the total fluoride concentration in the MacPSI etching bath within 30 etched wafers. Experimental data points are equipped with errors. The total fluoride concentration increases due to the replenishment of the consumed fluoride as implemented in the software.

The determination of the concentration of the reaction product SiF_6^{2-} in the MacPSI etching bath was performed with ion-chromatography and subsequent post-column derivatization. Figure 35 describes the increase of the dissolved Si concentration.

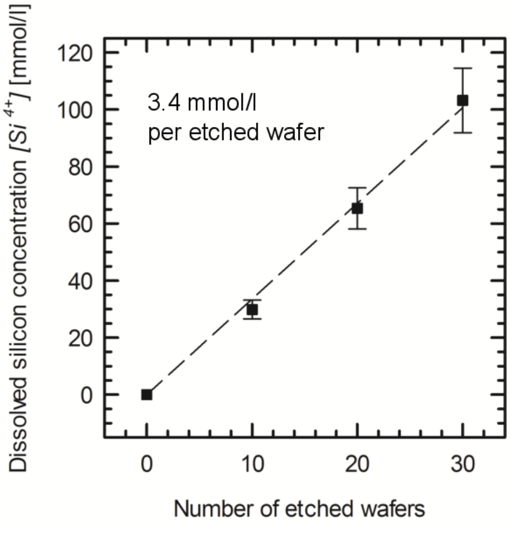

Figure 35: Concentration of dissolved Si in the MacPSI etching bath within 30 etched wafers.

The linear regression allows the calculation of the amount of dissolved Si per wafer, which is 3.4 mmol/l per wafer. Under the assumption that the initial volume is 4.585 l, the amount of dissolved Si is (440 ± 50) mg per porous double layer. This value corresponds well to the theoretical value of 0.5 g dissolved Si obtained by gravimetric analysis. The amount dissolved per etched wafer is directly related to the consumption of HF. Thus, the replenishment of the consumed fluoride with HF is important for the MacPSI process in order to enlarge the lifetime of the electrolyte.

As a result from the IC measurements, the concentration of the free fluoride is accessible according to

$$[F^-]_{free} = [F^-]_{total} - [F^-]_{bonded} \qquad (2.22).$$

Figure 36 illustrates the concentration of the free fluoride within 30 etched wafers. The replenishment keeps the theoretical concentration constant as indicated by the white diamonds. The experimental data are in agreement with the expected concentrations within the uncertainty of the measurement. This indicates that there is no evaporation of the electrolyte and, therefore, no noteworthy decrease of HF as has been supposed at the beginning of this paragraph.

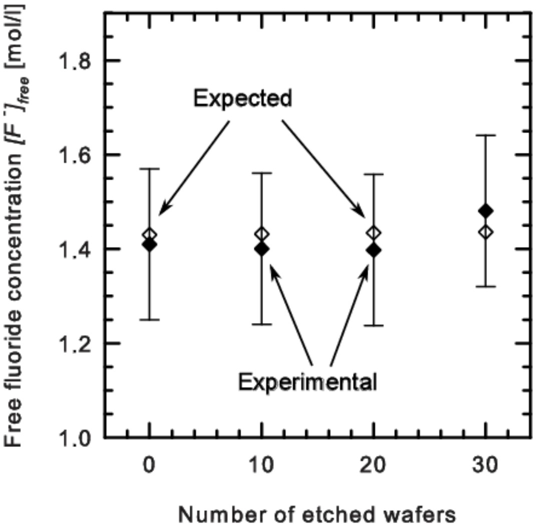

Figure 36: Comparison of the theoretical (white diamonds) and the experimentally determined free fluoride concentrations (black diamonds) in the MacPSI etching bath within 30 etched wafers. The concentrations are constant due to the periodic replenishment.

The concentration of the acetic acid was determined with the cuvette test method. The results are shown in Figure 37 for two etching baths A and B of the same initial concentration within the measurement's accuracy. For up to 30 etched wafers, the acetic acid concentration is constant within the method's uncertainty throughout the bath lifetime. A slight dependency of the acetic acid concentration on the increase of the bath volume – due to the replenishment of the free fluoride concentration – is theoretically expected, however, not observed so far. The absence of the decrease of the acetic acid concentration is further a hint that the electrochemical oxidation of acetic acid to carbon dioxide (chapter 2.2.3 on page 17) is not critical for the performance of the MacPSI etching bath within the investigated amount of 30 etched wafers. In addition, evaporation of acetic acid is not critical due to the vapor pressure of 2.07 kPa [93] (compare to Table 4.2 on page 48). Therefore, replenishment of the acetic acid concentration is not recommended.

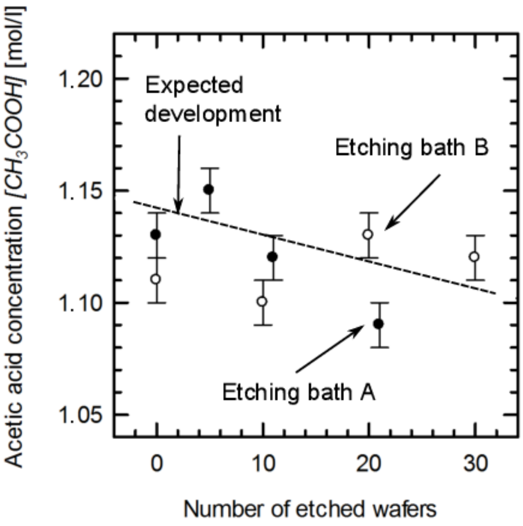

Figure 37: Development of the acetic acid concentration in two MacPSI etching baths A (black circles) and B (white circles) of the same initial concentrations. The volume of the bath increases during the bath lifetime due to the replenishment of the HF concentration. Therefore, the expected concentration decreases with the increasing number of wafers as indicated by the dashed line.

4.3 CONCLUSIONS

Investigation of the PSI etching bath

This chapter demonstrated the utility of the chemical analysis on the PSI etching bath. The HF analysis in the ISFH etching tool uncovered an enormous HF consumption of more than 60-times as much as expected. Furthermore, sources of HF loss were discovered and fixed if possible. The chemical analysis offered the possibility to replenish the electrolyte and to further increase the lifetime of the bath from about 250 to up to more than 700 porosified wafers. The first replenishments demonstrated that the ethanol content in the bath decreases fast and that the formation of completely detachable porous layers seems to depend on the remaining ethanol content. Consequently, it was necessary to even investigate the development of the ethanol concentration during the bath's lifetime.

The results obtained with the ISFH tool improved the development of another tool design, which is the SSE tool. Here, we were able to demonstrate the economic potential of the PSI process since the high consumption of HF was no more observable. It seems as if the high loss of HF resulted mostly from the previous tool design. The HF consumption of the SSE tool corresponds to the theoretical values and requires the – theoretical – addition of 14.61 ml HF (50 wt%) after 100 etched wafers. A measurable decrease of HF is not expected before 2000 wafers are etched. Besides, the number of etched wafers increased by about a factor of 3 compared with the ISFH tool. This is not a limit so far, but was attributed to technical circumstances.

The observed decrease of the ethanol concentration in the SSE tool is probably attributed to the oxidation of the ethanol during the etching process. This actually means that ethanol is consumed and the development of its concentration desires continuous analysis. The laboratory experience qualitatively shows that if the ethanol concentration is too low, the porous layers are not detachable without cracks. In the SSE tool we found a decrease of 3 mmol/l ethanol per etched wafer, which limits the usability of the electrolyte to about 600 wafers taking into consideration the investigated ethanol range from 4.0 to 5.7 mol/l. This means that a replenishment of the etching electrolyte is strongly recommended concerning the ethanol concentration. Furthermore, the replenishment of ethanol is more relevant than the replenishment with HF if the evaporation of the chemicals can be neglected and the reaction with Si is the only reason for the HF consumption.

The determination of the dissolved Si concentration demonstrated to be more accurate compared to the theoretical values if the sample contains more than 10 mmol/l dissolved Si. We found an experimental increase of 0.06 mmol/l dissolved Si per etched wafer. This increase is very low and an interference of the reaction product SiF_6^{2-} to the quality of the etched wafers was not observable so far.

With the analysis methods, the amount of free fluoride in the etching bath was accessible. We found that the consumption of HF due to the reaction with Si is low in the investigated concentration range compared with the amount of remaining HF in the electrolyte.

Investigation of the MacPSI etching bath

The development of the constituents in the MacPSI electrolyte was also investigated in this chapter. The F-ISE method was found suitable for the analysis of the MacPSI etching bath. Titration could not be used since the acetic acid in the electrolyte prevented the required adjustment of the pH. The experimental data fit well to the theoretically expected data; the automatic replenishment of the electrolyte implemented by the etching software could be reconstructed.

The cuvette test method IC, although not specially aligned for it, is suitable for the macroporous etching bath, too. The concentration of acetic acid was constant throughout the investigated range of 30 etched wafers. Both, the replenishment of the HF concentration and the probable oxidation of acetic acid to gaseous carbon dioxide during the electrochemical etching process were not found to influence the acetic acid concentration. The experimental amount of dissolved Si was determined to (440 ± 50) mg per etched wafer. Therefore, the theoretical amount of 0.5 g dissolved Si per wafer could be verified by the IC measurements.

General aspects for etching tools

The results of this chapter are related in particular to the etching tools used at the ISFH. However, some issues will be relevant for etching tools in general.

The dependency of the etching parameters on the HF concentration was discussed in chapter 2. This work demonstrates the importance of a closed etching setup in comparison with an open setup, where the loss of HF due to evaporation has to be considered. It could be shown that the use of a closed etching setup is beneficial since the main cause for the HF consumption then is the reaction with Si.

In addition to the HF concentration in the electrolyte, a further limiting factor could be identified considering the lifetime of an electrochemical etching bath: the wetting agent. If ethanol is used as a wetting agent, the oxidation during the electrochemical procedure may lead to a considerable decrease of the ethanol concentration. This is especially important if high voltages are applied for the etching process, as the investigations of the PSI process demonstrated. However, if relatively low voltages are used the oxidation of the wetting agent is not significant as the investigation of the MacPSI process showed. Here, we found no significant decrease of the acetic acid concentration in the investigated period. In general, the determination of the ethanol concentration is as much recommended as is the observation of the HF concentration.

The dissolved Si concentration is an indicator for the amount of free fluoride in the electrolyte. In this work, the SiF_6^{2-} concentration was found to increases slowly during the bath lifetime without an impact on the etching procedure investigated so far. This is further discussed in chapter 6.

5 WETTING BEHAVIOR OF THE PSI ELECTROLYTE

In this chapter, the role of ethanol in the PSI electrolyte is investigated in detail. Before the research work performed in this thesis, the etching of mesopores in the PSI process has been performed in aqueous HF solutions without a wetting agent. We will experimentally determine and discuss two main questions here: Why is it beneficial that the electrolyte contains ethanol? And considering the PSI electrolyte used at ISFH: How much ethanol is required for homogeneous formation of bridges in the separation layer?

The first part of this chapter concerns the experimental determination of the etching electrolytes properties, i.e., the density, the viscosity, the contact angle, the surface tension, and the ability to permeate through a porous membrane. Some of these parameters are directly accessible for the electrolyte, others are determined for aqueous ethanol if the use of HF is prohibited due to safety reasons. We compare the experimental data to literature data for aqueous HF where possible in order to determine the influence of the ethanol.

The second question is approached by a discussion concerning the size and the distribution of hydrogen bubbles related to the ethanol concentration in the electrolyte. The discussion includes the solubility of hydrogen as well as the diffusion of HF_2^- in the electrolyte.

The experimental data to the figures are listed in the tables in Appendix E.

5.1 INVESTIGATION OF THE PSI ELECTROLYTE'S PROPERTIES

This chapter deals with the wetting properties of the PSI electrolyte. Investigated properties are the density, the surface tension, the contact angle, the viscosity, and the ability to permeate through porous Si. The investigation of these parameters is important for further discussions concerning the role of ethanol in the PSI electrolyte.

The investigated solutions are similar to the PSI electrolyte, i.e., they consist of HF, ethanol, and water. The HF concentrations are kept constant at 19.5 mol/l, while the ethanol concentration ranges from 0 to 5.7 mol/l in order to illustrate the aging of the electrolyte. Aging of the electrolyte means that the ethanol concentration decreases due to evaporation, oxidation during etching or replenishment.

5.1.1 DENSITY

The density of EtOH-H_2O solutions depends on the concentration of the ethanol and is reported in the literature [94]. This paragraph deals with the development of the density in the PSI electrolyte with decreasing ethanol concentration.

The former manufacturer of the electrolyte used in the PSI process at ISFH reported a density of 1050 g/l. Here, we determine the density of the HF-EtOH-H_2O solutions with decreasing ethanol concentration in order to simulate the aging of the electrolyte. These experiments were performed by gravimetric analysis. The ethanol concentration ranges from 0 to 5.7 mol/l. For each investigated HF-EtOH-H_2O solution five samples were taken with the volume of 0.5 ml, 0.75 ml, 1.0 ml, 1.25 ml, and 1.5 ml, respectively. The solutions were weighed by means of an analytical balance (Mettler AE 200, Mettler Toledo, Gießen, Germany). Each measurement was repeated five times, the data can be found in Appendix E. The densities were calculated by linear regression from the weight as a function of the volume; Figure 38 shows an exemplary measurement.

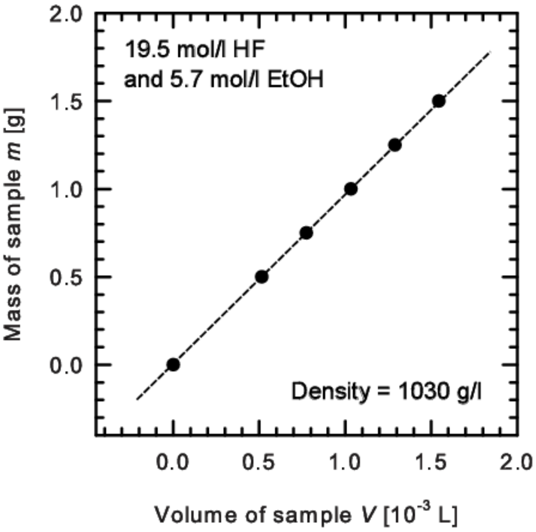

Figure 38: Determination of the density of HF-EtOH-H_2O solutions with the linear regression method. The uncertainties are small compared to the scale of the y-axis; they are explained in detail in Appendix B.

The uncertainties of the experimentally determined densities were calculated by error propagation taking both, the error of the pipette and the error of the balance into consideration as described in detail in Appendix B.

Figure 39 illustrates the resulting densities for the investigated HF-EtOH-H_2O solutions.

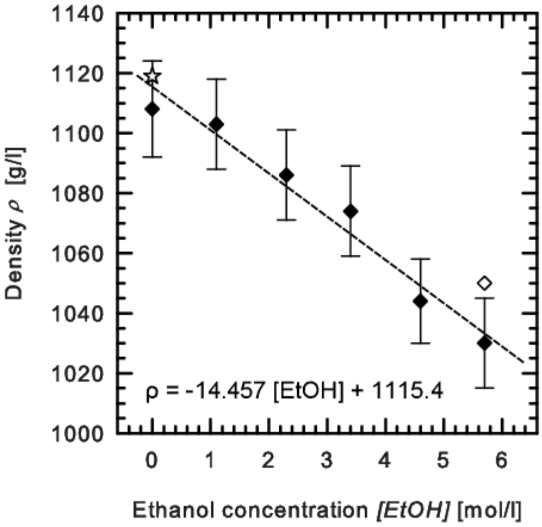

Figure 39: Experimentally determined densities of HF-EtOH-H_2O solutions (black diamonds). The white diamond indicates the density as reported by the former manufacturer; the white star indicates the literature value for aqueous HF with a concentration of 19.5 mol/l.

The results show that the density of HF-EtOH-H_2O solution decreases with increasing ethanol concentration. The experimentally determined density for 5.7 mol/l EtOH in 19.5 mol/l HF is close to the reported value of 1050 g/l as indicated in Figure 39. Therefore, the accuracy of the experimental values is taken as sufficient for further calculations. The reported density for 19.5 mol/l aqueous HF is 1119 g/l [95]; it is indicated by the white star in Figure 39 and within the uncertainty of the experiment.

The knowledge of the density of HF-EtOH-H_2O solutions allows for the calculation of the density of any HF solution with the ethanol concentration of less than 5.7 mol/l according to the linear regression illustrated in Figure 39.

5.1.2 SURFACE TENSION

The surface tension is the energy that is required to increase the surface of a liquid. It is counteracts the inner attractive forces that keep the surface as small as possible [96]. The surface tension determines the wettability of a liquid: The lower the surface tension is the better is its wettability. As an example, the surface tension of pure water is 72.75 mN/m and of pure ethanol 22.31 mN/m.

In this work, the surface tension σ is experimentally determined according to

$$\sigma = \frac{\rho \cdot g \cdot \Delta h \cdot r}{2 \cos\theta} \qquad (5.1).$$

Here, ρ is the density [kg m^{-3}], g is the standard gravity [9.81 m s^{-2}], Δh is the height of the liquid in a capillary tube [m], r is the radius of the capillary tube [m], and θ is the contact angle between the liquid and the surface [°].

Equation (5.1) includes unknown parameters for HF-EtOH-H_2O mixtures, which are the density ρ, the height in the capillary tube Δh, and the contact angle θ. The density was determined above. The contact angle for water and ethanol in contact with glass is $\theta = 0°$ [97] for complete wetting, which is indicated by a meniscus having the shape of a half-sphere at the maximum height in the capillary. Therefore, the contact angle is neglected in the following determination of the surface tension due to $\cos\theta = 1$. Consequently, the experimental determination of the capillary height is described in the following paragraph before we continue with the determination of the surface tension.

Determination of the capillary height

The determination of the rising height of the electrolyte solution in a capillary tube was performed with glass capillary tubes with an inner diameter of 0.8 mm (melting point determination tubes, Hirschmann Laborgeräte GmbH & Co. KG, Eberstadt, Germany). The investigated electrolyte solutions are HF-EtOH-H_2O solutions with the ethanol concentration ranging from 0 to 5.7 mol/l and a constant HF concentration of 19.5 mol/l.

For the investigation of the capillary height a capillary tube was dipped into 10 ml of the electrolyte solution. The solution rose until equilibrium was reached after a few seconds. Subsequently, the height of the liquid in the capillary tube h_{total} was marked with a pen. The height required for the determination of the surface tension Δh according to equation (5.1) was calculated by

$$\Delta h = h_{total} - h_{surface} \tag{5.2}$$

with $h_{surface}$ being the height of the 10 ml electrolyte solution in the vessel. The experiment was repeated tenfold for each solution in order to determine the measurement uncertainty. Figure 40 shows the schematic representation of the experiment on the left and on the right the experimentally determined capillary heights Δh for HF-EtOH-H_2O solutions in glass capillary tubes.

The experimental uncertainty is the standard deviation within the tenfold measurement of each investigated solution plus the uncertainty of the height reading estimated to 1 mm. The capillary heights obtained with glass tubes in Figure 40 illustrate a decrease with increasing ethanol concentration.

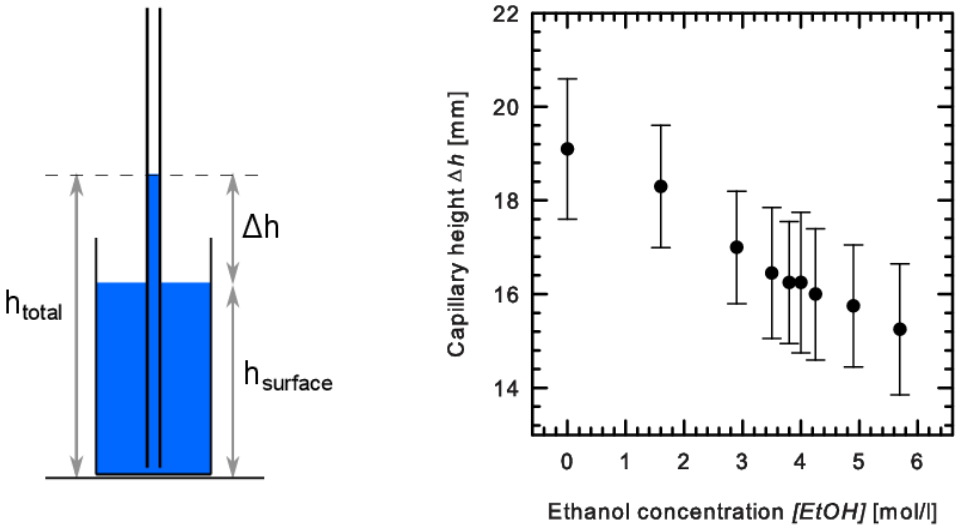

Figure 40: Schematic representation of the experimental setup (on the left side) and experimentally determined capillary height for and HF-EtOH-H_2O solutions in glass capillary tubes (on the right side). Each data point is the mean of 10 measurements.

Determination of the surface tension

The experimentally determined density and the capillary height from the glass tubes allow the calculation of the surface tension according to equation (5.1). Figure 41 compares the experimentally determined surface tensions of HF-EtOH-H_2O with the reported surface tension of 47.3 mN/m for aqueous 19.5 mol/l HF as calculated from the reported data in [98]. The comparison shows that the experimental results underestimate the reported result. Thus, the absolute values for the surface tension are expected to above the experimental results.

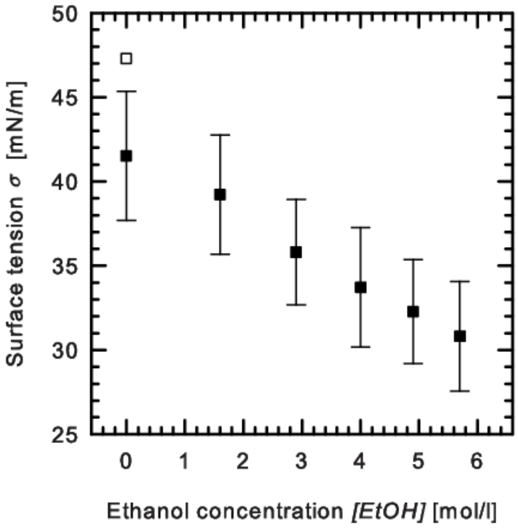

Figure 41: Comparison of the experimentally determined surface tensions of HF-EtOH-H_2O (in black squares) with the reported data for aqueous HF (the white square) calculated according to [98].

The uncertainties of the experimentally determined surface tensions were calculated by error propagation taking into consideration the standard deviation of the capillary height, the error of the experimentally determined density, and the radius of the capillary tube. Details concerning the determination of the error of the surface tension can be found Appendix B.

The addition of ethanol to aqueous HF decreases the surface tension of the PSI electrolyte compared to the surface tension obtained for aqueous HF solutions of 47.3 mN/m. Besides, this indicates that even HF is kind of a wetting agent in comparison to water with a surface tension of 72.75 mN/m. We find a linear dependency indicating that the more ethanol is in the electrolyte the lower the surface tension will be. The surface tension of pure ethanol is reported as 21.8 mN/m [99]; therefore, the surface tension of the PSI electrolyte is not expected to be below this limit even if the ethanol concentration is further raised.

5.1.3 CONTACT ANGLE

The wettability of a liquid is determined by the contact angle between the surface and the liquid. Figure 42 shows photographs of aqueous ethanol drops in the concentration range from 0 to 5.7 mol/l indicating the change of the wettability of the solution. The drops sit on a Si wafer substrate.

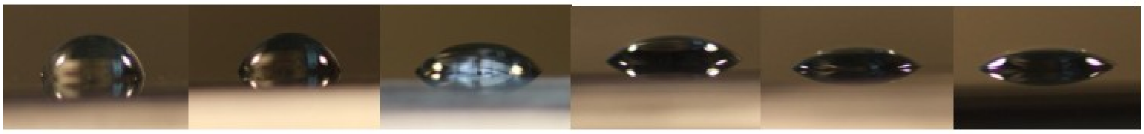

Figure 42: Photographs taken from drops of aqueous ethanol sitting on a Si wafer substrate. The concentration of ethanol ranges from 0 to 5.7 mol/l from left to right.

The addition of ethanol decreases the surface tension of the water and increases the wetted surface area as shown in Figure 42. In order to investigate the contact angle in more detail, measurements were performed with a contact angle measuring device equipped with a camera using the sessile drop method. The evaluation software was CAM 100 Optical Contact Angle Meter, version 1.0 (KSV Instruments Ltd). The substrate was a porosified *p*-type Si wafer. For the creation of the drops, a gastight syringe from Hamilton-Bonaduz was used with a total volume of 1 000 µl; the volume of each drop in the measurements was 13 µl. Due to safety reasons, contact angle experiments were operated with aqueous ethanol solutions only.

Figure 43 indicates the development of the contact angle on a Si *p*-type wafer porosified within the PSI process. The contact angle decrease from around 80° to about 30° within the investigated ethanol concentration range. The measurements were repeated five times with the standard deviation as the uncertainty.

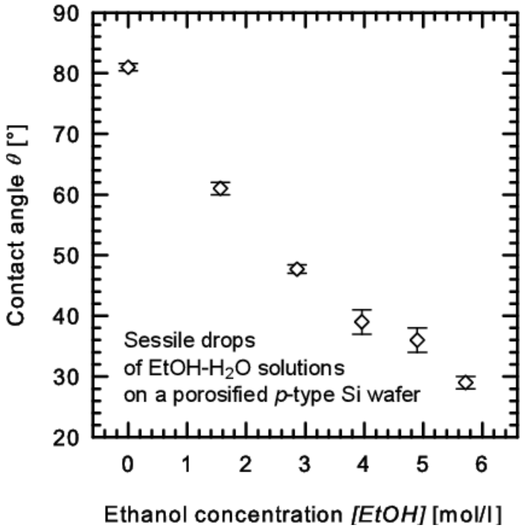

Figure 43: Experimentally measured contact angles with the sessile drop method for aqueous ethanol solutions. Each data point represents five measurements.

As expected, the more ethanol is in the solution, the lower is the determined contact angle. We assume that this behavior is in general the same for contact angles of HF-EtOH-H_2O solutions.

5.1.4 DYNAMIC VISCOSITY

This paragraph investigates the viscosities of HF-EtOH-H_2O solutions with the ethanol concentration ranging from 0 to 5.7 mol/l and a constant HF concentration of 19.5 mol/l. The experiments are performed with a falling sphere viscometer where a sphere of a known density and diameter is dropped into a cylindrical flask containing the solution to be investigated. This experiment is based on Stokes' law for a sphere falling through a surrounding fluid.

$$F_d = -6\pi\eta r \nu \qquad (5.3)$$

Here, F_d is the drag force, η is the dynamic viscosity, r is the radius of the sphere, and v is the velocity. The sphere will experience a balance of the viscous drag force and the buoyancy force F_b through the gravitational force F_g as illustrated in Figure 44. At steady state, the terminal velocity v of the sphere is determinable by

$$\nu = \frac{2r^2 g(\rho_S - \rho_F)}{9\eta} \qquad (5.4)$$

where g is the gravitation constant, ρ_S is the density of the solid sphere, ρ_F is the density of the fluid [100]. In the following experiment, the velocity v is determined with a sphere falling in a cylindrical flask.

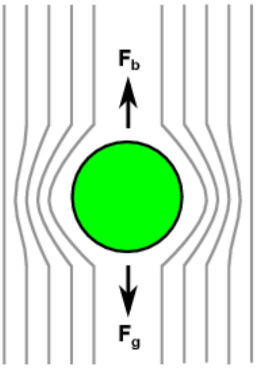

Figure 44: Creeping flow past a falling sphere.

The spheres used in this experiment are made of polyamide with a diameter of 2.0 mm and a density of 1.13 g/cm^3 (from KGM Kugelfabrik GmbH, Fulda, Germany) in order to meet the requirements for HF persistency. It is of importance that the density of the sphere is greater than the density of the solutions in order to have the sphere falling instead of swimming on the surface. The spheres were colored with a customary, black marker to increase the visibility during the experiment. The cylindrical flask is made from polyethylene and has an inner diameter of 5.5 cm. The distance from the falling sphere to the wall is about 14 times the sphere diameter, thus, we can neglect the influence of the wall for spheres falling in the centre of the flask and assume laminar flow. The falling distance is 24 cm consisting of 7 cm as the settling distance for the sphere to reach the equilibrium velocity and 17 cm as the falling distance. A stopwatch measures the time the sphere requires to pass the falling distance. Figure 45 illustrates the experimental setup with a falling sphere marked with an arrow. The falling times are listed in Appendix E.

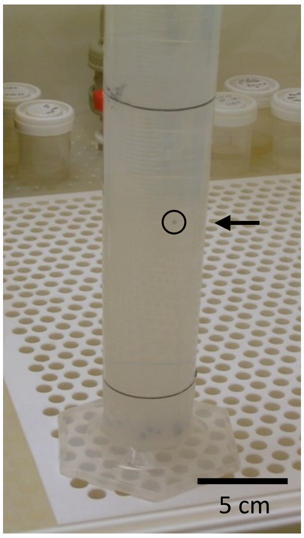

Figure 45: Experimental setup for the falling sphere test. The sphere is indicated by the arrow and the circle.

The dynamic viscosity is calculated according to equation (5.4); the results are illustrated in Figure 46. The determination of the uncertainty is attached to Appendix B; the uncertainty of the experimentally determined densities of the electrolyte exhibits a strong influence on the result. The viscosities of HF-EtOH-H_2O are extrapolated for ethanol concentrations below 3.5 mol/l. The experimental approach was not usable in this concentration range since the density of the electrolyte prevented the immersion of the sphere. This is in contrast to the experimentally determined densities of the electrolyte described above and indicates that the surface tension is high enough for the spheres to swim.

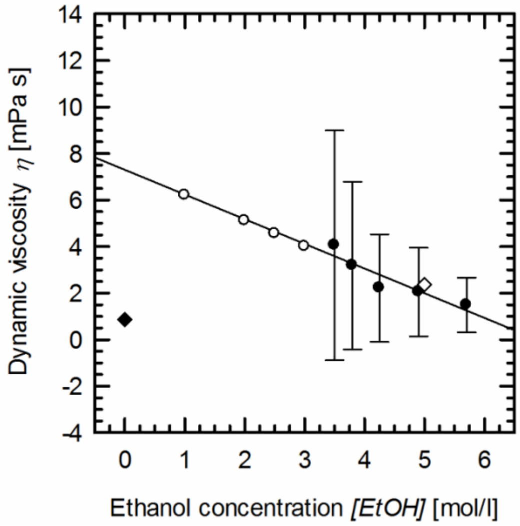

Figure 46: Experimentally determined viscosities of HF-EtOH-H_2O solutions (black circles). The data points in white circles were extrapolated for ethanol concentrations below 3.5 mol/l. the HF concentration is 19.5 mol/l for each investigated solution. The black diamond represents the literature value for aqueous HF (19.5 mol/l) [101], the white diamond the literature value for aqueous ethanol (5.0 mol/l) [93]. The uncertainties are calculated according to Appendix B.

Figure 46 shows that the viscosities of HF-EtOH-H_2O solutions depend strongly on the ethanol concentration. It should be noted that the spheres reacted with the HF in the investigated solutions. This was indicated by a vanishing color of the spheres during the falling and could have resulted in a roughening of the surface of the spheres and a slight adulteration of the result. Furthermore, about five of the spheres did not fall in the centre of the cylindric flask. Those spheres might not experience laminar flow, however, the falling times were found to be similar to the laminar flown spheres. Thus, the results of those spheres were not excluded; the 20-fold measurement of solution should diminish the influences of the non-laminar flow on the result.

The literature value for the viscosity of an aqueous ethanoic solution with a concentration of about 5.0 mol/l (i.e. 24wt%) is 2.37 mPa·s [93]. This is well represented by the experimental data in Figure 46. However, the viscosity of aqueous HF is about 0.86 mPa·s for a concentration of 19.5 mol/l (i.e. 38wt%) [101], which is clearly not represented by the experiment and due to the uncertainty of the measurement. According to the experiment, the viscosities of aqueous HF solutions with ethanol are expected to be higher than the literature value for pure HF. The deviation is mainly due to the uncertainty of the density of the electrolyte or even to the simple experimental setup. However, even if the absolute experimental values are error-afflicted, the tendency for lower viscosities with increasing ethanol concentrations is detectable. This is due to the observed increasing falling times of the sphere with decreasing ethanol concentration as indicated by Table E6 in Appendix E on page 144.

5.1.5 PERMEATION THROUGH POROUS SILICON

The following paragraph investigates the behavior of the electrolyte in contact with porous Si through experiments concerning the permeation. This experiment is close to the etch process and will provide insight concerning the required ethanol concentration for homogeneous etching. Since the required ethanol concentration is expected to be near to the initial ethanol concentration, we curtail the investigated range to 2.0 to 5.7 mol/l in the following.

It is a precondition for the etch process that the electrolyte could reach the etch front. Therefore, it is necessary that the electrolyte is able to permeate through the porous Si that forms during the etch process. The following paragraph describes the investigation of the permeability of the PSI layers with test items as shown in Figure 47.

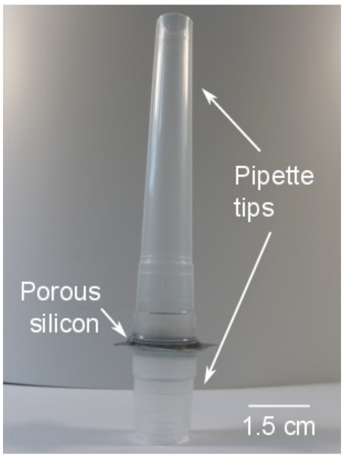

Figure 47: Test item for the investigation of the permeability of porous Si layers.

The test items consist of a porous Si layer glued between two pipette tips. The porous Si layer has a thickness of 36 µm and a porosity of about 20%, which corresponds to the starting layer conditions used in the PSI process. The pipette tips serve as reservoirs for the electrolyte compositions under investigation. The upper tip has the capability to hold the volume of 6 ml electrolyte. The glue is a pourable, addition-curing silicone rubber from Wacker (ELASTOSIL® RT 601, Wacker Chemie AG, München, Germany), which was investigated in terms of practicability for photovoltaics by Steckenreiter [5]. The curing time was 24 hours at room temperature before use. The resistance of the silicone against HF was checked successfully with 19.5 mol/l HF. After testing, all items dried at room temperature overnight before further measurements were carried out.

Figure 48 illustrates the experimental setup. The time-dependent investigation of the permeation of electrolytes with different compositions through the PSI layer was enabled by means of a mirror. The electrolyte compositions contain ethanol in concentrations ranging from 2.0 to 5.7 mol/l and 19.5 mol/l HF. This range was chosen for investigation in order to image a representative decrease of the ethanol concentration caused by replenishment and oxidation in the PSI etching bath starting at the initial concentration.

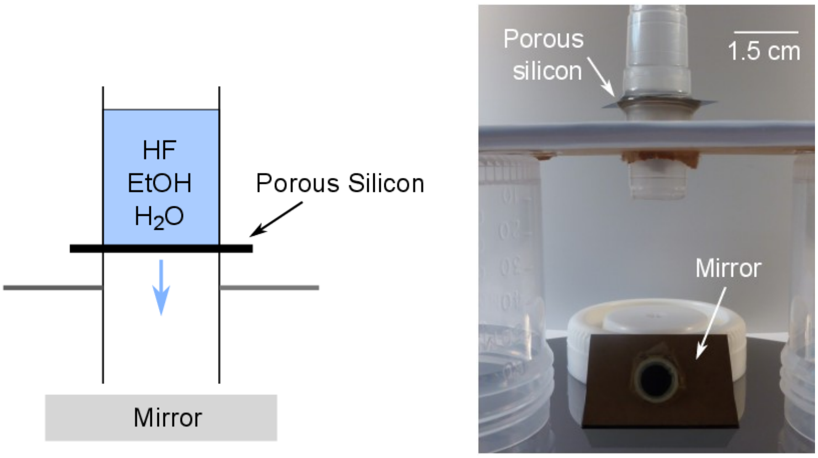

Figure 48: Schematic representation and photograph of the experimental setup for the investigation of the electrolytic permeation.

The development of the permeation capability of the electrolyte through the porous Si was followed with a digital reflex camera EOS 50D by Canon equipped with a macro objective lens with a focal distance of 24 to 105 mm. The photographs in Figure 49 illustrate the six different levels of electrolyte permeation through porous Si from bottom view, defined in this work.

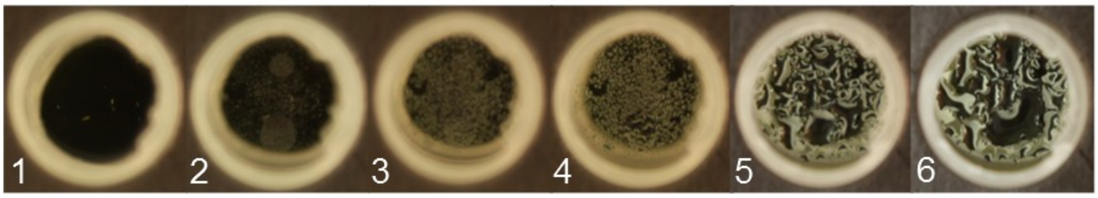

Figure 49: Permeation experiment with EtOH-H_2O and HF-EtOH-H_2O electrolytes with different ethanol concentrations. Demonstrated is the appearance of drops on the bottom side of porous Si with time indicated by level (1) to (6). The photographs were taken with a digital reflex camera equipped with a macro objective lens.

The first picture in Figure 49 corresponds to level (1) and shows the appearance of the porous Si without any electrolyte; the observable spots are traces of dust. The first traces of the electrolyte are observable in the second level (2), where the electrolyte forms very small drops. In the permeation level (3), the small drops are distributed homogeneously over the whole area of the porous Si. Subsequently, the drops grow further and start to merge on a small scale in level (4). In the following level (5) the growing drops merge clearly. As a result, the number of drops decreases. The final level (6) indicates the appearance of very large drops covering the whole surface of the porous Si. Throughout all permeation experiments, no dropping of electrolytic solutions was observable.

Figure 50 shows the time-dependent appearance of level (1)-(6) for the HF-EtOH-H_2O solutions with ethanol concentrations from 2 to 5.7 mol/l.

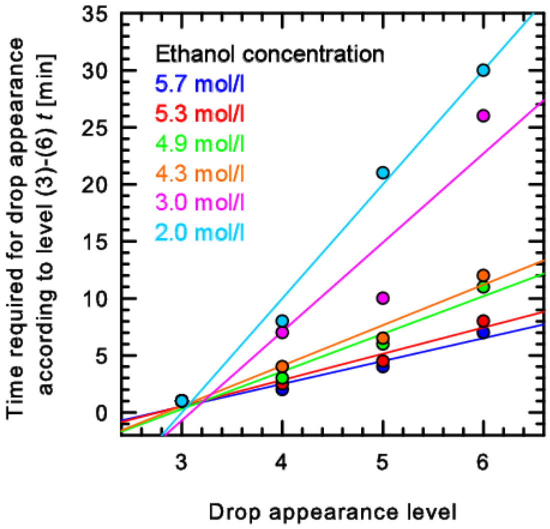

Figure 50: Required time for HF-EtOH-H_2O electrolytes to reach the appearance of the drops according to Figure 49. All electrolyte compositions start with level (3).

Demonstrated is the required time for the porous layers to exhibit the levels (1) to (6) according to Figure 49 as a function of the ethanol concentration in the electrolyte. The HF-EtOH-H_2O solutions start all with level (3) independent on the ethanol concentration. This is a hint for the quick permeation of these solutions through the porous Si that is independent on the investigated ethanol concentration. The composition of the electrolyte determines the required time for the appearance of the level (4) to (6). This is where the drop formation occurs on the bottom side of the porous layers. The more ethanol the electrolyte contains, the faster the levels change. The fastest permeation behavior shows the solution containing 5.7 mol/l ethanol that reaches level (6) within 7 min. The electrolyte with 2.0 mol/l requires 30 min for level (6). All electrolyte solutions HF-EtOH-H_2O are able to reach level (6). The solutions containing between 5.7 and 4.3 mol/l ethanol show a similar slope of their regression lines, whereas the solutions containing 3.0 and 2.0 mol/l have a much steeper slope. Thus, the permeation behavior seems to have a kind of critical value here depending on the ethanol concentration. However, it should be taken into consideration that the slope of the regression line for 3.0 mol/l ethanol could be similar to the higher concentrated ethanol samples if the last data point was lower. The limit of 4.3 mol/l may therefore indeed be shifted to lower ethanol concentrations.

The performance of this experiment with aqueous HF (19.5 mol/l) showed no permeation of liquid at all. This means, that there is a significant difference in the permeation behavior of electrolyte solutions containing ethanol and those with only HF. The ethanol is essential for the ability of the electrolyte to permeate the porous Si.

5.2 DISCUSSION OF THE ROLE OF ETHANOL IN THE PSI ELECTROLYTE

In the PSI etching bath ethanol is part of the electrolyte as a wetting agent in order to facilitate the formation of homogeneously etched porous layers. The addition of ethanol reduces the surface tension as demonstrated above. This should improve the detachability of the hydrogen gas bubbles that from during the etch process [69].

Hydrogen bubbles are a source of inhomogeneous etching because they prevent the diffusion of fresh electrolyte to the etch front which might be a cause for the formation of thick bridges. This is the reason, why ethanol is considered as a parameter that could potentially limit the usability of the electrolyte. This chapter deals with the experimental results obtained so far concerning the electrolytes wetting properties, i.e., surface tension, contact angle, and viscosity. The importance of ethanol in the PSI electrolyte is discussed in relation to the formation of hydrogen bubbles.

The size of hydrogen bubbles

The experimental results described above demonstrate that the surface tension of the electrolyte depends on the ethanol concentration in the electrolyte. Compared to aqueous HF, the addition of ethanol decreases the surface tension by about 15 mN/m. The reduced surface tension should facilitate the release of hydrogen bubbles. If hydrogen bubbles stick to the surface, they hinder the access of the fluoride ions and, therefore, lead to inhomogeneous etched porous layers [70,71].

In the following, we investigate the dependency of the hydrogen bubble size on the ethanol concentration in the PSI electrolyte. For this, we need the experimentally determined properties surface tension, density, and contact angle. The calculations [102] were performed considering a bubble sitting on a surface in the moment close before the detachment as indicated by Figure 51.

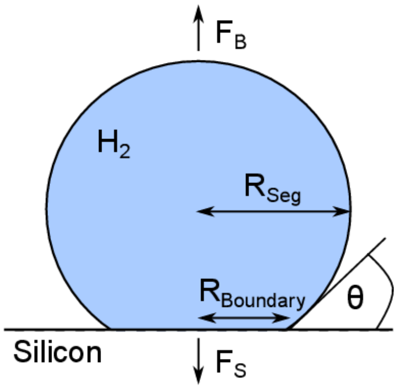

Figure 51: Schematic representation of a bubble on a surface close to detachment.

Figure 51 indicates that the buoyancy force F_B and the surface tension force F_S are in equilibrium before the bubble detaches, i.e., the sum of F_B and F_S is considered as zero.

$$\vec{F}_B + \vec{F}_S = 0 \tag{5.5}$$

The bubble is approximately a sphere. Hence, the buoyancy force F_B is defined as

$$\vec{F}_B = V_S \cdot (\rho_L - \rho_V) \cdot g \cdot \vec{e}_z \tag{5.6}$$

Here, V_S is approximately the volume of the sphere, ρ_L and ρ_V are the densities of the liquid and the vapor, g is the standard gravity, and e_z a vector in z-direction. The surface tension force F_S is

$$\vec{F}_S = -2\pi\sigma R \sin^2\theta \cdot \vec{e}_z \tag{5.7}$$

with the surface tension σ, the radius of the bubble R, the contact angle θ and e_z a vector in z-direction.

We are interested in the radius R of the bubble in the moment before the bubble detaches from the surface. Therefore, we will consider the spherical segment V_{Seg} instead of V_S in the following.

$$V_{Seg} = \frac{2}{3} R^3 \sin^2\left(\frac{\theta}{2}\right) \cdot \left(3 - \sin^2\left(\frac{\theta}{2}\right)\right) \tag{5.8}$$

Considering equations (5.5) to (5.8) and solve for R the radius of the segment R_{Seg} is calculated as

$$R_{Seg} = \sqrt{\frac{2\pi\sigma\sin^2\theta}{\frac{2}{3}\sin^2\left(\frac{\theta}{2}\right) \cdot \left(3 - \sin^2\left(\frac{\theta}{2}\right)\right) \cdot (\rho_L - \rho_V) \cdot g}} \tag{5.9}$$

The radius $R_{boundary}$ is the radius of the bubble in contact with the boundary surface [103]

$$R_{boundary} = R_{Seg} \sin\theta \qquad (5.10).$$

Here, the experimental results for the surface tension, the contact angle and the density of the electrolyte are required. The radius $R_{boundary}$ is calculated considering the density of hydrogen gas (0.0899 kg/m^3) and shown as a function of the ethanol concentration in Figure 52.

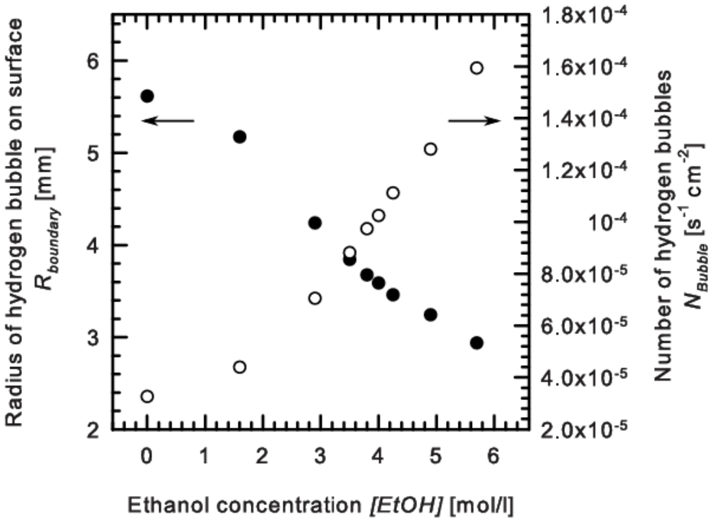

Figure 52: Calculated radius of hydrogen bubbles before detachment (black circles) and number of hydrogen bubbles (white circles) as a function of the ethanol concentration in the PSI electrolyte.

The size of the hydrogen bubble is clearly related to the ethanol concentration in the electrolyte. The hydrogen bubbles have a radius between 2 and 6 mm in the investigated concentration range. The more ethanol is in the electrolyte the smaller is the radius of the bubble. It is essential for the etching results that the hydrogen bubbles are small before they detach from the surface. The longer a bubble stays detached on the surface, the more it hinders the diffusion of fresh HF_2^- to the etch front. It is reasonable to suggest inhomogeneous etching here. Figure 52 shows that the size of the hydrogen bubble increases linearly with decreasing ethanol concentration.

In the following, we estimate the number of expected hydrogen bubbles [s^{-1} cm^{-2}]. The parameters for the calculations are listed in Table 5.1; the constants are listed in Appendix 9.

Table 5.1: Parameters for the calculation of the hydrogen bubble formation on porous Si.

Parameter	Value
Etching area *A*	1 cm^2
Etch rate *r*	1 µm/min
Porosity *P*	22%
Valence *n*	2.6

The volume of Si dissolved per time is

$$\frac{dV_{Si}}{dt} = A\,r\,P\,t \tag{5.11}$$

The amount of substance n_{Si} is accordingly

$$\frac{n_{Si}}{dt} = \frac{V_{Si}\,\rho_{Si}}{M_{Si}}\,t \tag{5.12}$$

The formation of the starting layer in the PSI process is dominated by the divalent dissolution mechanism as discussed in chapter 2.2.2 on page 11, in which the formation ratio for hydrogen is 1:1 for the dissolution of Si. No hydrogen is formed during the tetravalent dissolution and, therefore, neglected in these considerations here. The valence *n* determines how many silicon atoms are dissolved; it was calculated to 2.6 in chapter 2.2.2. The valence of 2.6 indicates that both dissolution mechanisms contribute to the formation of pores. We consider the amount of substance of hydrogen to be formed during the pore formation as

$$\frac{n_{H_2}}{dt} = n_{Si}\left(1 - \frac{n-2}{2}\right)\,t \tag{5.13}$$

The volume of the formed hydrogen gas calculates according to

$$\frac{V_{H_2}}{dt} = n_{H_2} V_{mol}\,t \tag{5.14}$$

with V_{mol} as the molar volume of a gas assuming hydrogen as an ideal gas. Then, the volume of hydrogen that is formed per time is calculated with

$$\frac{dV_{H_2}}{dt} = V_{mol}\frac{A\,r\,P\,\rho_{Si}}{M_{Si}}\left(1 - \frac{n-2}{2}\right)\,t \tag{5.15}$$

The number of hydrogen bubbles N_{Bubble} is related to the volume of hydrogen and the spherical segment V_{Seg} calculated in equation (5.8).

$$\frac{dN_{Bubble}}{dt}=\frac{V_{mol}}{V_{Seg}}\frac{A\,r\,P\,\rho_{Si}}{M_{Si}}\left(1-\frac{n-2}{2}\right)\,t \tag{5.16}$$

Finally, *N_{Bubble}* per area *A* is calculated according to

$$\frac{\frac{dN_{Bubble}}{dt}}{A}=\frac{V_{mol}}{V_{Seg}}\frac{r\,P\,\rho_{Si}}{M_{Si}}\left(1-\frac{n-2}{2}\right)\,t \tag{5.17}$$

The results are shown in Figure 52. We see that the number of estimated hydrogen bubbles per etched cm^2 is very low; however, the number increases with increasing ethanol concentration. This is related to the smaller sizes of the bubbles. The ethanol in the electrolyte thus leads to the formation of more but smaller bubbles compared aqueous HF solutions indicated at zero ethanol concentration in Figure 52. The size of the bubble should be kept as low as possible in order to give the HF_2^- access to the etching front.

Solubility of hydrogen gas

The following paragraph investigates the solubility of hydrogen gas in the PSI electrolyte. Since ethanol is added to the electrolyte in order to facilitate the release of hydrogen bubbles from the Si surface, a high solubility of hydrogen should be beneficial for the etching process particularly if reasonable amounts of hydrogen are formed.

Figure 53 illustrates the solubility of hydrogen in ethanoic solution as a function of the ethanol concentration [104].

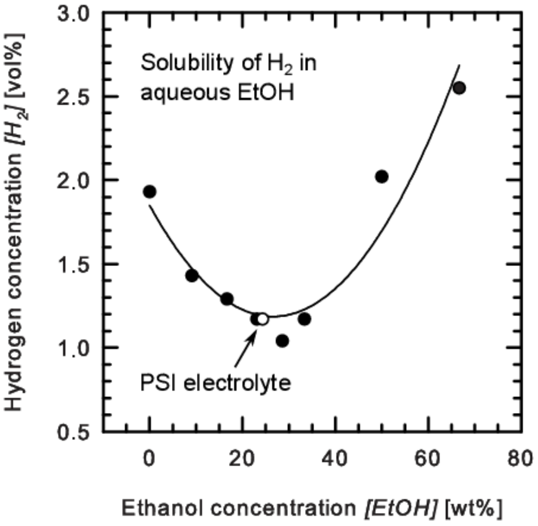

Figure 53: Solubility of hydrogen in EtOH-H_2O mixtures at 20 °C and 760 mm Hg adapted from [104]. The black circles illustrate the literature data, the white circle the ethanol concentration in the PSI electrolyte.

The calculation above allow for an estimation of the volume of hydrogen formed during the etching process. V_{Seg} from equation (5.8) describes the volume of a single hydrogen bubble. We calculate the volume of formed hydrogen as

$$V_{H_2,total} = V_{Seg}\, N_{Bubble}\, A\, t \tag{5.18}$$

considering the PSI substrate with an etching area A of 145 cm^2 and an etching time t of 60 s. V_{Seg} and N_{Bubble} are taken from Table E8 on page 145 for an ethanol concentration of 5.7 mol/l. The solubility calculates as the ratio of the hydrogen volume and the etching bath volume of 14.9 L.

$$\frac{V_{H_2,total}}{V_{Etching\,Bath}} = \frac{0.038\ \text{ml}}{14900\ \text{ml}} = 2.5\cdot10^{-6}\ \text{ml}\ H_2/\text{ml electrolyte} \tag{5.19}$$

We find that the volume of formed hydrogen per minute and per ml etching bath is very low. For water, the solubility of hydrogen is reported as 0.018 ml H_2/ml H_2O at 293 K [105], whereas for aqueous ethanol 0.017 ml H_2/ml is reported for a concentration similar to the electrolyte [104]. Consequently, the solubility of hydrogen plays a rather minor role for the performance of the etching bath.

Diffusion coefficient of HF_2^-

The diffusion of the active etching species HF_2^- to the etch front is essential for the etching process. Here, we investigate how the diffusion of the HF_2^- is influenced by the decrease of the ethanol concentration in the electrolyte.

The diffusion of an ions or molecules is described by its diffusion coefficient D in cm^2/s according to the *Stokes-Einstein equation* [58]

$$D = \frac{k_B T}{6\pi\eta R_0} \tag{5.20}.$$

Here, k_B is the Boltzmann constant [J/K], T is the temperature [K], π is 3.1415, η is the dynamic viscosity [Ns/m^2] and R_0 is the hydrodynamic radius [m]. The effective diffusion coefficient D_e describes the effective diffusivity in porous media [106].

$$D_e = \frac{\varepsilon_t \delta}{\tau} D \tag{5.21}$$

Here, ε_t is the porosity that is available for the transport, i.e., pores that are not accessible for the diffusion are not considered here. The constrictivity δ describes the decrease of the diffusion velocity due to the increased viscosity in narrow pores. The tortuosity τ finally is a factor that describes the rate of tortuousness, i.e., the form of the pores, if they are straight or loopy.

The diffusion coefficient *D* depends on the viscosity of the electrolyte that was experimentally determined above. Due to the disagreement with the theoretical viscosity of HF it is not possible to give absolute values concerning the dependency of the diffusion coefficient on the ethanol concentration here. However, a rough estimation of the development of the diffusion is given.

The diffusion coefficient *D* and D_e are calculated according to equations (5.20) and (5.21). Note, that the unit Pa·s equals Ns/m^2 for the determination of the diffusion coefficient. The hydrodynamic radius R_0 is the radius of the diffusing ion or molecule under consideration of the associated salvation shell. Here, R_0 was calculated solving equation (5.20) with the literature value for the diffusion coefficient of HF_2^- in water, which is $1.997 \cdot 10^{-5}$ cm^2/s [93]. In ethanoic solutions values in the range of $2.2 \cdot 10^{-5}$ cm^2/s were reported in literature [39]. In equation (5.21) the porosity ε_t was taken as 22% due to the starting layer of the mesoporous Si in the PSI process assuming that all pores are accessible for diffusion, the constrictivity δ and the tortuosity τ were considered as further constants. Figure 54 shows the general development of the diffusion coefficient *D* and the effective diffusion coefficient D_e as a function of the ethanol concentration in HF-EtOH-H_2O.

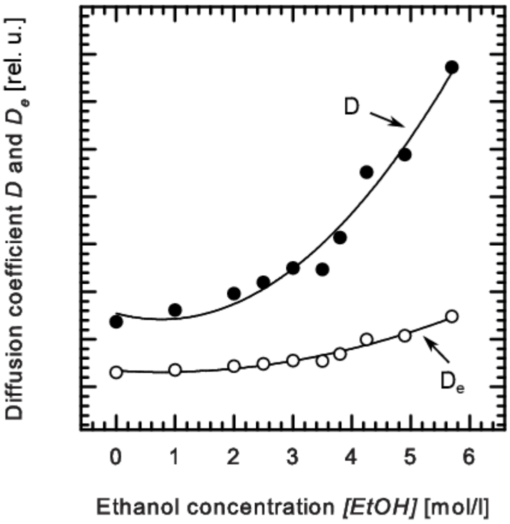

Figure 54: Development of the diffusion coefficient *D* (in black circles) and the effective diffusion coefficient D_e (in white circles) of HF_2^- in HF-EtOH-H_2O solutions as a function of the ethanol concentrations.

The diffusion of HF_2^- is facilitated through the addition of ethanol to the HF in terms of the diffusion coefficient *D*. The more ethanol is in the electrolyte, the faster is the diffusion of HF_2^-. For the etching process, the diffusion of HF_2^- into the pores and to the Si/HF interface is essential due to the consumption of HF_2^- during the reaction with Si. Therefore, it is reasonable to suggest a correlation between the diffusion of the HF_2^- and the etching result. However, the effective diffusion coefficient D_e is not reasonably affected by the ethanol concentration in the electrolyte. Thus, the diffusion in the pores may be less affected by the ethanol concentration than is the diffusion of HF_2^- in the electrolyte.

5.3 CONCLUSIONS

This chapter discusses the influence of the ethanol concentration on the wetting behavior of the PSI electrolyte. Therefore, a number of experiments were performed in order to determine the electrolytes properties in terms of surface tension, density, viscosity, contact angle, and ability to permeate through porous Si. The experiments demonstrated that the investigated properties all depend on the ethanol concentration in the electrolyte since they all decrease with increasing ethanol concentration.

Subsequently, the properties of the electrolyte were used for the calculation of the hydrogen bubble size and the amount of expected bubbles per time and area. This is interesting, because ethanol is added to the electrolyte as a wetting agent that should decrease the surface tension – which it does according to the experiments above – resulting in a facilitated detachability of the hydrogen bubbles that form during the dissolution reaction of Si. The calculations demonstrate that the size of the bubbles on the surface depends on the ethanol concentration. The higher the ethanol concentration in the electrolyte is the smaller are the hydrogen bubbles. Even the number of hydrogen bubbles depends on the ethanol content, leading to the conclusion that in an electrolyte with a high ethanol concentration more but smaller hydrogen bubbles exist. Therefore, the detachment is improved through the addition of ethanol.

The detachability of hydrogen bubbles is very important for the PSI process. We understand that where a hydrogen bubble sits no further HF_2^- can reach the etching front, therefore, acting as a hindrance for the performance of homogeneous etching. Where the bubble sits, no fresh electrolyte may reach the etching front and thicker bridges may remain in the porous Si due to the absence of HF_2^- at this place. This is where the origin of cracks is expected.

The diffusion coefficient of HF_2^- was further investigated in this chapter. The diffusion of HF_2^- in the electrolyte is facilitated if ethanol is present in the electrolyte; however, the diffusion in the pores is less affected. In addition, the solubility of hydrogen seems to play a minor role for the presence of ethanol in the electrolyte. This is due to the low amounts of hydrogen formed during etching and confirmed by a comparison with data from literature.

As discussed in chapter 2.2.3 on page 17, the oxidation of ethanol to CO_2 within the electrochemical process is a possible source of ethanol loss. It is important to determine the ethanol concentration development and to replenish the ethanol in the electrolyte in order to obtain beneficial circumstances for homogeneous pore formation. The investigations in this chapter give evidence to suggest a critical ethanol concentration for the PSI electrolyte that is required for homogeneous pore formation. In consistency with the results of this chapter and our experience with the PSI process as discussed in chapter 4.1.2 on page 46, we recommend keeping the ethanol concentration between approximately 4.0 and 5.7 mol/l.

6 INFLUENCE OF DISSOLVED SILICON ON ELECTROCHEMICAL ETCHING

The electrochemical treatment of a Si wafer leads to the formation of pores and, furthermore, to dissolved Si that is released as SiF_6^{2-} into the electrolyte. The mechanisms of the formation of SiF_6^{2-} were discussed in detail in chapter 2.2.2 on page 11. This chapter investigates the behavior of porous Si in water and in aqueous solutions of SiF_6^{2-} in order to determine the impact of SiF_6^{2-} in the electrolyte. An overview of the reported influence of SiF_6^{2-} on the etching results is given. Furthermore, we discuss the possible impact of SiF_6^{2-} enrichment in the electrolyte on the electrochemical parameters for the PSI and the MacPSI process with regard to the results of chapter 4.

6.1 POROUS SILICON IN WATER

The surface of a Si wafer is usually covered by a layer of silicon dioxide (SiO_2). This paragraph deals with the formation of SiO_2 on a porous surface and focuses on the behavior of a mesoporous layer that is stored under water.

The surface of a Si wafer is naturally covered by a thin layer of native grown silicon oxide with the surface groups Si–H and Si–OH. These continue further to the formation of Si–O–Si since the oxidized "back bonds" are thermodynamically preferred over Si–H and Si–OH [107,108]. The native oxide establishes within several hours having a thickness of a few nanometers [109]. Miura and co-workers found an equilibrium thickness of 0.6 nm oxide when the Si is exposed to air [110,111]. The oxide thickness was determined by infrared absorption spectroscopy (IRAS) on *n*-type, phosphorous doped Si wafers with (100) and (111) orientation and was found to be independent of the surrounding humidity. We suggest a complete surface oxidation for the mesoporous Si from the PSI process due to the great surface area.

We found that water has a noteworthy impact on mesoporous Si. A mesoporous layer with a porosity of about 20% and a thickness of 30 µm dissolved in distilled water during a storage time of several weeks. The photographs in Figure 55 show the appearance of such a layer at the beginning and after four weeks of storage. The layer became more transparent with time and had a jellylike stiffness.

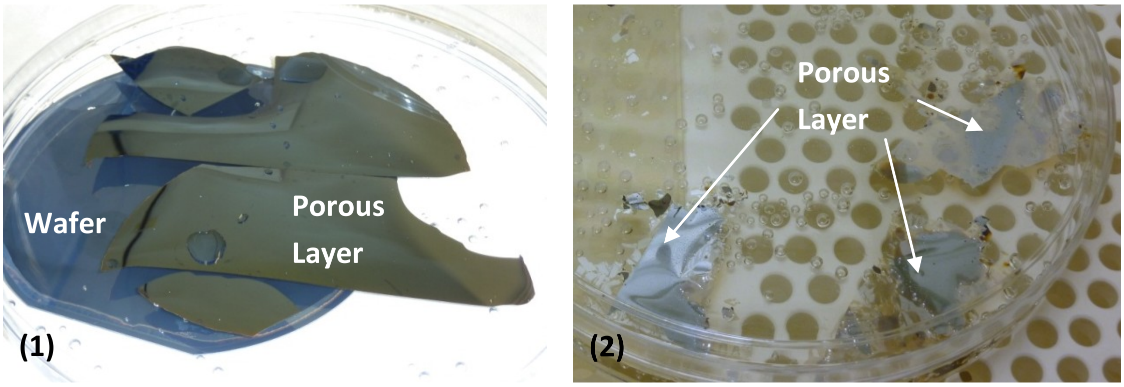

Figure 55: Photographs of a 30 µm thick mesoporous Si layer before (1) and after storage under distilled water for four weeks (2). The layer became more transparent with a jellylike stiffness.

The observation can be explained with the proceeding oxidation of the Si–O–Si bonds by water [96].

$$SiO_{2\,(s)} + 2\,H_2O_{(l)} \rightarrow Si(OH)_{4\,(aq)} \qquad (6.1)$$

Thus, the exposure of porous Si to water leads to the liberation of silicic acid as a result of the dissolution process. This reaction is accompanied by the formation of hydrogen gas, which is observable through the formation of bubbles.

In order to determine if SiF_6^{2-} has a similar dissolution effect as water, the influence of aqueous solutions of SiF_6^{2-} on porous Si is investigated in more detail in the following paragraph. Since the SiF_6^{2-} concentration increases during the lifetime of the etching bath, it is interesting to see if an effect on the etching process has to be taken into consideration.

6.2 POROUS SILICON IN AQUEOUS SOLUTIONS OF SiF_6^{2-}

For the investigation of the impact of aqueous SiF_6^{2-} solutions on porous Si a deeper understanding of the chemistry of SiF_6^{2-} is desired. The focus is on the experiments performed in this work which are related to the dissolution of porous Si by SiF_6^{2-}.

6.2.1 CHEMISTRY OF SiF_6^{2-}

Silicon hexafluoride is the reaction product of the electrochemical anodization of Si. It has an octahedral symmetry as illustrated in Figure 56. The six fluoride ions in the complex are equidistant.

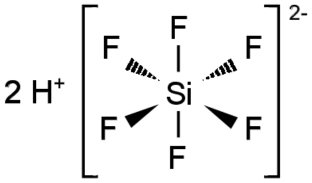

Figure 56: Molecular geometry of SiF_6^{2-}. The six Si-F bonds are equidistant.

SiF_6^{2-} is stable in aqueous solutions up to pH 3 [112]. Therefore, the investigations of this chapter were performed in the range of pH 1 to 3. In aqueous solutions above pH 3, SiF_6^{2-} dissociates and releases fluoride ions as well as soluble aquo-, hydroxo- and oxosilicates following the overall dissociation-hydrolysis process [113,114], i.e.,

$$SiF_6^{2-}{}_{(aq)} + 4\ H_2O_{(l)} \rightleftharpoons 4\ HF_{(aq)} + 2\ F^-{}_{(aq)} + Si(OH)_{4\ (aq)} \qquad (6.2).$$

Table 6.1 gives the thermodynamic data of SiF_6^{2-} that clearly indicate the stability of the complex.

Table 6.1: Thermodynamic data for SiF_6^{2-} [115].

Thermodynamics	Value
$\Delta_f H°_{298}$	-2389.1 kJ/mol
$\Delta_f G°_{298}$	-2199.4 kJ/mol
$S°_{298}$	122.2 J/mol·K

The acidity constants for the strong acid H_2SiF_6 in aqueous solutions are shown below.

$$H_2SiF_{6\ (aq)} \rightleftharpoons H^+{}_{(aq)} + HSiF_6^-{}_{(aq)} \qquad pKs_1 = 1.92 \qquad (6.3)$$

$$HSiF_6^-{}_{(aq)} \rightleftharpoons H^+{}_{(aq)} + SiF_6^{2-}{}_{(aq)} \qquad pKs_2 = -0.6 \qquad (6.4)$$

The dissolution of silicon dioxide by SiF_6^{2-} is described according to Gmelin [115] by two reaction paths:

$$4\ SiF_6^{2-}{}_{(aq)} + 2\ SiO_{2\ (s)} + 8\ H^+{}_{(aq)} \rightleftharpoons 6\ SiF_{4\ (aq)} + 4\ H_2O_{(l)} \qquad (6.5)$$

and

$$5\ SiF_6^{2-}{}_{(aq)} + SiO_{2\ (s)} + 4\ H^+{}_{(aq)} \rightleftharpoons 6\ SiF_5^-{}_{(aq)} + 2\ H_2O_{(l)} \qquad (6.6).$$

The equilibrium constants

$$K = \frac{[SiF_4]^6}{[SiF_6^{2-}]^4\,[H^+]^8} = 7\cdot 10^{-8} \qquad (6.7)$$

and

$$K = \frac{[SiF_5^-]^6}{[SiF_6^{2-}]^5\,[H^+]^4} = 9 \cdot 10^{-2} \tag{6.8}$$

were also taken from [115]. The equilibrium constants in equations (6.7) and (6.8) indicate the favorable formation of SiF_5^- compared to SiF_4.

6.2.2 EXPERIMENTAL INVESTIGATIONS

As discussed above, water dissolves oxidized porous Si. This paragraph investigates if aqueous solutions of SiF_6^{2-} have a similar effect. An increased Si concentration in the sample solution would indicate that SiF_6^{2-} is dissolving the porous Si. Due to the reactions described in equations (6.5) and (6.6), the investigation includes porous Si with and "without" native grown oxide, i.e., with the least possible amount of grown oxide.

Experimental details

Solutions with dissolved Si were prepared from hexafluorosilicic acid H_2SiF_6 (35 wt% in H_2O, Alfa Aesar, Germany) in concentrations of 0.18 mmol/l Si with pH 1, pH 2, and pH 3. The initial concentration of 0.18 mmol/l Si was chosen in order to fit to the measurement range of the ion-chromatography according to chapter 3.3 on page 33. The solutions with pH 1 and 2 were adjusted with hydrochloric acid (HCl, 37%, semiconductor grade VLSI PURANAL®, Honeywell, Germany), while the solution with pH 3 contain no additional acid since the protons from H_2SiF_6 are sufficient to reach the required pH. Due to the observed effect of water, the investigation was expanded for the influence of distilled water. Therefore, water samples were prepared with pH 1, pH 2, and pH 3 – all prepared with HCl – to investigate the influence of water with regard to the dissolution of porous Si.

The porous Si samples with native grown oxide were allowed to age for about four months in air, samples without native oxide were processed as quickly as possible after emerging the porous Si from the etching solution. The "quickly as possible" was indeed 10 to 24 min due to the time required for cutting the porous layer into pieces, drying it from rinsing water, and weighing.

The prepared solutions were each brought into contact with about 0.1 g mesoporous Si from the PSI process with a porosity of about 20% and a thickness of about 30 µm. One group contained aged – oxidized – porous Si; the other group freshly prepared porous Si. Samples of the solutions were taken at the beginning and after reaction times of 0 s, 20 s, 40 s, 60 s, 80 s, 100 s, 120 s, 5 min, 10 min, 30 min, and 60 min, respectively. The analysis of the samples was performed by IC with post-column derivatization and the concentration of Si in solution followed over time.

Figure 57 shows the development of the dissolved Si concentration in samples with distilled water. The graph on the left side illustrated the dissolution of oxidized porous Si, whereas the graph on the right side pictures the dissolution of non-oxidized porous Si. The observed increase of the Si concentration is due to the dissolution of porous Si by water. There is no clear dependency on the pH of the water solution observable since the results are within their uncertainties. However, the dissolved Si concentration increases with proceeding time of the experiment for all sample solutions. The observed increase is independent on the presence of oxide on the surface.

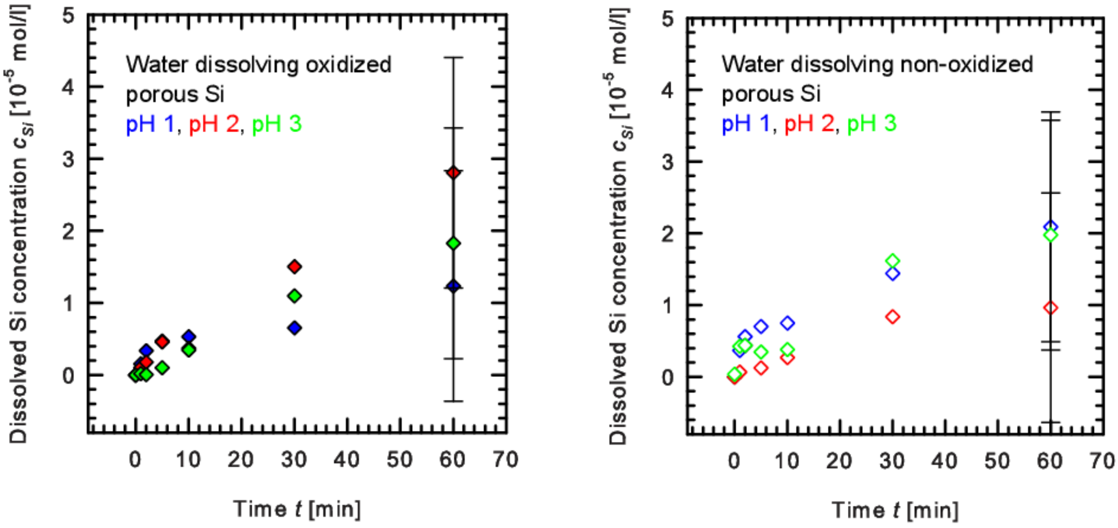

Figure 57: Development of the dissolved Si concentration in water samples in contact with porous Si. The graph on the left side shows the dissolution of oxidized porous Si, the graph on the right side the dissolution of non-oxidized porous Si. An exemplary error is given. The color of the data points correspond to the pH of the sample: blue for pH 1, red for pH 2, green for pH 3.

The amount of dissolved Si that is due to the reaction of SiF_6^{2-} with the porous Si is indicated by $[Si]_{dissolved}$ in the following. It is obtained by

$$[Si]_{dissolved} = [Si]_{measured} - [SiF_6^{2-}]_{initial} - [Si]_{water} \qquad (6.9),$$

where the amount of the initial Si (= 0.18 mmol/l) $[SiF_6^{2-}]_{initial}$ as well as the amount of the Si dissolved by water $[Si]_{water}$ – according to Figure 57 – is subtracted from the measured result $[Si]_{measured}$. The determination of the uncertainty of the result is attached to Appendix F.

Figure 58 illustrates the amount of Si that is dissolved by the SiF_6^{2-} in the aqueous solutions of pH 1, pH 2, and pH 3. The samples contain porous Si with grown oxide. The influence of water as well as the initial amount of Si in the solution were subtracted according to equation (6.9), therefore, the graph pictures the amount Si dissolved by SiF_6^{2-}.

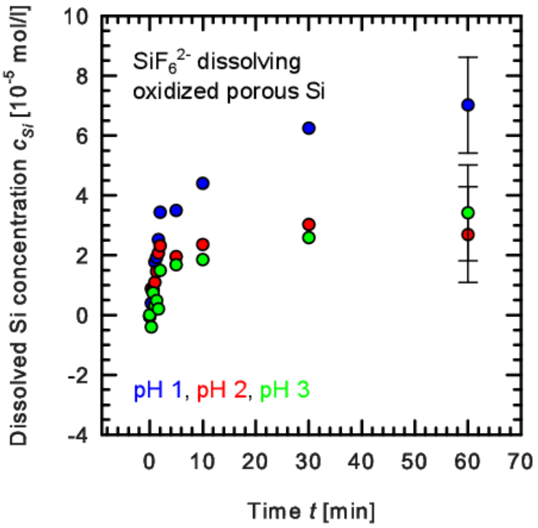

Figure 58: Development of the dissolved Si concentration in aqueous solutions of SiF_6^{2-} in contact with porous Si having a native grown oxide on the surface. The influences of the water as well as the initial Si concentration were subtracted according to equation (6.9). Therefore, the graph illustrates the amount of Si dissolved according to SiF_6^{2-} only. An exemplary error is given. The color of the data points correspond to the pH of the sample: blue for pH 1, red for pH 2, green for pH 3.

Negative data points indicate that – according to equation (6.9) – the amount of Si dissolved by water or the initial SiF_6^{2-} concentration exceeds the amount of Si that is dissolved during the reaction. The graph shows an increase of the Si concentration of up to $7{\cdot}10^{-5}$ mol/l additional dissolved Si in the sample. The greatest increase is observable within the first 2 min of the experiment. This is investigated in more detail in Figure 59.

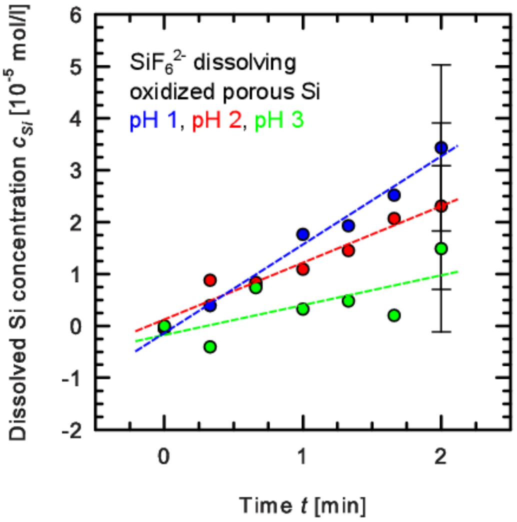

Figure 59: Development of the dissolved Si concentration of Figure 58 in the first two minutes of the experiment. An exemplary error is given. The color of the data points correspond to the pH of the sample: blue for pH 1, red for pH 2, green for pH 3.

A dependency on the pH of the solution is observable since the aqueous SiF_6^{2-} solution with pH 1 shows the strongest increase of the dissolved Si concentration per minute in this experiment. This indicates the acid catalyzed behavior of the reaction according to equations (6.5) and (6.6).

Figure 60 depicts the development of the dissolved Si concentration in samples containing porous Si "without" oxide on the surface. Again, negative data points indicate more Si is dissolved by water and $[SiF_6^{2-}]_{initial}$ than due to the reaction within the investigated period of time. In comparison to the similar experiment in Figure 58, the concentrations obtained here are rather constantly below $2 \cdot 10^{-5}$ mol/l.

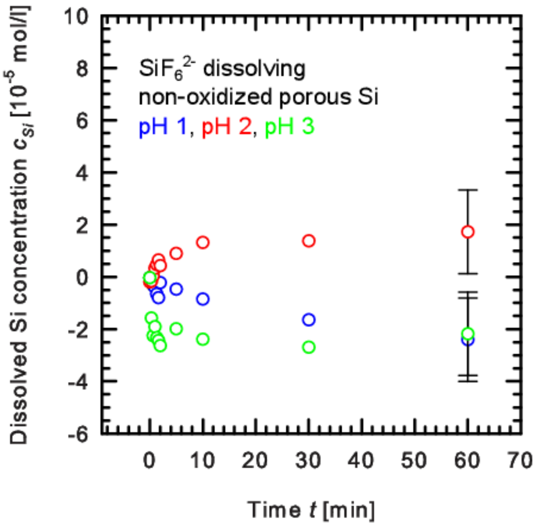

Figure 60: Development of the dissolved Si concentration in aqueous SiF_6^{2-} solutions in contact with porous Si without native grown oxide on the surface. An exemplary error is given. The color of the data points correspond to the pH of the sample: blue for pH 1, red for pH 2, green for pH 3.

The comparison of Figure 58 and Figure 60 shows that the rapid increase of the dissolved Si concentration within the first two minutes of the experiment is observable only for samples with oxidized porous Si. According to equations (6.5) and (6.6), the dissolution rate depends on the pH of the solution. The most rapid dissolution is observed at pH 1 in Figure 59, and therefore, attributed to the dissolution of the silicon oxide on the porous Si. Furthermore, freshly prepared porous Si with a non-oxidized surface is not dissolved by aqueous solutions of SiF_6^{2-}.

It is interesting to see how much Si was dissolved within the experiments compared to the overall amount of silicon oxide on the surface. The calculation takes the thickness of the silicon oxide as 0.6 nm from Miura [110], the surface area of 230 m^2/cm^3 from Herino [48], the amount of 0.1 g porous Si in this experiment, and the density of the porous Si into consideration. Details are given in Appendix F. So, we calculate the mass of silicon oxide on a piece of porous Si sample as used in this experiment to 20 mg. Accordingly, the maximum concentration of the dissolved Si would be $3.5 \cdot 10^{-3}$ mol/l if all silicon oxide would be dissolved. Thus, there is still some silicon oxide left on the porous Si and none of the investigated solutions is able to dissolve the silicon oxide completely.

In contrast to the electrochemical Si dissolution mechanisms discussed in chapter 2.2.2 on page 11, the porous Si in this chapter dissolves via a strictly chemical route. Therefore, the Si–O network needs to be opened in order to enable the nucleophilic attack of the fluoride ions from the SiF_6^{2-} described in equations (6.5) and (6.6). A Si network that has been opened accordingly has Si–OH surface groups offering enough space for the fluoride for attack. Any fluorinated species in HF solutions may provide the required fluoride ion [116]. Table 6.2 lists the bond energies for various Si–X, demonstrating the energetic stability of Si–F against Si–O or Si–H [63].

Table 6.2: Chemical bond energies [63].

Chemical bond	Bond energy [kJ/mol]
Si–F	541.35
Si–O	369.28
Si–H	294.75
Si–Si	176.68

The attack of fluoride on oxidized Si leading to a Si–F bond is therefore energetically favorable. The experimental results obtained in this paragraph suggest that SiF_6^{2-} is a possible provider of fluoride for the dissolution of oxidized porous Si. Therefore, a slight promotion of local Si dissolution caused by SiF_6^{2-} is conceivable.

6.3 SIGNIFICANCE OF SiF_6^{2-} FOR ELECTROCHEMICAL ETCHING

In the following paragraph, the observations concerning the behavior SiF_6^{2-} in aqueous solutions in the presence of porous Si are related to the etching procedure for the PSI process. The paragraph starts with a short literature overview and proceeds with an estimation of the impact of an increased SiF_6^{2-} concentration on the electrochemical reactions in the PSI etching process as discussed chapter 2.2.3 on page 13.

Literature overview concerning the influence of SiF_6^{2-} on electrochemical etching

The general dependancy of etching parameters on the composition of the etching bath is well known in literature. For example, Hickling reported an influence of the copper concentration in solution on the critical current density required for electropolishing in various electrolytes [117]. The following gives an overview concerning the reported impacts of SiF_6^{2-} in literature. The group of Acker reported an increase of the etching rate with increasing concentration of SiF_6^{2-} in acidic texturization baths consisting of HF and HNO_3 [118]. Even more, for the same electrolyte an influence on the surface texturing is observed [18]. On the other hand, Turner investigated as one of the earliest in 1958 the influence of SiF_6^{2-} on the critical current density to start electropolishing of *p*-type Si in aqueous solutions of 5% HF. Yet, he found no dependancy for H_2SiF_6 concentrations of 0 to 25 wt% on the critical current density [41]. According to Unagami, the SiF_6^{2-} remains in the porous layer and acts as a hindrance layer to the following anodization; consequently, further anodization can only proceed where no SiF_6^{2-} is present [119]. However, no information is presented with regard to the required amount of SiF_6^{2-}. On the opposite, Monk and co-workers found evidence that SiF_6^{2-} diffuses away from the reaction surface due to the concentration gradient and, hence, no interference of further etching is observed [116]. Thus, neither a support nor a reasonable hindrance of the electrochemical etching process itself due to the increased SiF_6^{2-} concentration is reported.

At this point, it is important to consider the very low Si concentration in the PSI etching bath for further discussions. As the experimental results above demonstrate, SiF_6^{2-} is able to dissolve porous Si with an oxidized surface. However, the silicon oxide can of course be dissolved by HF as well, which was not added to the investigated solutions in the experiment above. Therefore, it is interesting to compare the thermodynamic data for the silicon oxide dissolution by SiF_6^{2-} and by HF. The dissolution by SiF_6^{2-} was introduced above in equation (6.6). Table 6.3 lists the thermodynamic data.

Table 6.3: Thermodynamic data for the dissolution of silicon dioxide by HF and by SiF_6^{2-} as listed in [115,120]. Data marked with an asterisk* were calculated from thermodynamic data according to [58,115].

Dissolution path	$6\,F^- + 4\,H^+ + SiO_2 \rightleftharpoons SiF_6^{2-} + 2\,H_2O$	$5\,SiF_6^{2-} + SiO_2 + 4\,H^+ \rightleftharpoons 6\,SiF_5^- + 2\,H_2O$
Equilibrium constant *K*	$2 \cdot 10^{25}$*	$9 \cdot 10^{-2}$
Enthalpy of formation $\Delta_f H°_{298}$ [kJ/mol]	-2389.1	-657.22*

The comparison of the equilibrium constants *K* and the enthalpies of formation $\Delta_f H°_{298}$ indicates the superior role of HF in the dissolution of silicon dioxide.

Nevertheless this paragraph deals with the influence of SiF_6^{2-} on the electrochemical etching bath. This is due to the observation at ISFH that the addition of some used electrolyte to a fresh prepared PSI etching bath supports the formation of porous layers. The difference of the used to the fresh electrolyte is, of course, the existence of the reaction product SiF_6^{2-}. However, assuming that 400 wafers were etched and the value of about 20 mg Si/wafer – as determined by gravimetric analysis – is reasonable, the concentration of SiF_6^{2-} would be around 9 mmol/l in an etching bath of 30 liters after replenishment. Considering then, that about 200 ml of the old etching solution are added to the new bath this leads to a SiF_6^{2-} concentration of about 0.1 mmol/l. This concentration range was investigated above in terms of the impact of SiF_6^{2-} on porous Si. Since the dissolution experiments demonstrate that SiF_6^{2-} is able to dissolve oxidized porous Si, it is reasonable to investigate the impact of SiF_6^{2-} on the etching process in more detail.

Influence of increased SiF_6^{2-} concentration on the electrochemical reactions

The electrode potentials discussed regarding the electrochemical reactions in chapter 2.2.3 depend on the concentrations of the chemical constituents. The concentration of SiF_6^{2-} is associated with the amount of etched wafers within one electrolyte bath. It is interesting to see if the rising concentration of SiF_6^{2-} has a considerable impact on the potentials in the electrochemical setup. The electrochemical reaction considering the reaction product SiF_6^{2-} is

$$Si + 6\,F^- \rightarrow SiF_6^{2-} + 4\,e^- \qquad (2.9)$$

with the standard electrode potential $E^0 = -1.37$ V. With the Nernst Equation introduced in equation (3.4) we calculate the development of the potential with regard to the increased SiF_6^{2-} concentration, the results are shown in Figure 61.

We find that the electrode potential is constant within a range of 0.05 V for the investigated concentration range of SiF_6^{2-} from 0.001 mol/l to 10 mol/l. The SiF_6^{2-} concentration of 10 mol/l is dedicated to a certain number of etched wafers *#(wafer)* according to

$$\#(\mathrm{wafer}) = \frac{c_{Si}\, V_{bath}\, M_{Si}}{m_{per\ etched\ wafer}} \qquad (6.10)$$

where the c_{Si} is the concentration of SiF_6^{2-}, i.e. 10 mol/l, V_{bath} is the volume of the PSI or MacPSI electrolyte, M_{Si} is the molar mass of Si, and $m_{per\ etched\ wafer}$ is the mass of Si that is dissolved per etched wafer (please see chapter 4).

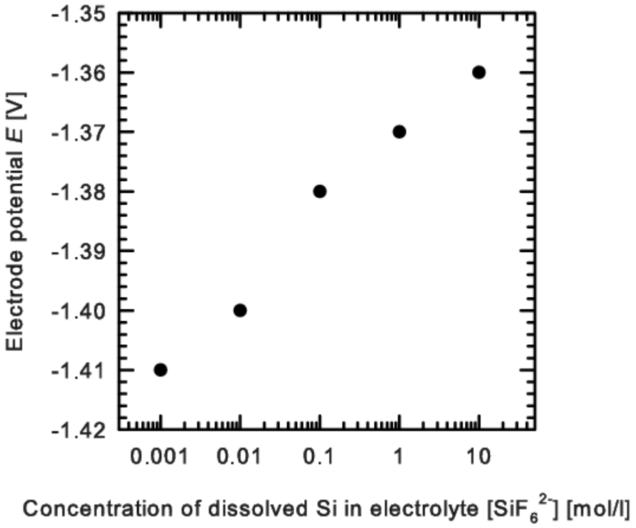

Figure 61: Predicted development of the electrode potential with regard to the increased SiF_6^{2-} concentration.

In the PSI electrolyte, the SiF_6^{2-} concentration of 10 mol/l is obtained if more than 400 000 wafers are etched, in the MacPSI electrolyte etching of about 2500 wafers is required. These numbers of etched wafers are relatively high. Thus, a considerable change of the electrode potential is not expected as a result of the enrichment of the reaction product SiF_6^{2-} in the electrolyte. As a result, it is not necessary to consider the increased concentration of SiF_6^{2-} in the electrolyte in terms of the electrochemical equilibria in the systems for the etching processes performed at the ISFH. Therefore, the etching parameters required for homogeneous pore formation do not need to be adjusted due to the increased concentration of SiF_6^{2-}.

However, these results are in contrast to the observations concerning the requirement of some old electrolyte for homogenous pore formation in the PSI process. Since the etching results in the SSE tool are sacrificial in terms of their detachability even in fresh prepared electrolytes so far, we suppose that the observation is merely attributed to the ISFH tool than to a general fact.

6.4 CONCLUSIONS

This chapter deals with the influence of the reaction product SiF_6^{2-} on the etch procedure. At the beginning the chemical reaction of SiF_6^{2-} with porous Si is investigated taking into consideration porous Si with and without silicon oxide on the surface. The experimental results demonstrated that SiF_6^{2-} is able to dissolve porous Si if the surface is oxidized. Samples containing freshly prepared porous Si with the least possible amount of oxide on the surface show no increase of the Si concentration in the solution.

In addition, the impact of SiF_6^{2-} on the electrochemical equilibria in the etching setups is discussed, especially in terms of the adjustment of the etching parameters. In chapter 2.3 on page 20, we focused on the homogeneous pore formation that is influenced by the etching parameters. Here, it was determined whether an increased SiF_6^{2-} concentration affects the electrode potentials with the consequence that an adjustment of the etching parameters would be necessary. The investigated concentration range for SiF_6^{2-} was 0.001 - 10 mol/l which represents up to 400 000 etched wafers in the PSI tool or 2500 etched wafers in the MacPSI tool. We found that the electrode potential would change in a range of max. 0.05 V. This change would not require any adjustment of the etching parameters. Consequently, no impact concerning the SiF_6^{2-} concentration is expected that limits the usability of the investigated electrolytes in any way.

7 SUMMARY

In this thesis, the chemical compositions of the electrolytes were investigated that are used in electrochemical etching baths for the formation of meso- and macroporous Si at the ISFH. The focus is on the evaluation of chemical analysis methods that are appropriate to use in these highly HF concentrated electrolytes. In addition, the impact of variations in the electrolyte – decreasing ethanol concentration and increasing dissolved Si concentration during the bath lifetime – are investigated concerning their impact on the etching process.

The etching processes investigated here are the PSI (Porous Si) process for the formation of mesoporous Si with the electrolyte consisting of 19.5 mol/l HF and 5.7 mol/l ethanol. The mesoporous Si is part of a modern concept for thin Si solar cells that requires no ingot sawing. The second electrolyte is used in the MacPSI (Macroporous Si) process for the formation of macroporous Si containing 1.43 mol/l HF and 1.14 mol/l acetic acid. The macroporous Si layer can be used as an absorber in solar cells. Both investigated electrolytes have in common the reaction product of the Si dissolution, which is SiF_6^{2-}. Due to the interest of industrial application in case of the PSI process, the focus of this work is on the etching process for mesoporous Si; however, the investigated chemical analysis methods are adapted to the MacPSI process where possible.

The porous Si consists of a double layer with two different porosities: a lower porosity on top and a higher porosity underneath. The lower porosity layer is used as a separation layer in the PSI process and requires a homogeneous distribution of narrow Si bridges in order to enable a defect-free detachment from the substrate wafer. The etching parameters for the formation of a proper separation layer depend on the concentration of HF in the electrolyte. In order to gain reproducible etching results it is required to keep the HF concentration constant. An aim of this work was to investigate chemical analysis methods that are suitable for the determination of the concentration of HF in the electrolyte.

The etching of the mesoporous Si at ISFH is performed in the dark on *p*-type Si substrate wafers. The holes that are required for the electrochemical dissolution mechanisms are therefore available in the bulk Si due to the doping of the substrate with boron. On the other hand, the macropores at ISFH form in *n*-type Si substrate wafers under illumination of the rear-side generating the holes. The electrochemical etching setup for the PSI process at ISFH was investigated in detail in terms of an estimation of the probability of the chemical reactions. There is no reference electrode integrated in the etching system, which is the reason for the estimation. In addition to the anodic Si dissolution, the formation of molecular hydrogen at the cathode takes place. Furthermore, we expect that ethanol oxidizes during the etching process. The end product of the oxidation is gaseous CO_2, which leads to an overall depletion of the organic species in the electrolyte.

The technical part of this thesis includes the evaluation of chemical analysis methods that are suitable for the determination of the etching bath constituents. Under investigation were titration with $La(NO_3)_3$ as well as a fluoride-ion selective electrode (F-ISE) for the determination of the fluoride concentration, a commercially available cuvette test method for the organic substances, and ion-chromatography (IC) for the determination of the rising SiF_6^{2-} concentration. A challenge was the determination of the low SiF_6^{2-} concentrations in a matrix of highly concentrated hydrofluoric acid. The IC – equipped with a post-column derivatization device – was identified as suitable for the determination of the SiF_6^{2-} in the PSI etching bath. The use of the organic acids column delayed the undissociated HF and, thus, enables evaluable Si signals. All chemical analysis methods were evaluated concerning their applicability on the PSI etching baths. The reliability of titration and F-ISE were investigated by reference measurement; the accuracies of all methods were determined by the recovery rates. Furthermore, the MacPSI etching bath was investigated to spread the applicability of the methods.

In this work, the introduced chemical analysis methods were used for the analysis of two etching setups for the formation of mesoporous Si within the PSI process, the ISFH tool and the SSE tool. The analysis was performed using titration for the fluoride concentration, the cuvette test method for ethanol, and the IC for SiF_6^{2-}. In addition, the MacPSI etching bath was investigated by applying the F-ISE for the fluoride concentration, the cuvette test method for the acetic acid, and again the IC for SiF_6^{2-}. The chemical analysis enabled the identification of the reasons for the high HF consumption in the ISFH tool prior to this work. Those were mainly due to technical circumstances and related to the fact that the ISFH tool is not hermetically sealed to minimize the risk of explosion (the etching electrolyte is a potentially explosive mixture). Consequently, the loss of HF due to evaporation out of the reservoir has to be accepted and clearly demonstrates the importance of chemical analysis for the PSI process. The chemical analysis enables the replenishment of lost HF and consequently the enlargement of the etching bath's lifetime. These insights influenced the design of a modern etching tool – the SSE tool – which is a prototype that is currently located at ISFH. Therefore, the development of the chemical concentrations of the electrolyte in the SSE tool was also investigated. Here, the HF concentration was found to be constant during more than 700 etched wafers increasing the number of etched wafers from about 250 to more than 700 wafers compared to the ISFH tool. It should be noted that this limit referred to the circumstance that the tool required technical adjustment; it does not indicate the general limit for the usability of the electrolyte. Concerning the development of the ethanol concentration in the electrolyte we found a decrease of 3 mmol/l per etched wafer even in the closed SSE tool and identified the oxidation of ethanol during the etching process as a possible reason. Consequently, it is recommended to analyze the ethanol concentration periodically. This work identified the ethanol concentration as a possible limit for the usability of the etching baths. Further investigations concerning the ethanol concentration were performed in this work and are addressed below. For the determination of the SiF_6^{2-} a limit of 10 mmol/l was evaluated for analysis results that meet the average estimated theoretical values. With this, we identified a very slight increase of the dissolved Si concentration of about 0.06 mmol/l per PSI double layer.

The investigation of the SSE tool allows a rough estimation of the economy of the PSI process in terms of the HF consumption. The considerations lead to the number of 2000 etched wafers before a decrease of the HF concentration should be noticeable. A replenishment with the initial electrolyte concentration, i.e., with HF and ethanol, would increase the lifetime of the bath reasonably. This work demonstrates that the HF consumption during the porosification of the Si is not a limiting factor for the industrial realization of the PSI process.

In case of the MacPSI process the replenishment of the HF concentration is implemented in the software. The amount of consumed HF is relatively high due to the formation of macropores where about 0.5 g Si is dissolved per etching process. It is therefore required to replenish the HF after every etched wafer in order to keep the etching parameters constant. The investigated chemical analysis methods demonstrated their applicability on the MacPSI etching bath due to the agreement of the theoretical concentrations with the experimental results. There was no evidence of a decrease in the acetic acid concentration observable throughout the amount of etched wafers in the investigated period. The rising SiF_6^{2-} concentration was detectable with the IC method investigated in the technical part of this thesis; the detection was facilitated through the lower HF concentration in the MacPSI etching bath.

During the lifetime of the PSI etching bath, the ethanol concentration was found to decrease. Therefore, the chemical part of this thesis investigates the development of the properties of the electrolyte with decreasing ethanol concentration. Considered are the surface tension, the density, the contact angle, the viscosity, and the ability to permeate through a porous Si membrane. With the exception of the contact angle, all experiments were performed with HF-EtOH-H_2O solutions representing the etching electrolyte. We found that these properties depend linearly on the remaining ethanol concentration in the electrolyte. With these data, the impact of ethanol on the etching procedure is discussed in terms of the detachability of hydrogen bubbles. Hydrogen bubbles form during the etching process on the Si wafer. If a bubble sits on the etching surface, it hinders the HF_2^- to reach the etching front. Thus, the etching is expected to be inhomogeneous here, which could be a cause for the formation of thicker Si bridges in the separation layer of the porous double layer. Thicker bridges are possible origins for cracks in the detached porous layer. This work showed that the size and the number of hydrogen bubbles theoretically depend on the ethanol concentration in the electrolyte. Consequently, the impact of hydrogen bubbles as a cause of inhomogeneous etching could be controlled by the monitoring of the ethanol concentration in the bath and appropriate replenishment. The more ethanol is in the electrolyte, the smaller is the size of the bubbles sitting on the substrate before they detach. The number of bubbles was found to increase with increasing ethanol concentration, which is related to the smaller sizes of the bubbles. However, the existence of big bubbles is more critical to the homogeneous etching than the existence of small but many bubbles. Thus, the more ethanol is in the electrolyte the better is the etch performance.

The dissolved Si concentration increases during the electrolyte's lifetime. Here, the dissolution of porous Si was investigated experimentally indicating that SiF_6^{2-} is able to dissolve oxidized porous Si. In terms of the electrode potentials we found no influence of an increasing SiF_6^{2-} concentration that would require the adjustments of the etching parameters within 400 000 wafers for the PSI process and 2500 wafers for the MacPSI process. Therefore, an impact of SiF_6^{2-} on the etch performance is not expected.

Outlook concerning the electrochemical reactions

A deeper understanding for the electrochemical reactions concerning the PSI process is desirable. At the moment, the lack of a reference electrode prohibits these experiments. With an implemented reference electrode the available potentials for the electrochemical reactions could be identified more exactly. For example, it would be interesting to determine if the oxidation of ethanol is a competing reaction on the anode to the dissolution of Si. It would also be interesting to see whether CO_2 is detectable in the gas phase. Concerning the hydrogen formation it would be interesting to localize if hydrogen is released on the backside of the wafer, too. In addition, it would be interesting to determine the overall hydrogen release in more detail, i.e., the sum of the hydrogen released during the etching process from the Si surface and the hydrogen that forms during the reduction reaction of protons. A constant hydrogen release during the pore formation would indicate a superior reduction reaction, whereas a difference in the divalent and tetravalent dissolution should be noticeable if the amount of released hydrogen from the Si surface is reasonable.

8 REFERENCES

[1] Semi; PVgroup. *International Technology Roadmap for Photovoltaik (ITRPV), Results 2012*; 2013. Available online: www.itrpv.net.

[2] Brendel, R. Review of layer transfer processes for crystalline thin-film silicon solar cells. *Jpn. J. Appl. Phys.* **2001**, *40*, 4431–4439.

[3] Haase, F.; Winter, R.; Kajari-Schröder, S.; Nese, M.; Brendel, R. High efficiency back-contact back-junctions silicon solar cells with cell thicknesses of 45 µm, 90 µm, 130 µm and 290 µm. *Proceedings of the 27th European Photovoltaic Solar Energy Conference (EU PVSEC), Frankfurt, Germany* **2012**.

[4] Petermann, J.H.; Zielke, D.; Haase, F.; Garralaga Rojas, E.; Brendel, R. 19%-efficient and 43 µm-thick crystalline Si solar cell from layer transfer using porous silicon. *Prog. Photovolt: Res. Appl.* **2012**, *20*, 1–5.

[5] Steckenreiter, V.; Horbelt, R.; Nilsen Wright, D.; Nese, M. Qualification of encapsulation materials for module-level-processing. *Sol. Energy Mater. Sol. Cells* **2014**, *120*, 396–401.

[6] Green, M.A.; Emery, K.; Hishikawa, Y.; Warta, W.; Dunlop, E.D. Solar cell efficiency tables (version 41). *Prog. Photovolt: Res. Appl.* **2013**, *21*, 1–11.

[7] Ernst, M.; Brendel, R. Large area macroporous silicon layers for monocrystalline thin-film solar cells. *IEEE Proceedings of the 35th Photovoltaic Specialists Conference (PVSC), Honolulu, Hawaii* **2010**, 3122–3124.

[8] Ernst, M.; Brendel, R.; Ferre, R.; Harder, N.-P.; Kajari-Schröder, S. Macroporous silicon as an absorber for thin heterojunction solar cells. *IEEE Proceedings of the 38th Photovoltaic Specialists Conference (PVSC), Austin, Texas* **2012**, 1040–1045. © [2012] IEEE. Reprinted, with permission, from [8].

[9] Ernst, M.; Brendel, R.; Ferré, R.; Harder, N.-P. Thin macroporous silicon heterojunction solar cells. *Phys. Status Solidi RRL* **2012**, *6*, 187–189.

[10] Ernst, M.; Brendel, R. Macroporous silicon solar cells with an epitaxial emitter. *IEEE J. Photovolt.* **2013**, *3*, 723–729.

[11] Brendel, R. A novel process for ultrathin monocrystalline silicon solar cells on glass. *Proceedings of the 14th European Photovoltaic Solar Energy Conference (EU PVSEC), Barcelona, Spain* **1997**, 1354–1357.

[12] Tayanaka, H.; Matsushita, T. Separation of thin epitaxial Si films on porous Si for solar cells. *Proceedings of the 6th Sony Reseach Forum* **1996**, 556.

[13] Tayanaka, H.; Yamauchi, K.; Matsushita, T. Thin-film crystalline silicon solar cells obtained by separation of a porous silicon sacrificial layer. *Proceedings of the 2nd World Conference and Exhibition on Photovoltaic Solar Energy Conversion (WCPEC), Vienna, Austria* **1998**, 1272–1277.

[14] Haase, F. *Loss analysis of back-contact back-junction thin-film monocrystalline silicon solar cells*. Dissertation: Hannover, 2013.

[15] Steckenreiter, V.; Hensen, J.; Knorr, A.; Garralaga Rojas, E.; Kajari-Schröder, S.; Brendel, R. Reconditioning of silicon substrates for manifold re-use in the layer transfer process with porous silicon. *Proceedings of the 22nd International PV Science and Engineering Conference, Hangzhou, China* **2012**.

[16] Weinreich, W.; Acker, J.; Gräber, I. Determination of total fluoride in $HF/HNO_3/H_2SiF_6$ etch solutions by new potentiometric titration methods. *Talanta* **2007**, *71*, 1901–1905.

[17] Henßge, A.; Acker, J.; Müller, C. Titrimetric determination of silicon dissolved in concentrated HF-HNO_3-etching solutions. *Talanta* **2006**, *68*, 581–585.

[18] Henßge, A.; Acker, J. Chemical analysis of acidic silicon etch solutions I. Titrimetric determination of HNO_3, HF, and H_2SiF_6. *Talanta* **2007**, *73*, 220–226.

[19] Acker, J.; Henßge, A. Chemical analysis of acidic silicon etch solutions II. Determination of HNO_3, HF, and H_2SiF_6 by ion chromatography. *Talanta* **2007**, *72*, 1540–1545.

[20] Zimmer, M.; Oltersdorf, A.; Meded, M.; Kirchgässner, E.; Furtwängler, H.; Eigner, S.; Rentsch, J. In-line analysis and process control in wet chemical texturing processes. *Proceedings of the 22nd European Photovoltaic Solar Energy Conference (EU PVSEC), Milan, Italy* **2007**, 1020–1023.

[21] Zimmer, M.; Oltersdorf, A.; Kirchgässner, E.; Rentsch, J. Spectroscopical inline analysis of wet chemical processes. *Proceedings of the 23rd European Photovoltaic Solar Energy Conference (EU PVSEC), Valencia, Spain* **2008**, 1057–1061.

[22] Zimmer, M.; Oltersdorf, A.; Rentsch, J. Online process control of acidic texturisation baths with ion chromatography. *Talanta* **2009**, *80*, 499–503.

[23] Campbell, P.; Green, M.A. Light trapping properties of pyramidally textured surfaces. *J. Appl. Phys.* **1987**, *62*, 243–249.

[24] Macdonald, D.H.; Cuevas, A.; Kerr, M.J.; Samundsett, C.; Ruby, D.; Winderbaum, S.; Leo, A. Texturing industrial multicrystalline silicon solar cells. *Sol. Energy* **2004**, *76*, 277–283.

[25] Lauinger, T.; Schmidt, J.; Aberle, A.G.; Hezel, R. Record low surface recombination velocities on 1 Ω cm *p*-silicon using remote plasma silicon nitride passivation. *Appl. Phys. Lett.* **1996**, *68*, 1232–1234.

[26] Schultz, O.; Emanuel, G.; Glunz, S.W.; Willeke, G.P. Texturing of multicrystalline silicon with acidic wet chemical etching and plasma etching. *Proceedings of the 3rd World Conference and Exhibition on Photovoltaic Solar Energy Conversion (WCPEC), Osaka, Japan* **2003**, 1360–1363.

[27] Marstein, E.S.; Solhelm, H.J.; Nilsen Wright, D.; Holt, A. Acidic texturing of multicrystalline silicon wafers. *IEEE Proceedings of the 31st Photovoltaic Specialists Conference (PVSC), Florida* **2005**, 1309–1312.

[28] Hezel, R. A new high efficiency solar cell concept based on truncated pyramids. *Proceedings of the 1st World Conference and Exhibition on Photovoltaic Solar Energy Conversion (WCPEC), Hawaii, USA* **1994**.

[29] Grauvogl, M.; Aberle, A.G.; Hezel, R. 17.1% efficient metal-insulator-semiconductor inversion layer silicon solar cells using truncated pyramids. *Appl. Phys. Lett.* **1996**, *69*, 1462–1464. Reprinted with permission from [29]. Copyright [1996], AIP Publishing LLC.

[30] Grauvogl, M.; Hezel, R. The truncated-pyramid MIS inversion-layer solar cell: a comprehensive analysis. *Prog. Photovolt: Res. Appl.* **1998**, *6*, 15–24.

[31] Metz, A.; Meyer, R.; Kuhlmann, B.; Grauvogl, M.; Hezel, R. 18.5% efficient first-generation MIS inversion-layer silicon solar cells. *IEEE Proceedings of the 26th Photovoltaic Specialists Conference (PVSC), Anaheim, CA* **1997**, 31–34.

[32] Müller, J.W.; Metz, A.; Hezel, R. A new and simple approach for fabricating inverted pyramids on crystalline silicon solar cells. *Proceedings of the 17th European Photovoltaic Solar Energy Conference (EU PVSEC), Munich, Germany* **2001**, 347–349.

[33] Steinert, M.; Acker, J.; Henßge, A.; Wetzig, K. Experimental studies on the mechanism of wet chemical etching of Si in HF/HNO_3 mixtures. *J. Electrochem. Soc.* **2005**, *152*, C843-C850.

[34] Steinert, M.; Acker, J.; Krause, M.; Oswald, S.; Wetzig, K. Reactive species generated during wet chemical etching of silicon in HF/HNO_3 mixtures. *J. Phys. Chem. B* **2006**, *110*, 11377–11382.

[35] Kolasinski, K.W.; Yadlovskiy, J. Stain etching of silicon with V_2O_5. *phys. stat. sol. (c)* **2011**, *8*, 1749–1753.

[36] Dudley, M.E.; Kolasinski, K.W. Stain etching with Fe(III), V(V), and Ce(IV) to form microporous silicon. *Electrochem. Solid St.* **2009**, *12*, D22-D26.

[37] Nahidi, M.; Kolasinski, K.W. Effects of stain etchant composition on the photoluminescence and morphology of porous silicon. *J. Electrochem. Soc.* **2006**, *153*, C19-C26.

[38] Kochergin, V.; Föll, H. *Porous Semiconductors - Optical Properties and Applications*; Springer: London, 2009.

[39] Lehmann, V. *Electrochemistry of Silicon*; WILEY-VCH Verlag GmbH & Co. KGaA: Weinheim, 2002.

[40] Kolasinski, K.W. Etching of silicon in fluoride solutions. *Surf. Sci.* **2009**, *603*, 1904–1911.

[41] Turner, D.R. Electropolishing silicon in hydrofluoric acid solutions. *J. Electrochem. Soc.* **1958**, *105*, 402–408.

[42] Uhlir, A. Electrolytic shaping of germanium and silicon. *Bell System Tech. J.* **1956**, *35*.

[43] Foucaran, A.; Pascal-Delannoy, F.; Giani, A.; Sackda, A.; Combette, P.; Boyer, A. Porous silicon layers used for gas sensor applications. *Thin Solid Films* **1997**, *297*, 317–320.

[44] Anglin, E.J.; Cheng, L.; Freeman, W.R.; Sailor, M.J. Porous silicon in drug delivery devices and materials. *Adv. Drug Delivery Rev.* **2008**, *60*, 1266–1277.

[45] Clément, D.; Diener, J.; Gross, E.; Künzner, N.; Timoshenko, V.Y.; Kovalev, D. Highly explosive nanosilicon-based composite materials. *phys. stat. sol. (a)* **2005**, *202*, 1357–1364.

[46] Shabir, Q.; Skaria, C.; O Brien, H.; Loni, A.; Barnett, C.; Canham, L. Taste and mouthfeel assessment of porous and non-porous silicon microparticles. *Nanoscale Res. Lett.* **2012**, *7*, 407.

[47] Sing, K.S.W.; Everett, D.H.; Haul, R.A.W.; Moscou, L.; Pierotti, R.A.; Rouquérol, J.; Siemieniewska, T. Reporting physisorption data for gas/solid systems: with special reference to the determination of surface area and porosity. *Pure & Appl. Chem.* **1985**, *57*, 603–619.

[48] Herino, R.; Bomchil, G.; Barla, K.; Bertrand, C. Porosity and pore size distribution of porous silicon layers. *J. Electrochem. Soc.* **1987**, *134*, 1994–2000.

[49] Birner, A. *Optische Wellenleiter und Mikroresonatoren in zweidimensionalen photonischen Kristallen aus makroporösem Silizium*. Dissertation: Halle-Wittenberg, 2000.

[50] Wolf, A.; Terheiden, B.; Brendel, R. Autodiffusion: A Novel Method for Emitter Formation in Crystalline Silicon Thin-Film Solar Cells. *Prog. Photovolt: Res. Appl.* **2007**, *15*, 199–210.

[51] Wolf, A. *Sintered porous silicon - Physical properties and applications for layer-transfer silicon thin-film solar cells*. Dissertation: Hannover, 2007.

[52] Lehmann, V.; Gösele, U. Porous silicon formation: A quantum wire effect. *Applied Physics Letters* **1991**, *58*, 856–858.

[53] Memming, R.; Schwandt, G. Anodic dissolution of silicon in hydrofluoric acid solutions. *Surf. Sci.* **1966**, *4*, 109–124.

[54] Ernst, M. *Oberflächenpassivierung und Schichttransfer makroporösen Siliciums*. Diploma Thesis: Hannover, 2008.

[55] Niwano, M.; Miura, T.; Kimura, Y.; Tajima, R.; Miyamoto, N. Real-time, *in situ* infrared study of etching of Si(100) and (111) surfaces in dilute hydrofluoric acid solution. *J. Appl. Phys.* **1996**, *79*, 3708–3713.

[56] Niwano, M.; Miura, T.; Tajima, R.; Miyamoto, N. Infrared study of chemistry of Si surfaces in etching solutions. *Appl. Surf. Sci.* **1996**, *100/101*, 607–611.

[57] Niwano, M.; Kimura, Y.; Miyamoto, N. *In situ* infrared study of chemical state of Si surface in etching solution. *Appl. Phys. Lett.* **1994**, *65*, 1692–1694.

[58] Atkins, P.W. *Physikalische Chemie*, 3rd ed; WILEY-VCH Verlag GmbH & Co. KGaA: Weinheim, 2001.

[59] Bard, A.J.; Parsons, R.; Jordan, J. *Standard Potentials in Aqueous Solution*; Marcel Dekker, Inc.: New York, 1985.

[60] Binnewies, M.; Jäckel, M.; Willner, H.; Rayner-Canham, G. *Allgemeine und Anorganische Chemie*, 1st ed; Spektrum Akademischer Verlag: München, 2004.

[61] Ernst, M. *Macroporous silicon for crystalline thin-film solar cells*. Disseration: Hannover, 2013.

[62] Radhakrishnan, H.S.; Martini, R.; Depauw, V.; van Nieuwenhuysen, K.; Debucqroy, M.; Govaerts, J.; Gordon, I.; Mertens, R.; Poortmans, J. Improving the quality of epitaxial foils produced using a porous silicon-based layer transfer process for high efficiency thin-film crystalline silicon solar cells. *IEEE J. Photovolt.* **2014**, *4*, 70–77.

[63] Smith, R.L.; Collins, S.D. Porous silicon formation mechanisms. *J. Appl. Phys.* **1992**, *71*, R1-R22.

[64] Binnewies, M. *Chemische Gleichgewichte*; VCH Verlagsgesellschaft: Weinheim, 1996.

[65] Verhaverbeke, S.; Teerlinck, I.; Vinckier, C.; Stevens, G.; Cartuyvels, R.; Heyns, M.M. The etching mechanism of SiO_2 in hydrofluoric acid. *J. Electrochem. Soc.* **1994**, *141*, 2852–2857. Reproduced by permission of The Electrochemical Society.

[66] Kolasinski, K.W. The mechanism of Si etching in fluoride solutions. *Phys. Chem. Chem. Phys.* **2003**, *5*, 1270–1278.

[67] Broene, H.H.; De Vries, T. The thermodynamics of aqueous hydrofluoric acid solutions. *J. Am. Chem. Soc.* **1947**, *69*, 1644–1646.

[68] Warren, L.J. The measurement of pH in acid fluoride solutions and evidence for the existence of $(HF)_2$. *Anal. Chim. Acta* **1971**, *53*, 199–202.

[69] Kordás, K.; Remes, J.; Beke, S.; Hu, T.; Leppävuori, S. Manufacturing of porous silicon; porosity and thickness dependence on electrolyte composition. *Appl. Surf. Sci.* **2001**, *178*, 190–193.

[70] Bomchil, G.; Herino, R.; Barla, K.; Pfister, J.C. Pore size distribution in porous silicon studied by adsorption isotherms. *J. Electrochem. Soc.* **1983**, *130*, 1611–1614.

[71] Lehmann, V. Porous silicon preparation: Alchemy or electrochemistry? *Adv. Mater.* **1992**, *11*, 762–764.

[72] Luxenberg, P.; Kim, J.I. Hydrogenfluorid-Gleichgewichte in Äthanol-Wasser-Mischungen. *Z. Phys. Chem.* **1980**, *121*, 173–186.

[73] Garrido, B.; Montserrat, J.; Morante, J.R. The role of chemical species in the passivation of <100> silicon surfaces by HF in water-ethanol solutions. *J. Electrochem. Soc.* **1996**, *143*, 4059–4066.

[74] Chainet, F.; Lienemann, C.-P.; Coutiade, M.; Ponthus, J.; Donard, O.F. Silicon speciation by hypenated techniques for environmental, biological and industrial issues: A review. *J. Anal. At. Spectrom.* **2011**, *26*, 30–51.

[75] Judge, J.S. A study of the dissolution of SiO_2 in acidic fluoride solutions. *J. Electrochem. Soc.* **1971**, *118*, 1772–1775.

[76] Lingane, J.J. Further study of the lanthanum fluoride membrane electrode for potentiometric determination and titration of fluoride. *Anal. Chem.* **1968**, *40*, 935–939.

[77] Moeller, T.; Kremers, H.E. Observations on the rare earths: An electrometric study of the precipitation of trivalent hydrous rare earth oxides and hydroxides. *J. Phys. Chem.* **1944**, *48*, 395–406.

[78] Nehmann, J.B.; Kajari-Schröder, S.; Bahnemann, D.W. Analysis methods for meso- and macroporous silicon etching baths. *Nanoscale Res. Lett.* **2012**, *7*, 398.

[79] Frant, M.S.; Ross, J.W. Electrode for sensing fluoride ion activity in solution. *Science* **1966**, *154*, 1553–1555.

[80] Lingane, J.J. A study of the lanthanum fluoride membrane electrode for end point detection in titrations of fluoride with thorium, lanthanum, and calcium. *Anal. Chem.* **1967**, *39*, 881–887.

[81] Sawant, R.M.; Mahajan, M.A.; Verma, P.; Shah, D.; Thakur, U.K.; Ramakumar, K.L.; Venugopal, V. Fluoride determination in various matrices relevant to nuclear industry: A review. *Radiochim. Acta* **2007**, *95*, 585–594.

[82] Pütz, P. *TOC - ein aufschlussreicher Summenparameter*, *Praxisbericht*; 2009. Available online: www.hach-lange.de.

[83] Byrne, R.H. Standardization of standard buffers by visible spectrometry. *Anal. Chem.* **1987**, *59*, 1479–1481. Reprinted with permission from [83]. Copyright (1987) American Chemical Society.

[84] Weiß, J. *Handbook of Ion Chromatography*, 3rd ed; WILEY-VCH Verlag GmbH & Co. KGaA: Weinheim, 2004.

[85] Schwedt, G.; Vogt, C. *Analytische Trennmethoden*; WILEY-VCH Verlag GmbH & Co. KGaA: Weinheim, 2010. Copyright Wiley-VCH Verlag GmbH & Co. KGaA. Reproduced with permission.

[86] Pettersson, A.K.; Karlberg, B. Simultaneous determination of orthophosphate and silicate in brackish water. *Anal. Chim. Acta* **1999**, *378*, 183–189.

[87] Knudson; H. W.; Juday, C.; Meloche, V.W. Silicomolybdate method for silica. *Ind. Eng. Chem., Anal. Ed.* **1940**, *12*, 270–273.

[88] Cordes, P. *Streng biomimetische Modellsysteme für die Biomineralisation von Siliciumdioxid auf der Basis von Polyaminen oder Alkylglycosiden*. Dissertation: Hannover, 2006.

[89] Alexander, G.B. The reaction of low molecular weight silicic acid with molybdic acid. *J. Am. Chem. Soc.* **1953**, *75*, 5655–5657.

[90] Lange, B.; Vejdělek, Z.J. *Photometrische Analyse*; Verlag Chemie GmbH: Weinheim, 1987.

[91] Römpp Online; 2014. Available online: www.roempp.com.

[92] Jarry, R.L.; Davis, W., JR. The vapor pressure, association, and heat of vaporization of hydrogen fluoride. *J. Phys. Chem.* **1953**, *57*, 600–604.

[93] Lide, D.R. *CRC Handbook of Chemistry and Physics*: *A Ready-Reference Book of Chemical and Physical Data*, 82nd ed; CRC Press: Washington D.C., 2001.

[94] *Concentration Density Finder*; Merck Millipore, 2014.

[95] Rausch, R. *Das Periodensystem der Elemente online*, *Dichtewertetabelle von Flusssäure*; 2014. Available online: www.periodensystem-online.de/index.php?id=lists&form=Dichtewerte&sst=15 (accessed on 12 June, 2014).

[96] Holleman, A.F.; Wiberg, E. *Lehrbuch der Anorganischen Chemie*, 91st ed; Walter de Gruyter: Berlin, 1985.

[97] Sears, F.W.; Zemansky, M.W. *University Physics*, 2nd ed; Addison-Wesley, 1955.

[98] Keller-Rudek, H.; Kuhn, P.; List, H.; Gmelin, L.; Koschel, D., Eds. *Gmelin Handbook of Inorganic Chemistry. F-Fluorine. Supplement Vol 3: Compounds with Hydrogen*; Springer, 1982.

[99] Vázquez, G.; Alvarez, E.; Navaza, J.M. Surface tension of alcohol + water from 20 to 50 °C. *J. Chem. Eng. Data* **1995**, *40*, 611–614.

[100] Demtröder, W. *Experimentalphysik 1*: *Wärme und Mechanik*, 3rd ed; Springer: Heidelberg, 2004.

[101] Honeywell. *Specialty Chemicals*, *Hydrofluoric Acid Properties*; 2002. Available online: http://www.chem.purdue.edu/chemsafety/Equip/HFfacts10.pdf (accessed on 12 June, 2014).

[102] *Internal communication at ISFH*.

[103] Mitrovic, J. Das Abreissen von Dampfblasen an festen Heizflächen. *Int. J. Heat Mass Transfer* **1983**, *26*, 955–963.

[104] Meyer, R.J.; Pietsch, E., Eds. *Gmelins Handbuch der Anorganischen Chemie*: *Wasserstoff*, 8th ed; Verlag Chemie GmbH: Berlin, 1927.

[105] Crozier, T.E.; Yamamoto, S. Solubility of hydrogen in water, seawater, and NaCl solutions. *J. Chem. Eng. Data* **1974**, *19*, 242–244.

[106] Grathwohl, P. *Diffusion in Natural Porous Media*: *Contaminant Transport, Sorption/Desorption and Dissolution Kinetics*; Springer, 1998.

[107] Kato, Y.; Ito, T.; Hiraki, A. Low temperature oxidation of crystalline porous silicon. *Appl. Surf. Sci.* **1989**, *41/42*, 614–618.

[108] Ito, T.; Yasumatsu, T.; Watabe, H.; Hiraki, A. Structural change of crystalline porous silicon with chemisorption. *Jpn. J. Appl. Phys.* **1990**, *29*, L201-L204.

[109] Morita, M.; Ohmi, T.; Hasegawa, E.; Kawakami, M.; Ohwada, M. Growth of native oxide on a silicon surface. *J. Appl. Phys.* **1990**, *68*, 1272–1281.

[110] Miura, T.; Niwano, M.; Shoji, D.; Miyamoto, N. Initial stages of oxidation of hydrogen-terminated Si surfaces stored in air. *Appl. Surf. Sci.* **1996**, *100/101*, 454–459.

[111] Miura, T.; Niwano, M.; Shoji, D.; Miyamoto, N. Kinetics of oxidation on hydrogen-terminated Si(100) and (111) surfaces stored in air. *J. Appl. Phys.* **1996**, *79*, 4373–4380.

[112] Gmelin, L.; Meyer, R.J., Eds. *Gmelins Handbook of Inorganic and Organometallic Chemistry*: *Silicium Teil B, System Nr. 15*; Verlag Chemie GmbH: Weinheim, 1959.

[113] Urbansky, E.T. Fate of fluorosilicate drinking water additives. *Chem. Rev.* **2002**, *102*, 2837–2854.

[114] Sugita, Y.; Watanabe, S. Effects of reaction product during hydrogenation of Si surfaces in HF solution. *Jpn. J. Appl. Phys.* **1998**, *37*, 1193–1197.

[115] Behrendt, W.; Gmelin, L., Eds. *Gmelin Handbook of Inorganic and Organometallic Chemistry*: *Si Supplement Vol. B8*. Ternary Silicon-Fluorine-Hydrogen Compounds; Springer: London, 1996.

[116] Monk, D.J.; Soane, D.S.; Howe, R.T. Hydrofluoric acid etching of silicon dioxide sacrificial layers. *J. Electrochem. Soc.* **1994**, *141*, 264–269.

[117] Hickling, A.; Higgins, J.K. The rate-determining stage in the anodic dissolution of metals. *Trans. Inst. Met. Finishing* **1953**, *29*, 274–291.

[118] Weinreich, W.; Acker, J.; Gräber, I. The effect of H_2SiF_6 on the surface morphology of textured multi-crystalline silicon. *Semicond. Sci. Technol.* **2006**, *21*, 1278–1286.

[119] Unagami, T. Formation mechanism of porous silicon layer by anodization in HF solution. *J. Electrochem. Soc.* **1980**, *127*, 476–483.

[120] Hengge, E.; Schlöl, R., Eds. *Gmelin Handbook of Inorganic and Organometallic Chemistry*: *Si Supplement Volume B7*. Binary species of silicon and fluorine; Springer: Berlin, 1992.

[121] Zachmann, H.G. *Mathematik für Chemiker*, 5th ed; WILEY-VCH Verlag GmbH & Co. KGaA: Weinheim, 2004.

9 LIST OF FIGURES

10 APPENDIX

A DETERMINATION OF THE VALENCE

The valence *n* is defined as the number of electrons required for the dissolution of a single Si atom, as discussed in chapter 2.2.2 on page 11. In the following, the valence for the starting and the separation layer of the PSI process is determined to investigate the dissolution behavior. The parameters of the layers are given in Table A1; the constants are listed in the list of symbols in chapter 9. The etching area *A* is 145 cm^2.

Table A1: Parameters for and results of the calculation of the valence *n* for the starting and the separation layer of the PSI process.

	Starting Layer	Separation Layer
Thickness *d* [µm]	1.1	0.2
Porosity *P* [%]	22	40
Volume of porous Si V_{PSI} [cm^3]	$3.509 \cdot 10^{-3}$	$1.160 \cdot 10^{-3}$
Amount of substance n_{Si} [mol]	$2.919 \cdot 10^{-4}$	$9.648 \cdot 10^{-5}$
Number of dissolved Si atoms N_{Si}	$1.758 \cdot 10^{20}$	$5.810 \cdot 10^{19}$
Current density *J* [mA/cm^2]	5	200
Etching time *t* [s]	100	3
Electric charge *Q* [C]	72.5	87
Number of required electrons N_{e-}	$4.526 \cdot 10^{20}$	$5.431 \cdot 10^{20}$
Valence *n*	2.6	9.3

The calculation of the number of dissolved Si atoms N_{Si} is the first step in the determination of the valence

$$n_{Si} = V_{PSI} \cdot \frac{\rho_{Si}}{M_{Si}} = (A \cdot d \cdot P) \cdot \frac{\rho_{Si}}{M_{Si}}$$

$$N_{Si} = N_A \cdot n_{Si}$$

where M_{Si} is the molar mass of Si, ρ_{Si} is the density of Si, and N_A is Avogadro's constant. As a result, N_{Si} is $1.758 \cdot 10^{20}$ for the starting and $5.810 \cdot 10^{19}$ for the separation layer of the PSI process. The number of available electrons N_{e-} is determined as follows

$$N_{e^-} = \frac{(J \cdot A) \cdot 10^{-3} \cdot t}{e} = \frac{Q}{e}$$

where e is the elementary charge. For the starting layer, N_{e-} is $4.526 \cdot 10^{20}$ and for the separation layer N_{e-} is $5.431 \cdot 10^{20}$. Hence, the valence n is defined as the ratio of N_{e-} and N_{Si}

$$n = \frac{N_{e^-}}{N_{Si}}$$

Finally, the valence is 2.6 for the starting layer and 9.3 for the separation layer in the PSI process.

Uncertainty of the valence n

The following paragraph shows the determination of the valences uncertainty in order to estimate the reliability of the result. The calculation is performed according to [121] and takes into consideration the uncertainties of the input parameters.

We considered the etching area A, the density of Si ρ_{Si}, the molar mass of Si M_{Si}, Avogadro's constant N_A, and the electronic charge e as constants. Table A2 lists the uncertainties as estimated for the input parameters.

Table A2: Uncertainties of the input parameters for the calculation of the valence *n* in the PSI process.

	Starting Layer	Separation Layer
Thickness *d* [µm]	1.1 ± 0.01	0.2 ± 0.01
Porosity *P* [%]	22 ± 2	40 ± 2
Current density *J* [mA/cm^2]	5 ± 0.1	200 ± 0.1
Etching time *t* [s]	100 ± 0.1	3 ± 0.1

The uncertainty of the amount of substance n_{Si} was calculated according to

$$m_{n,Si} = \sqrt{\left(\frac{\partial n_{Si}}{\partial d}\right)^2 m_d^2 + \left(\frac{\partial n_{Si}}{\partial P}\right)^2 m_P^2}$$

$$= \sqrt{\left(AP\frac{\rho_{Si}}{M_{Si}}\right)^2 m_d^2 + \left(dA\frac{\rho_{Si}}{M_{Si}}\right)^2 m_P^2}$$

and was required for the determination of the uncertainty of the number of dissolved Si atoms N_{Si}.

$$m_{N,Si} = \sqrt{\left(\frac{\partial N_{Si}}{\partial n_{Si}}\right)^2 m_{n,Si}^2}$$

$$= \sqrt{N_A^2\ m_{n,Si}^2}$$

Besides, the uncertainty of the number of required electrons N_{e-} was calculated according to the following equations.

$$m_{n,e} = \sqrt{\left(\frac{\partial n_e}{\partial J}\right)^2 m_J^2 + \left(\frac{\partial n_e}{\partial t}\right)^2 m_t^2}$$

$$= \sqrt{\left(\frac{At}{e}\right)^2 m_J^2 + \left(\frac{JA}{e}\right)^2 m_t^2}$$

Finally, the uncertainty of the valence n equates to:

$$m_n = \sqrt{\left(\frac{\partial n}{\partial N_e}\right)^2 m_{N,e}^2 + \left(\frac{\partial n}{\partial N_{Si}}\right)^2 m_{N,Si}^2}$$

$$= \sqrt{\left(\frac{1}{N_{Si}}\right)^2 m_{N,e}^2 + \left(-\frac{N_e}{N_{Si}^2}\right)^2 m_{N,Si}^2}$$

Table A3 lists the results of the determination of the uncertainty for the valence.

Table A3: Intermediate results for the uncertainties of the valence *n* in the PSI process.

	Starting Layer	Separation Layer
Number of dissolved Si atoms N_{Si}	$(2.1 \pm 0.3)\cdot 10^{20}$	$(7.0 \pm 3.5)\cdot 10^{19}$
Number of required electrons N_{e-}	$(5.5 \pm 0.1)\cdot 10^{20}$	$(6.6 \pm 0.2)\cdot 10^{20}$
Valence n	2.6 ± 0.4	9.3 ± 4.7

Consequently, the valence for the starting layer in the PSI process is $n = 2.6 \pm 0.4$ and for the separation layer $n = 9.3 \pm 4.7$. The uncertainty of the separation layer is mainly due to the uncertainty in the thickness of the layer and its porosity.

B DETERMINATION OF THE MEASUREMENT UNCERTAINTIES

The uncertainty of a measurement result consists of the systematic and the relative uncertainty. The systematic uncertainty considers the uncertainty of pipettes, volumetric flasks, measuring cylinders, and standard solutions. Those contribute to the uncertainty of the sample preparation as well as to the measurement itself. Therefore, the uncertainties m_{Dilute} and $m_{Measure}$ were calculated by error-propagation in order to obtain the mean uncertainty of the measurement result taking into consideration the uncertainties of the input parameters [121]. The relative uncertainty is represented by the standard deviation $m_{Standard\ dev}$.

We assume that the performance of the investigated method is not affected by former measurements.

TITRATION

The uncertainty of the fluoride concentration determined by precipitation titration $m_{Titration}$ consists of the systematic uncertainty of the measurement $m_{F-,Measure}$ and the standard deviation $m_{Standard\ dev}$.

$$m_{\text{Titration}} = m_{\text{F}^-,\text{Measure}} + m_{\text{Standard dev.}}$$

The uncertainty of the measurement $m_{F-,Measure}$ depends on various sources of errors, i.e., the volume of the etching bath sample V_{EB}, the volume V_{La} and the concentration *[La]* of the $La(NO_3)_3$ standard solution. Since *[La]* has a huge impact on the titration result as discussed in chapter 3.1.1 on page 27, the uncertainty $m_{[La]}$ was determined experimentally with a nitrate ion-selective electrode.

Nitrate ion-selective electrode

The uncertainty of the NO_3-ISE measurement $m_{NO3-ISE}$ consists of the systematic uncertainties in the sample preparation $m_{NO3-,Dilute}$, and in the measurement $m_{NO3-,Measure}$ as well as of the standard deviation $m_{Standard\ dev}$.

$$m_{\text{NO}_3-\text{ISE}} = m_{\text{NO}_3^-,\text{Dilute}} + m_{\text{NO}_3^-,\text{Measure}} + m_{\text{Standard dev.}}$$

The uncertainty of the sample preparation is determined taking the dilution of the $La(NO_3)_3$ solution sample into consideration; therefore, the uncertainty of the concentration of the diluted sample $m_{NO3-,Dilute}$ is determined in the following by error-propagation.

$$[NO_{3,St}^{-}]\,V_{St} = [NO_{3,Dilute}^{-}]\,V_{Dilute}$$

$$m_{[NO_3^-,Dilute]} = \sqrt{\left(\frac{\partial[NO_{3,Dilute}^{-}]}{\partial[NO_{3,St}^{-}]}\right)^2 m_{[NO_{3,St}^{-}]}^2 + \left(\frac{\partial[NO_{3,Dilute}^{-}]}{\partial V_{St}}\right)^2 m_{V_{St}}^2 + \left(\frac{\partial[NO_{3,Dilute}^{-}]}{\partial V_{Dilute}}\right)^2 m_{V_{Dilute}}^2}$$

$$= \sqrt{\left(\frac{V_{St}}{V_{Dilute}}\right)^2 m_{[NO_{3,St}^{-}]}^2 + \left(\frac{[NO_{3,St}^{-}]}{V_{Dilute}}\right)^2 m_{V_{St}}^2 + \left(-\frac{[NO_{3,St}^{-}]\,V_{St}}{(V_{Dilute})^2}\right)^2 m_{V_{Dilute}}^2}$$

Table B1 lists the required parameters. The uncertainty of the $La(NO_3)_3$ standard solution concentration $[NO_3^-]_{St}$ has been estimated to 5%.

Table B1: Parameters for the determination of the uncertainty of the NO_3-ISE.

Parameter	Typical value	Uncertainty
Standard solution concentration $[NO_3^-]_{St}$	0.1 mol/l	0.005 mol/l
Volume of standard sample V_{St}	0.25 ml	0.005 ml*
Volume of diluted sample V_{Dilute}	25 ml	0.04 ml*
Temperature T	298 K	5 K
Measured potential E	171	1 mV
Standard potential E_0	311 mV#	5 mV

* As reported by the manufacturer.
\# As taken from calibration data.

Accordingly, the uncertainty of the sample preparation $m_{NO3-,Dilute}$ is $5.4\cdot10^{-5}$ mol/l.

The concentration of the nitrate $[NO_3^-]$ is determined by the Nernst equation:

$$E = E^0 + \frac{RT}{zF}\ln a_{NO_3^-}$$

Here, the activity a_{NO3-} of the nitrate ions is set equal with their concentration $[NO_3^-]$ to facilitate the calculation. Therefore, a_{NO3-} is substituted by $[NO_3^-]$ in the following. Error-afflicted parameters considered for the determination of the measurement uncertainty of $[NO_{3-,Measure}]$ are T and E while R, z, F, and E^0 are constants.

$$[NO_3^-] = e^{\frac{(E-E^0)zF}{RT}}$$

$$m_{[NO_{3,Measure}^-]} = \sqrt{\left(\frac{\partial[NO_3^-]}{\partial E}\right)^2 m_E^2 + \left(\frac{\partial[NO_3^-]}{\partial T}\right)^2 m_T^2}$$

$$= \sqrt{\left(\left(\frac{nF}{RT}\right)e^{\frac{(E-E^0)zF}{RT}}\right)^2 m_E^2 + \left(\left(-\frac{(E-E^0)zF}{RT^2}\right)e^{\frac{(E-E^0)zF}{RT}}\right)^2 m_T^2}$$

Therefore, the uncertainty of the measurement for the NO_3-ISE is $6.0\cdot10^{-3}$ mol/l.

The standard deviation $m_{Standard\ dev}$ has been determined by 7-fold measurement and was found to be 0.018 mol/l. Therefore, the total uncertainty of the NO_3-ISE measurement $m_{NO3\text{-}ISE}$ is 0.02 mol/l or 20%, respectively, regarding the initial concentration as given in Table B1.

Now we use $m_{NO3\text{-}ISE}$ for the determination of $m_{Titration}$. The uncertainty of the $La(NO_3)_3$ solution concentration is required for the determination of the uncertainty of the amount of substance of $La(NO_3)_3$ solution n_{La}. The relevant parameters are listed in Table B2.

Table B2: Parameters for the determination of the uncertainty of the precipitation titration.

Parameter	Typical value	Uncertainty
Volume of $La(NO_3)_3$ solution in burette V_{La}	10 ml	0.001 ml*
Experimental concentration of $La(NO_3)_3$ $[La]$	0.096 mol/l	0.02 mol/l
Volume of etching bath sample V_{EB}	0.15 ml	0.005 ml*

* As reported by the manufacturer.

$$n_{La} = [La]\cdot V_{La}$$

$$m_{n,La} = \sqrt{\left(\frac{\partial n_{La}}{\partial V_{La}}\right)^2 m_{V,La}^2 + \left(\frac{\partial n_{La}}{\partial [La]}\right)^2 m_{[La]}^2}$$

$$= \sqrt{([La])^2 m_{V,La}^2 + (V_{La})^2 m_{[La]}^2}$$

The uncertainty of n_{La} is in the range of $2\cdot10^{-4}$ mol/l. With this, the determination of the uncertainty of the amount of substance of fluoride n_F is possible – it is found to be in the range of $6\cdot10^{-4}$ mol/l.

$n_F = 3\cdot n_{La}$ according to $La^{3+}{}_{(aq)} + 3\ F^-{}_{(aq)} \rightarrow LaF_{3\ (s)}$

$$m_{n,F} = \sqrt{\left(\frac{\partial n_F}{\partial n_{La}}\right)^2 m_{n,La}^2}$$

$$= \sqrt{3^2 \cdot m_{n,La}^2}$$

Finally, the uncertainty of the measured fluoride concentration $m_{[F^-]}$ is calculated according to:

$$[F^-] = \frac{n_F}{V_{EB}}$$

$$m_{[F^-]} = \sqrt{\left(\frac{\partial [F^-]}{\partial n_F}\right)^2 m_{n_F}^2 + \left(\frac{\partial [F^-]}{\partial V_{EB}}\right)^2 m_{V_{EB}}^2}$$

$$= \sqrt{\left(\frac{1}{V_{EB}}\right)^2 m_{n_F}^2 + \left(-\frac{n_F}{V_{EB}^2}\right)^2 m_{V_{EB}}^2}$$

Following the calculations, $m_{[F^-]}$ is in the range of 4.0 mol/l depending on the concentration of the etching bath ranging from about 15 to 19.5 mol/l. The standard deviation $m_{Standard\ dev}$ of the precipitation titration has been determined by a 20-fold measurement to 0.08 mol/l. Therefore, $m_{Titration}$ of this work results in 4.1 mol/l or 21%, respectively, regarding the fluoride concentration of 19.5 mol/l.

Note: The uncertainty of $m_{Titration}$ calculated so far is relatively high and mainly caused by the uncertainty of the $La(NO_3)_3$ standard solution. Assuming the concentration of the standard solution to be accurate, the uncertainty of $m_{Titration}$ reduces to 0.3 mol/l ($m_{[F^-]}$ = 0.22 mol/l and $m_{Standard\ dev}$ = 0.08 mol/l), which is 1.5% with regard to the initial fluoride concentration of 19.5 mol/l. The figures in chapter 4 are drawn with this uncertainty.

FLUORIDE ION-SELECTIVE ELECTRODE

The uncertainty of the F-ISE measurement $m_{F\text{-}ISE}$ consists of the systematic uncertainties in the sample preparation $m_{F^-,Dilute}$, and in the measurement $m_{F^-,Measure}$ as well as of the standard deviation $m_{Standard\ dev}$.

$$m_{F-ISE} = m_{F^-,Dilute} + m_{F^-,Measure} + m_{Standard\ dev.}$$

The uncertainty of the sample preparation is determined taking the dilution of the etching bath sample into consideration; therefore, the uncertainty of the concentration of the diluted sample $m_{F^-,Dilute}$ is determined in the following. Table B3 lists the required parameters. The uncertainty of the etching bath concentration $[F^-_{EB}]$ has been estimated to 5%.

Table B3: Parameters for the determination of the uncertainty of the F-ISE.

Parameter	Typical value	Uncertainty
Measured potential E	-40 mV	1 mV
Standard potential E_0	76 mV[#]	5 mV
Volume of diluted sample V_{Dilute}	1000 ml	0.08 ml*
Temperature T	298 K	5 K
PSI etching bath		
Etching bath concentration $[F^-_{EB}]_{PSI}$	19.5 mol/l	0.98 mol/l
Volume of etching bath sample $V_{EB,PSI}$	0.3 ml	0.005 ml*
MacPSI etching bath		
Etching bath concentration $[F^-_{EB}]_{MacPSI}$	1.43 mol/l	0.07 mol/l
Volume of etching bath sample $V_{EB,MacPSI}$	3.5 ml	0.03 ml*

* As reported by the manufacturer.
[#] As taken from calibration data.

$$[F^-_{EB}]\,V_{EB} = [F^-_{Dilute}]\,V_{Dilute}$$

$$m_{[F^-_{Dilute}]} = \sqrt{\left(\frac{\partial[F^-_{Dilute}]}{\partial[F^-_{EB}]}\right)^2 m^2_{[F^-_{EB}]} + \left(\frac{\partial[F^-_{Dilute}]}{\partial V_{EB}}\right)^2 m^2_{V_{EB}} + \left(\frac{\partial[F^-_{Dilute}]}{\partial V_{Dilute}}\right)^2 m^2_{V_{Dilute}}}$$

$$= \sqrt{\left(\frac{V_{EB}}{V_{Dilute}}\right)^2 m^2_{[F^-_{EB}]} + \left(\frac{[F^-_{EB}]}{V_{Dilute}}\right)^2 m^2_{V_{EB}} + \left(-\frac{[F^-_{EB}]\,V_{EB}}{(V_{Dilute})^2}\right)^2 m^2_{V_{Dilute}}}$$

The concentration of the fluoride $[F^-]$ is determined by the Nernst equation:

$$E = E^0 + \frac{RT}{zF}\ln a$$

Here, the activity a of the fluoride ions equals $[F^-]$ due to the experimental setup as described in chapter 3.1.2 on page 29. Therefore, a is substituted by $[F^-]$ in the following. Error-afflicted parameters for the determination of the measurement uncertainty $[F^-_{Measure}]$ are T and E while R, z, F, and E^0 are constants.

$$[F^-] = e^{\frac{(E-E^0)zF}{RT}}$$

$$m_{[F^-_{Measure}]} = \sqrt{\left(\frac{\partial[F^-]}{\partial E}\right)^2 m_E^2 + \left(\frac{\partial[F^-]}{\partial T}\right)^2 m_T^2}$$

$$= \sqrt{\left(\left(\frac{zF}{RT}\right)e^{\frac{(E-E^0)zF}{RT}}\right)^2 m_E^2 + \left(\left(-\frac{(E-E^0)zF}{RT^2}\right)e^{\frac{(E-E^0)zF}{RT}}\right)^2 m_T^2}$$

The uncertainty of the measurement $m_{F\text{-},Measure}$ calculates to 0.04 mol/l for both etching baths.

For the PSI etching bath, $m_{F\text{-},Dilute}$ is $3 \cdot 10^{-4}$ mol/l and the standard deviation $m_{Standard\ dev}$ – determined by 10-fold measurement – was found to be 0.23 mol/l. Therefore, the uncertainty of the F-ISE measurement $m_{F\text{-}ISE}$ for the PSI etching bath is 0.27 mol/l or 1.4%, respectively, with regard to the concentrations listed in Table B3.

The uncertainty $m_{F\text{-},Dilute}$ is $2.5 \cdot 10^{-4}$ mol/l for the MacPSI etching bath, whereas the standard deviation is 0.12 mol/l within five measurements. Hence, the uncertainty of the F-ISE measurement $m_{F\text{-}ISE}$ for the MacPSI etching bath is 0.16 mol/l or 11.2%, respectively, again with regard to Table B3.

CUVETTE TEST METHOD

The uncertainty of the cuvette test measurements $m_{Cuvette\ test}$ consists of the systematic uncertainty of the concentration caused by the dilution of the etching bath sample $m_{TOC,Dilute}$ and the standard deviation of the measurements $m_{Standard\ dev.}$:

$$m_{Cuvette\ test} = m_{TOC,Dilute} + m_{Standard\ dev.}$$

Table B4 lists the corresponding error-afflicted parameters required for the following calculations. The uncertainty of the etching bath concentration $[TOC_{EB}]$ has been estimated to 5%.

The uncertainty of the concentration $[TOC_{Dilute}]$ has been determined as follows considering the volume of the sample V_{EB} and the concentration of the etching bath $[TOC_{EB}]$ as well as the volume of the diluted sample V_{Dilute} as error-afflicted parameters.

Table B4: Parameters for the determination of the uncertainty of the cuvette test method results.

Parameter	Typical value	Uncertainty
PSI etching bath		
Etching bath concentration $[TOC_{EB}]_{PSI}$	5.76 mol/l	0.29 mol/l
Volume of etching bath sample $V_{EB,PSI}$	0.35 ml	0.005 ml*
Measuring cylinder $V_{Dilute,PSI}$	1000 ml	0.08 ml*
MacPSI etching bath		
Etching bath concentration $[TOC_{EB}]_{MacPSI}$	1.14 mol/l	0.06 mol/l
Volume of etching bath sample $V_{EB,MacPSI}$	1.8 ml	0.03 ml*
Measuring cylinder $V_{Dilute,MacPSI}$	1000 ml	0.08 ml*

* As reported by the manufacturer.

$$[\mathrm{TOC}_{\mathrm{Dilute}}]=\frac{\mathrm{V}_{\mathrm{EB}}\,[\mathrm{TOC}_{\mathrm{EB}}]}{\mathrm{V}_{\mathrm{Dilute}}}$$

$$\mathrm{m}_{[\mathrm{TOC}_{\mathrm{Dilute}}]}=\sqrt{\left(\frac{\partial[\mathrm{TOC}_{\mathrm{Dilute}}]}{\partial \mathrm{V}_{\mathrm{EB}}}\right)^2 \mathrm{m}_{\mathrm{V}_{\mathrm{EB}}}^2+\left(\frac{\partial[\mathrm{TOC}_{\mathrm{Dilute}}]}{\partial[\mathrm{TOC}_{\mathrm{EB}}]}\right)^2 \mathrm{m}_{[\mathrm{TOC}_{\mathrm{EB}}]}^2+\left(\frac{\partial[\mathrm{TOC}_{\mathrm{Dilute}}]}{\partial \mathrm{V}_{\mathrm{Dilute}}}\right)^2 \mathrm{m}_{\mathrm{V}_{\mathrm{Dilute}}}^2}$$

$$=\sqrt{\left(\frac{[\mathrm{TOC}_{\mathrm{EB}}]}{\mathrm{V}_{\mathrm{Dilute}}}\right)^2 \mathrm{m}_{\mathrm{V}_{\mathrm{EB}}}^2+\left(\frac{\mathrm{V}_{\mathrm{EB}}}{\mathrm{V}_{\mathrm{Dilute}}}\right)^2 \mathrm{m}_{[\mathrm{TOC}_{\mathrm{EB}}]}^2+\left(-\frac{\mathrm{V}_{\mathrm{EB}}\,[\mathrm{TOC}_{\mathrm{EB}}]}{\mathrm{V}_{\mathrm{Dilute}}^2}\right)^2 \mathrm{m}_{\mathrm{V}_{\mathrm{Dilute}}}^2}$$

Accordingly, the uncertainty of $[TOC_{Dilute}]$ is about $1.0\cdot10^{-4}$ mol/l for the PSI etching bath depending on the etching bath concentration that ranges from the initial concentration to about 3 mol/l. The standard deviation $m_{Standard\ dev}$ has been determined by a 20-fold measurement to 0.01 mol/l. So, the uncertainty of the TOC measurement $m_{Cuvette\ test}$ calculates to 0.01 mol/l or 0.2%, respectively, for the initial PSI etching bath concentration of 5.76 mol/l.

The uncertainty for the MacPSI etching bath samples is $1.6\cdot10^{-4}$ mol/l regarding $[TOC_{Dilute}]$ and in the range of 0.005 mol/l regarding the standard deviation determined within 3 measurements. Finally, $m_{Cuvette\ test}$ for the MacPSI electrolyte is $5.2\cdot10^{-3}$ mol/l or 0.5%, respectively, concerning the concentrations listed in Table B4.

ION-CHROMATOGRAPHY

The uncertainty of the ion-chromatography measurements m_{IC} for the determination of the Si concentration calculates as the sum of the systematic uncertainty concerning the sample preparation $m_{Si,Dilute}$ and the standard deviation $m_{Standard\ dev}$.

$$\mathrm{m}_{\mathrm{IC}}=\mathrm{m}_{\mathrm{Si,Dilute}}+\mathrm{m}_{\mathrm{Standard\ dev.}}$$

The uncertainty of the sample preparation *[Si$_{Dilute}$]* has been determined taking the volume of the etching bath sample V_{EB}, the measuring cylinder V_{Dilute} and the etching bath concentration *[Si$_{EB}$]* as error-afflicted parameters as listed in Table B5. The uncertainty of the etching bath concentration *[Si$_{EB}$]* has been estimated to 5%.

Table B5: Parameters for the determination of the uncertainty of the IC results.

Parameter	Typical value	Uncertainty
PSI etching bath		
Etching bath concentration $[Si_{EB}]_{PSI}$	8.3 mmol/l	0.42 mmol/l
Volume of etching bath sample $V_{EB,PSI}$	0.5 ml	0.005 ml*
Measuring cylinder $V_{Dilute,PSI}$	250 ml	0.3 ml*
MacPSI etching bath		
Etching bath concentration $[Si_{EB}]_{MacPSI}$	165.7 mmol/l	8.3 mmol/l
Volume of etching bath sample $V_{EB,MacPSI}$	1 ml	0.006 ml*
Measuring cylinder $V_{Dilute,MacPSI}$	250 ml	0.3 ml*

* As reported by the manufacturer.

$$[Si_{Dilute}] = \frac{V_{EB}\,[Si_{EB}]}{V_{Dilute}}$$

$$m_{[Si_{Dilute}]} = \sqrt{\left(\frac{\partial[Si_{Dilute}]}{\partial V_{EB}}\right)^2 m_{V_{EB}}^2 + \left(\frac{\partial[Si_{Dilute}]}{\partial[Si_{EB}]}\right)^2 m_{[Si_{EB}]}^2 + \left(\frac{\partial[Si_{Dilute}]}{\partial V_{Dilute}}\right)^2 m_{V_{Dilute}}^2}$$

$$= \sqrt{\left(\frac{[Si_{EB}]}{V_{Dilute}}\right)^2 m_{V_{EB}}^2 + \left(\frac{V_{EB}}{V_{Dilute}}\right)^2 m_{[Si_{EB}]}^2 + \left(-\frac{V_{EB}[Si_{EB}]}{V_{Dilute}^2}\right)^2 m_{V_{Dilute}}^2}$$

As a consequence of this calculation, $m_{Si,Dilute}$ is in the range of 0.4 mmol/l for the PSI etching bath depending on the Si concentration in the bath. The standard deviation $m_{Standard\ dev}$ has been determined within 20 repeated measurements to 1.3 mmol/l. Therefore, the uncertainty of the Si measurements with IC m_{IC} is 1.7 mmol/l or 20% regarding the parameters in Table B5.

For the MacPSI etching bath, $m_{Si,Dilute}$ calculates to 8.3 mmol/l and $m_{Standard\ dev}$ within 20 measurements to 9.9 mmol/l. As a result, the uncertainty of the IC measurement m_{IC} for the MacPSI etching bath samples is 18.2 mmol/l or 11%, respectively, again with regard to Table B5.

DENSITY

Chapter 5 deals with the densities of the electrolytes. The uncertainty m_ρ of the density ρ has been determined as follows considering the weight *m* as well as the volume *V* of the measured electrolyte to be error-afflicted.

$$\rho = \frac{m}{V}$$

$$m_\rho = \sqrt{\left(\frac{\partial \rho}{\partial m}\right)^2 m_m^2 + \left(\frac{\partial \rho}{\partial V}\right)^2 m_V^2}$$

$$= \sqrt{\left(\frac{1}{V}\right)^2 m_m^2 + \left(-\frac{m}{V^2}\right)^2 m_V^2}$$

Here, *m* is the weight of the measured electrolyte determined by means of a balance, m_m is the sum of the standard deviation obtained by five measurements and the uncertainty of the balance of 0.0001 g (as reported by the manufacturer), *V* is the volume of the electrolyte (0.50 ml, 0.75 ml, 1.00 ml, 1.25 ml, and 1.50 ml), and m_V is the uncertainty of the pipettes with respect to the volume as reported by the manufacturer as listed in Table B6.

Table B6: Volumes and volume uncertainties as used for the determinations of the density. The uncertainties are reported by the manufacturer of the pipettes.

Volume	Uncertainty
0.50 ml	0.005 ml
0.75 ml	0.006 ml
1.00 ml	0.006 ml
1.25 ml	0.03 ml
1.50 ml	0.03 ml

As a result, the uncertainties of the determination of the density are in the range of 14 to 16 g/l corresponding to 1.3 to 1.4%, respectively.

SURFACE TENSION

The uncertainty m_σ of the surface tension σ in chapter 5 was determined considering the density of the electrolytes ρ, the radius of the capillary tube *r* as well as the capillary height Δh to be error-afflicted. The according data is given in Table B7.

Table B7: Parameters for the determination of the uncertainty of the surface tension.

Parameter	Typical value	Uncertainty
Density of the electrolyte *ρ*	1030-1108 g/l	14-16 g/l
Radius of the capillary tube *r*	0.4 mm	0.02 mm
Capillary height *Δh*	15-19 mm	1.3 mm

The uncertainty of the density m_ρ was determined above. The uncertainty of the radius of the capillary tubes m_r was estimated to be 5%. The uncertainty of the capillary height $m_{\Delta h}$ consists of the standard deviation within 10 measurements $m_{Standard\ dev.}$ as well as the uncertainty of the reading of the liquid height in the capillary $m_{Reading}$, which is estimated to 1 mm.

$$m_{\Delta h} = m_{\text{Standard dev.}} + m_{\text{Reading}}$$

Taking these considerations into account, the uncertainty of the surface tension m_σ is calculated by the following error-propagation and results in about 4 mN/m or 9.5%, respectively.

$$\sigma = \frac{\rho \cdot g \cdot \Delta h \cdot r}{2}$$

$$m_\sigma = \sqrt{\left(\frac{\partial\sigma}{\partial\Delta h}\right)^2 m_{\Delta h}^2 + \left(\frac{\partial\sigma}{\partial\rho}\right)^2 m_\rho^2 + \left(\frac{\partial\sigma}{\partial r}\right)^2 m_r^2}$$

$$= \sqrt{\left(\frac{\rho\, g\, r}{2}\right)^2 m_{\Delta h}^2 + \left(\frac{\Delta h\, g\, r}{2}\right)^2 m_\rho^2 + \left(\frac{\rho\, g\, \Delta h}{2}\right)^2 m_r^2}$$

VISCOSITY

The viscosity *η* in chapter 5.1.4 on page 69 is determined by the falling sphere method. Error-afflicted parameters are the falling distance *h*, the falling time *t*, and the density of the electrolyte *ρ* under investigation. The uncertainty of the latter was discussed above.

The uncertainty of the falling time m_t consists of the standard deviation $m_{Standard\ dev.}$ determined within 20 measurements and the uncertainty of the accuracy of the stop-watch $m_{Stopwatch}$. The latter was determined to be 0.2 s by 20-fold measurements in aqueous ethanol solutions.

$$m_t = m_{\text{Standard dev.}} + m_{\text{Stopwatch}}$$

The uncertainty of the dynamic viscosity m_η was determined by error propagation taking the error-afflicted parameters into consideration as listed in Table B8.

Table B8: Parameters for the determination of the uncertainty of the dynamic viscosity.

Parameter	Typical value	Uncertainty
Falling distance *h*	0.17 m	0.001 m
Falling time *t*	2 - 34 s	0.5 - 7 s
Density of the electrolyte *ρ*	1030- 1108 g/l	14 - 16 g/l

$$\eta = \frac{2\,r^2\,g\,(\rho_S - \rho_F)}{9\,\nu} = \frac{2\,r^2\,g\,(\rho_S - \rho_F)}{9\,h}\,t$$

$$m_\eta = \sqrt{\left(\frac{\partial \eta}{\partial \rho_F}\right)^2 m_{\rho_F}^2 + \left(\frac{\partial \eta}{\partial h}\right)^2 m_h^2 + \left(\frac{\partial \eta}{\partial t}\right)^2 m_t^2}$$

$$= \sqrt{\left(\frac{2\,r^2\,g\,(\rho_S - 1)\,t}{9\,h}\right)^2 m_{\rho_F}^2 + \left(-\frac{2\,r^2\,g\,(\rho_S - \rho_F)\,t}{9\,h^2}\right)^2 m_h^2 + \left(\frac{2\,r^2\,g\,(\rho_S - \rho_F)}{9\,h}\right)^2 m_t^2}$$

The uncertainty of the viscosity results in 1 - 5 mPa s and is included in Table E6 on page 144.

C EXPERIMENTAL DATA ACCORDING TO CHAPTER 3

Please note that the uncertainties in this chapter were determined according to Appendix B.

Calibration Data

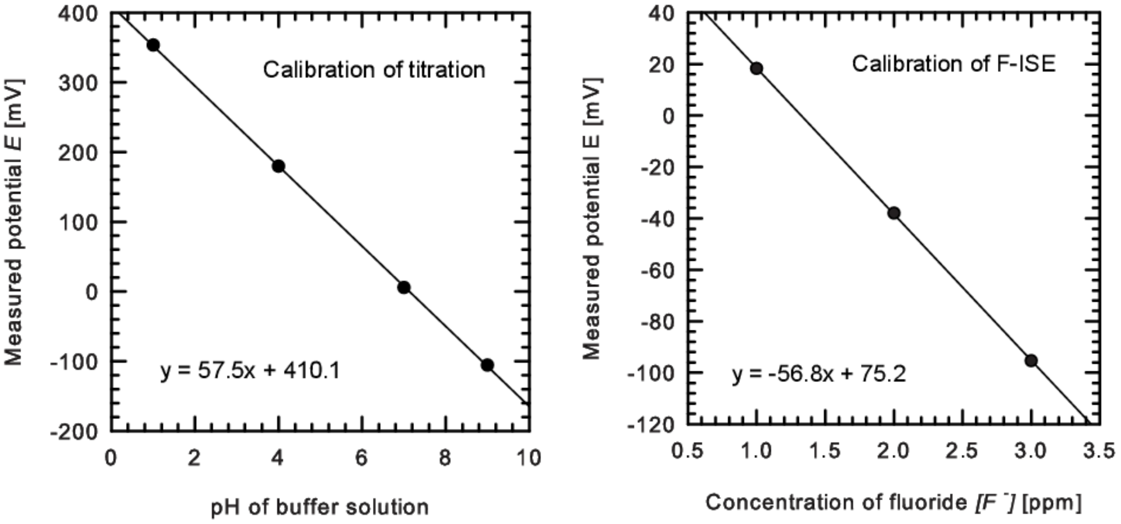

Figure C1: Exemplary calibration data for the fluoride determining methods, titration (on the left side) and F-ISE (on the right side).

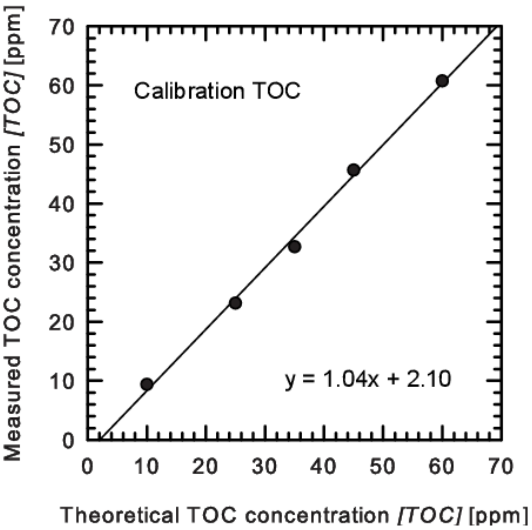

Figure C2: Exemplary calibration data for the cuvette test method.

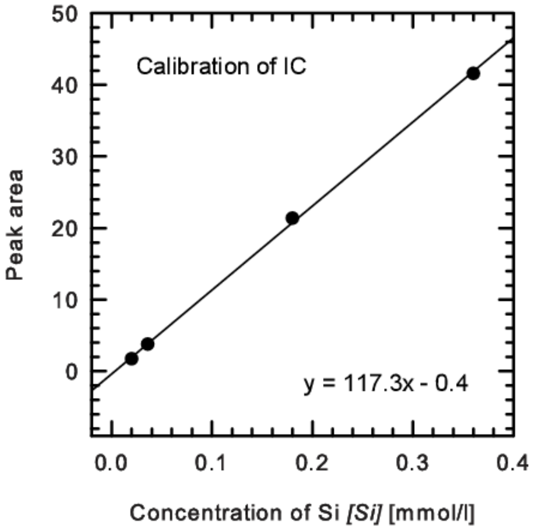

Figure C3: Exemplary calibration data for ion-chromatography.

Comparison of titration and F-ISE

Table C1: Experimental data for Figure 24 “Conformity test of data points of titration and F-ISE“; given is the mean value of two measurements. The concentration of the lanthanum nitrate solution was determined to (0.09+0.02) mol/l. The uncertainty of the titration and the F-ISE results is 0.3 mol/l for each measurement.

Date	Titration $[F^-]$ [mol/l]	Number of repetitions	F-ISE $[F^-]$ [mol/l]	Number of repetitions
20.01.2011	19.3	2	18.7	2
20.01.2011	19.1	2	18.7	2
21.01.2011	19.1	2	18.8	2
25.01.2011	18.8	2	18.6	2
26.01.2011	18.7	2	18.6	2
27.01.2011	18.6	2	18.3	2
27.01.2011	19.2	2	18.9	2
27.01.2011	19.1	2	18.9	2
28.01.2011	19.0	2	18.5	2
31.01.2011	18.7	3	18.6	4
01.02.2011	18.7	4	18.5	2
02.02.2011	18.6	3	18.3	2
03.02.2011	18.4	3	18.2	2
04.02.2011	18.3	3	18.1	2
07.02.2011	18.2	2	18.0	2
07.02.2011	19.0	2	18.8	2

Date	Titration [F $^-$] [mol/l]	Number of repetitions	F-ISE [F $^-$] [mol/l]	Number of repetitions
07.02.2011	18.9	2	18.7	2
07.02.2011	19.0	4	18.9	2
08.02.2011	19.3	2	19.2	3
08.02.2011	19.3	2	19.3	2
14.02.2011	19.3	3	19.2	2
17.02.2011	19.2	2	18.9	2
17.02.2011	19.3	2	19.2	2
28.02.2011	19.1	2	18.7	2
28.02.2011	19.3	3	18.9	2
28.02.2011	19.1	2	18.8	2
01.03.2011	19.4	2	19.2	2
01.03.2011	19.3	2	19.0	2
03.03.2011	19.3	2	19.0	2
09.03.2011	19.2	2	18.8	2
09.03.2011	19.2	2	18.9	2
10.03.2011	19.0	4	18.7	2
10.03.2011	19.4	2	19.1	2
15.03.2011	19.4	2	19.2	2
16.03.2011	19.2	2	19.0	2
16.03.2011	19.4	2	19.1	2
22.03.2011	18.6	2	18.4	2
22.03.2011	19.3	2	19.2	2

Recovery rates of titration

Table C2: Titration results for HF in water.

Target HF concentration [mol/l]	Actual HF concentration [mol/l]	Recovery rate [%]
12.99	12.85	98.9
19.49	19.39	99.5
21.54	21.69	100.7

Table C3: Titration results for HF in ethanol.

Target HF concentration [mol/l]	Actual HF concentration [mol/l]	Recovery rate [%]
12.99	13.07	100.6
19.49	19.39	99.5
21.54	21.65	100.5

Recovery rates of F-ISE

Table C4: F-ISE results for HF in water.

Target HF concentration [mol/l]	Actual HF concentration [mol/l]	Recovery rate [%]
12.99	12.92	99.4
19.49	19.55	100.3
21.54	21.69	100.7

Table C5: F-ISE results for HF in ethanol.

Target HF concentration [mol/l]	Actual HF concentration [mol/l]	Recovery rate [%]
12.99	12.97	99.8
19.49	19.49	100.0
21.54	21.59	100.2

Recovery rates of the cuvette test method

Table C6: Cuvette test results for ethanol in water.

Target ethanol concentration [mol/l]	Actual ethanol concentration [mol/l]	Recovery rate [%]
3.96	3.93	99.2
5.72	5.78	101.0
7.62	7.84	102.9

Table C7: Cuvette test results for ethanol in HF.

Target ethanol concentration [mol/l]	Actual ethanol concentration [mol/l]	Recovery rate [%]
3.96	3.92	99.0
5.72	5.64	98.6
7.62	7.73	101.4

Recovery rates of ion-chromatography

Table C8: Ion-chromatography results for Si^{4+} in water.

Target Si^{4+} concentration [mmol/l]	Actual Si^{4+} concentration [mmol/l]	Recovery rate [%]
0.071	0.069	96.7
0.178	0.168	94.4
0.285	0.282	98.9

Table C9: Ion-chromatography results for Si^{4+} in ethanol-HF.

Target Si^{4+} concentration [mmol/l]	Actual Si^{4+} concentration [mmol/l]	Recovery rate [%]
0.071	0.079	110.4
0.178	0.178	99.9
0.285	0.286	100.4

D EXPERIMENTAL DATA ACCORDING TO CHAPTER 4

D1 THE ISFH TOOL

Decrease of HF in the ISFH tool before the implementation of replenishment

Table D1: Decrease of the total fluoride concentration $[F^-]_{total}$ at the beginning of chemical analysis in the ISFH etching tool determined by titration. Experimental data to Figure 25, the uncertainty is 0.3 mol/l according to the determination of the uncertainties in Appendix B. Given is the mean value of two measurements per sample.

Date	Number of etched wafers	Total fluoride concentration [mol/l]
23.04.2010	0	18.0
27.04.2010	50	17.9
06.05.2010	60	17.7
06.05.2010	70	17.5
17.05.2010	80	17.4
17.05.2010	90	17.2
18.05.2010	100	17.0
22.06.2010	110	17.0
22.06.2010	120	16.9
23.06.2010	130	16.6
02.07.2010	140	16.2
07.07.2010	150	16.0
07.07.2010	159	15.8
09.07.2010	168	15.8
09.07.2010	177	15.5
09.07.2010	186	15.6
27.07.2010	196	15.3
27.07.2010	206	15.2
28.07.2010	216	14.9
28.07.2010	226	14.8
28.07.2010	236	14.8

Decrease of HF in the ISFH tool due to evaporation

Table D2: Decrease of the total fluoride concentration *$[F^-]_{total}$* due to evaporation from the reservoir. Experimental data to Figure 26 obtained with titration; the uncertainty is 0.3 mol/l according to the determination of the uncertainties in Appendix B. Given is the mean value of two measurements per sample.

Date	Evaporation time [day]	Total fluoride concentration [mol/l]
27.01.2011	0	18.3
28.01.2011	0.85	18.2
31.01.2011	3.85	17.9
01.02.2011	4.85	18.0
02.02.2011	5.85	17.9
03.02.2011	6.85	17.7
04.02.2011	7.85	17.5
07.02.2011	10.85	17.4

Development of the HF concentration in the ISFH tool with replenishment

Table D3: Development of the total fluoride concentration *$[F^-]_{total}$* and the ethanol concentration *[EtOH]* in a replenished electrolyte in the ISFH tool. Samples marked with an asterisk* indicate that replenishment was necessary. Experimental data to Figure 27. The uncertainty for the fluoride determination is 0.3 mol/l according to Appendix B; the listed results are the mean of two measurements. For the ethanol concentration, the uncertainty is 0.1 mol/l and given is the mean of three measurements.

Date	Number of etched wafers	Total fluoride concentration [mol/l]	Ethanol concentration [mol/l]
31.08.2011	0	18.5	-
01.09.2011	200	18.6	5.2
08.09.2011	211	18.2*	5.3
08.09.2011	211	18.7	-
13.09.2011	221	18.4*	4.9
13.09.2011	221	18.6	-
20.09.2011	232	-	4.7
26.09.2011	242	17.8*	4.7
26.09.2011	242	18.8	-
29.09.2011	252	-	4.3
05.10.2011	262	18.0*	4.2

Date	Number of etched wafers	Total fluoride concentration [mol/l]	Ethanol concentration [mol/l]
05.10.2011	262	18.4	-
06.10.2011	272	18.0*	4.0
06.10.2011	272	18.8	-
24.10.2011	272	-	3.8

D2 THE SSE TOOL

Etched wafers and bath volume of the SSE tool during investigation

Table D4: Technical data concerning the SSE tool. The bath volume is roughly indicated by means of a filling level. The asterisk* indicates where the electrolyte was replenished, the hash key# indicates where the structural upgrade of the tool was performed. Each replenishment was performed with 7.5 l of the initial electrolyte concentration. The uncertainty of the bath volume – required for the determination of the theoretical Si concentration – is related to the incorrect indication of the filling level.

Date	Number of etched wafers	Filling level [%]	Approximate bath volume [l]
17.11.2011	0	61.50	29.8
12.12.2011	428	53.27	25.8
13.12.2011	453	51.33	24.9
14.12.2011	478	49.95*	24.2*
04.01.2012	489	58.02	31.6
05.01.2012	504	57.00	31.1
09.01.2012	519	56.55	30.9
10.01.2012	539	54.89	30.1
18.01.2012	549	53.62	29.5
19.01.2012	569	52.02#	28.7#
14.02.2012	589	52.92	29.1
20.02.2012	592	51.41	28.4
21.02.2012	603	50.75	28.1
28.02.2012	614	49.94	27.7
29.02.2012	634	49.15*	27.3*
06.03.2012	648	58.60	34.9
16.03.2012	708	55.73	33.5

Development of the HF concentration in the SSE tool

Table D5: Total fluoride concentration in the SSE tool over a period of three months as determined by titration. Experimental data to Figure 29. The uncertainty for each measurement is 0.3 mol/l according to Appendix B; given is the mean of two measurements.

Date	Number of etched wafers	Total fluoride concentration [mol/l]
17.11.2011	0	18.1
21.11.2011	190	18.2
23.11.2011	326	18.1
24.11.2011	336	18.1
25.11.2011	350	18.2
05.12.2011	368	18.3
06.12.2011	388	18.2
07.12.2011	398	18.1
12.12.2011	428	18.2
13.12.2011	453	18.2
14.12.2011	478	18.3
04.01.2012	489	18.8 (replenished)
05.01.2012	504	18.6
09.01.2012	519	18.6
10.01.2012	539	18.7
18.01.2012	549	18.7
19.01.2012	569	18.7

Development of the ethanol concentration in the SSE tool

Table D6: Development of the ethanol concentrations *[EtOH]* in the ISFH and the SSE tool in an investigation period of about four weeks. Experimental data to Figure 30. The uncertainty is 0.1 mol/l according to Appendix B; the listed results are the mean of three measurements.

	Date	Number of etched wafers	Ethanol concentration [mol/l]
ISFH tool	01.09.2011	200	5.2
	08.09.2011	210	5.3
	13.09.2011	221	4.9
	20.09.2011	231	4.7
	26.09.2011	241	4.7

	Date	Number of etched wafers	Ethanol concentration [mol/l]
ISFH tool (continued)	29.09.2011	251	4.3
	05.10.2011	261	4.2
	06.10.2011	271	4.0
SSE tool	21.11.2011	190	5.0
	23.11.2011	326	5.0
	24.11.2011	336	4.8
	25.11.2011	350	4.7
	05.12.2011	368	4.7
	06.12.2011	388	4.6
	07.12.2011	398	4.5
	12.12.2011	428	4.6
	13.12.2011	453	4.4
	14.12.2011	478	4.2

Development of the dissolved silicon concentration in the SSE tool

Table D7: Development of the dissolved Si concentration in the SSE tool. Experimental data to Figure 32. The uncertainty is 1.7 mmol/l according to Appendix B. Replenishment = *, structural upgrade = #.

Date	Number of etched wafers	Si concentration, theoretical [mmol/l]	Si concentration, experimental [mmol/l]
17.11.2011	0	0	-
21.11.2011	190	4.6	-
23.11.2011	326	7.9	-
24.11.2011	336	8.2	-
25.11.2011	350	8.6	-
05.12.2011	368	9.4	-
06.12.2011	388	10.2	-
07.12.2011	398	10.6	-
12.12.2011	428	11.9	4.24
13.12.2011	453	13.1	8.51
14.12.2011	478*	14.2	8.42
04.01.2012	489	12.5	6.55
05.01.2012	504	11.4	7.87
09.01.2012	519	11.9	9.03

Date	Number of etched wafers	Si concentration, theoretical [mmol/l]	Si concentration, experimental [mmol/l]
10.01.2012	539	12.6	9.65
18.01.2012	549	13.1	11.75
19.01.2012	569#	14.0	12.48
14.02.2012	589	14.3	8.67
20.02.2012	592	14.7	13.48
21.02.2012	603	15.1	15.26
28.02.2012	614	15.6	15.10
29.02.2012	634*	16.3	12.66
06.03.2012	648	13.1	8.92
16.03.2012	708	14.9	8.40

Development of the free fluoride concentration in the SSE tool

Table D8: Development of the free fluoride concentration in the SSE tool. Experimental data to Figure 33. The uncertainty is 0.3 mol/l according to Appendix B, given is the mean of two measurements. Replenishment = *, structural upgrade = #.

Date	Number of etched wafers	Free fluoride concentration [mol/l]	Total fluoride concentration [mol/l]
01.09.2011	200	18.1	18.1
08.09.2011	210	18.1	18.2
13.09.2011	221	18.0	18.1
20.09.2011	231	18.0	18.1
26.09.2011	241	18.1	18.2
29.09.2011	251	18.3	18.3
05.10.2011	261	18.1	18.2
06.10.2011	271	18.1	18.1
21.11.2011	190	18.2	18.2
23.11.2011	326	18.1	18.2
24.11.2011	336	18.2	18.3
25.11.2011	350	18.8	18.8
05.12.2011	368	18.5	18.6
06.12.2011	388	18.5	18.6
07.12.2011	398	18.6	18.7
12.12.2011	428*	18.6	18.7
13.12.2011	453	18.6	18.7

Date	Number of etched wafers	Free fluoride concentration [mol/l]	Total fluoride concentration [mol/l]
14.12.2011	478	15.6	15.6
04.01.2012	489	15.8	15.9
05.01.2012	504	15.8	15.8
09.01.2012	519	15.9	16.0
10.01.2012	539	15.8	15.9
18.01.2012	549	16.3	16.4
19.01.2012	569#	16.7	16.8
14.02.2012	589	18.1	18.1
20.02.2012	592	18.1	18.2
21.02.2012	603	18.0	18.1
28.02.2012	614	18.0	18.1
29.02.2012	634*	18.1	18.2
06.03.2012	648	18.3	18.3
16.03.2012	708	18.1	18.2

D3 THE MACPSI TOOL

Analysis of the total fluoride concentration in the MacPSI electrolyte

Table D9: Concentration of the total fluoride concentration determined by F-ISE in the MacPSI Electrolyte. Experimental data to Figure 34; the uncertainty is 0.16 mol/l for each experimental measurement. Given is the mean of two measurements.

Number of etched wafers	Total fluoride concentration, expected [mol/l]	Total fluoride concentration, experimental [mol/l]
0	1.43	1.41
5	1.54	1.55
10	1.66	1.58
20	1.89	1.79
30	2.11	2.10

Analysis of the dissolved silicon concentration in the MacPSI electrolyte

Table D10: Concentration of the dissolved Si measured as Si^{4+} by ion-chromatography in the MacPSI etching bath. Experimental data to Figure 35.

Number of etched wafers	Dissolved silicon concentration [mmol/l]
10	30 ± 3
20	65 ± 7
30	103 ± 11

Analysis of the free fluoride concentration in the MacPSI electrolyte

Table D11: Concentration of the free fluoride in the MacPSI etching bath calculated from equation (2.22). Experimental data to Figure 36. The uncertainty of the experimental data is 0.16 mol/l.

Number of etched wafers	Free fluoride concentration, expected [mol/l]	Free fluoride concentration, experimental [mol/l]
0	1.43	1.41
10	1.43	1.40
20	1.44	1.40
30	1.44	1.48

Analysis of the acetic acid concentration in the MacPSI electrolyte

Table D12: Concentration of the acetic acid in two electrolytes of the same initial concentration. Determination by the cuvette test method, given is the experimental data to Figure 37. The uncertainty is 0.01 mol/l for each experimental measurement, given is the mean of three measurements.

Number of etched wafers	Expected Acetic acid concentration [mol/l]	Bath A: Acetic acid concentration [mol/l]	Bath B: Acetic acid concentration [mol/l]
0	1.14	1.13	1.11
5	1.14	1.15	-
10	1.13	1.12 (11 Wafer)	1.10
15	1.12	-	-
20	1.12	1.09 (21 Wafer)	1.13
25	1.11	-	-
30	1.11	-	1.12

E EXPERIMENTAL DATA ACCORDING TO CHAPTER 5

Determination of the density of HF-EtOH-H_2O electrolytes

Table E1: Experimental data for the determination of the density of HF-EtOH-H_2O electrolytes.

Sample	Weight of 0.5 ml [g]	Weight of 0.75 ml [g]	Weight of 1.0 ml [g]	Weight of 1.25 ml [g]	Weight of 1.5 ml [g]
19.5 mol/l HF and 5.7 mol/l ethanol	0.5120	0.7755	1.0301	1.2907	1.5435
	0.5187	0.7725	1.0329	1.2917	1.5460
	0.5150	0.7743	1.0340	1.2929	1.5450
	0.5180	0.7750	1.0348	1.2855	1.5418
	0.5065	0.7710	1.0330	1.2840	1.5430
19.5 mol/l HF and 4.6 mol/l ethanol	0.5269	0.7900	1.0566	1.3157	1.5669
	0.5266	0.7932	1.0592	1.3142	1.5721
	0.5245	0.7906	1.0582	1.3163	1.5689
	0.5267	0.7901	1.0589	1.3155	1.5705
	0.5256	0.7932	1.0577	1.3031	1.5702
19.5 mol/l HF and 3.4 mol/l ethanol	0.5350	0.8054	1.0756	1.3381	1.6077
	0.5337	0.8043	1.0753	1.3396	1.6102
	0.5366	0.8047	1.0755	1.3414	1.6115
	0.5325	0.8048	1.0752	1.3378	1.6089
	0.5386	0.8037	1.0755	1.3400	1.6121
19.5 mol/l HF and 2.3 mol/l ethanol	0.5451	0.8169	1.0914	1.3566	1.6325
	0.5430	0.8177	1.0907	1.3587	1.6307
	0.5438	0.8168	1.0937	1.3566	1.6314
	0.5442	0.8176	1.0939	1.3542	1.6336
	0.5427	0.8176	1.0933	1.3532	1.6316
19.5 mol/l HF and 1.1 mol/l ethanol	0.5504	0.8251	1.1064	1.3765	1.6528
	0.5521	0.8226	1.1051	1.3762	1.6590
	0.5517	0.8280	1.1043	1.3756	1.6599
	0.5513	0.8296	1.1027	1.3746	1.6535
	0.5503	0.8295	1.1057	1.3739	1.6521
19.5 mol/l HF	0.5646	0.8395	1.1210	1.3846	1.6731
	0.5610	0.8392	1.1225	1.3886	1.6706
	0.5585	0.8383	1.1233	1.3851	1.6684
	0.5550	0.8410	1.1252	1.3879	1.6700
	0.5550	0.8395	1.1233	1.3880	1.6672

Table E2: Experimentally determined densities for HF-EtOH-H_2O electrolytes with a HF concentration of 19.5 mol/l. Data to Figure 39, the uncertainty was determined according to Appendix B.

Ethanol in sample [mol/l]	Density of HF-EtOH-H_2O (with [HF] = 19.5 mol/l) [g/l]
0	1108 ± 16
1.1	1103 ± 15
2.3	1086 ± 15
3.4	1074 ± 15
4.6	1044 ± 14
5.7	1030 ± 15

Capillary height in glass capillary tubes

Table E3: Determination of the capillary height of HF-EtOH-H_2O in glass capillary tubes. Experimental data to Figure 40. The determination of the uncertainty is described in chapter 5.1.2. Each data point is the mean of a tenfold measurement.

Ethanol concentration [mol/l]	Capillary height glass tube [mm]
0.0	19.10 ± 1.5
1.6	18.30 ± 1.3
2.9	17.00 ± 1.2
3.5	16.45 ± 1.4
3.8	16.25 ± 1.3
4.0	16.25 ± 1.5
4.25	16.00 ± 1.4
4.9	15.75 ± 1.3
5.7	15.25 ± 1.4

Surface tension of HF-EtOH-H_2O electrolytes

Table E4: Experimentally determined surface tensions for HF-EtOH-H_2O solutions with a constant HF concentration of 19.5 mol/l. Experimental data to Figure 41, the uncertainty was determined according to Appendix B.

Ethanol in sample [mol/l]	Surface tension of HF-EtOH-H_2O [mN/m]
0.0	42 + 4
1.6	39 ± 4
2.9	36 ± 3
4.0	34 ± 4
4.9	32 ± 3
5.7	31 ± 3

Contact angles of EtOH-H_2O solutions

Table E5: Contact angles of EtOH-H_2O solutions on a porosified *p*-type Si wafer. Experimental data to Figure 43, the uncertainties are the mean of five measurements each.

Ethanol in sample [mol/l]	Contact angle θ [°]
0	81 ± 1
1.6	61 ± 1
2.9	48 ± 1
4.0	39 ± 2
4.9	36 ± 2
5.7	29 ± 1

Falling times and viscosities in HF-EtOH-H_2O solutions

Table E6: Experimentally determined falling times and calculated dynamic viscosities for HF-EtOH-H_2O solutions. The uncertainties of the falling times were determined by a 20-fold measurement and the uncertainty of the stop watch; the uncertainty of the viscosity was determined according to Appendix B. Experimental data according to Figure 46.

Ethanol in sample [mol/l]	3.5	3.8	4.25	4.9	5.7
Time [s]	34 ± 7	25 ± 6	16 ± 2	13 ± 2	8.1 ± 0.5
Viscosity [mPa·s]	4.05 ± 4.9	3.18 ± 3.6	2.21 ± 2.3	2.05 ± 1.9	1.48 ± 1.2

Permeation of HF-EtOH-H_2O solutions through porous silicon

Table E7: Investigation of the permeability of porous Si for HF-EtOH-H_2O solutions. Experimental data to Figure 50. Given is the time [min] required for the solution to reach the appearance of the drop according to Figure 49.

Ethanol concentration [mol/l]	Permeation Level (3)	Permeation Level (4)	Permeation Level (5)	Permeation Level (6)
5.7	1	2	4	7
5.3	1	2	4	8
4.9	1	3	6	11
4.3	1	4	6	12
3.0	1	7	10	26
2.0	2	8	21	30

Formation of hydrogen bubbles on the porous silicon surface

Table E8: Investigation of the size and number of hydrogen bubbles with decreasing ethanol concentration in the PSI electrolyte. Experimental data to Figure 52.

Ethanol concentration [mol/l]	Volume of segment, V_{Seg} [cm^{-3}]	Radius of H_2 bubble [mm]	Number of H_2 bubble [s^{-1} cm^{-2}]
0.0	0.133	5.61	$3.27 \cdot 10^{-5}$
1.6	0.099	5.17	$4.39 \cdot 10^{-5}$
2.9	0.062	4.24	$7.05 \cdot 10^{-5}$
3.5	0.049	3.84	$8.81 \cdot 10^{-5}$
3.8	0.045	3.67	$9.74 \cdot 10^{-5}$
4.0	0.042	3.59	$1.02 \cdot 10^{-4}$
4.25	0.039	3.46	$1.11 \cdot 10^{-4}$
4.9	0.034	3.24	$1.28 \cdot 10^{-4}$
5.7	0.027	2.94	$1.59 \cdot 10^{-4}$

F EXPERIMENTAL DATA ACCORDING TO CHAPTER 6

Determination of the uncertainty of the experimentally determined silicon concentration

The amount of dissolved Si in chapter 6 is determined according to equation (6.9) as

$$[\mathrm{Si}]_{\mathrm{dissolved}} = [\mathrm{Si}]_{\mathrm{measured}} - [\mathrm{SiF}_6^{2-}]_{\mathrm{initial}} - [\mathrm{Si}]_{\mathrm{water}} \qquad (6.9).$$

The uncertainty of the measured Si $[\mathrm{Si}]_{measured}$ is 20% according to the uncertainty of the IC measurement as determined in Appendix B. Since $[\mathrm{Si}]_{water}$ is a further result of a IC measurement, this uncertainty is taken as 20%, too. The aqueous SiF_6^{2-} solutions were diluted from a (7.00 ± 0.03) mmol/l stock solution; therefore, the uncertainty of the $[\mathrm{SiF}_6^{2-}]_{initial}$ calculates following

$$[\mathrm{Si\,F}_6^{2-}]_{\mathrm{Inital}} = \frac{V_{\mathrm{Stock}}\,[\mathrm{Si}]_{\mathrm{Stock}}}{V_{\mathrm{Dilute}}}$$

$$m_{[\mathrm{Si}_{\mathrm{Initial}}]} = \sqrt{\left(\frac{\partial[\mathrm{Si\,F}_6^{2-}]_{\mathrm{Inital}}}{\partial V_{\mathrm{Stock}}}\right)^2 m^2_{V_{\mathrm{Stock}}} + \left(\frac{\partial[\mathrm{Si\,F}_6^{2-}]_{\mathrm{Inital}}}{\partial[\mathrm{Si}_{\mathrm{Stock}}]}\right)^2 m^2_{[\mathrm{Si\ Stock}]} + \left(\frac{\partial[\mathrm{Si\,F}_6^{2-}]_{\mathrm{Inital}}}{\partial V_{\mathrm{Dilute}}}\right)^2 m^2_{V_{\mathrm{Dilute}}}}$$

$$= \sqrt{\left(\frac{[\mathrm{Si}]_{\mathrm{Stock}}]}{V_{\mathrm{Dilute}}}\right)^2 m^2_{V_{\mathrm{Stock}}} + \left(\frac{V_{\mathrm{Stock}}}{V_{\mathrm{Dilute}}}\right)^2 m^2_{[\mathrm{Si}]_{\mathrm{Stock}}} + \left(-\frac{V_{\mathrm{Stock}}[\mathrm{Si}]_{\mathrm{Stock}}}{V^2_{\mathrm{Dilute}}}\right)^2 m^2_{V_{\mathrm{Dilute}}}}$$

taking into consideration: V_{Stock} = (2.5 ± 0.05) ml and V_{Dilute} = (100 ± 0.05) ml. Finally, $[\mathrm{SiF}_6^{2-}]_{initial}$ calculates to (0.18 ± 0.04) mmol/l.

Consequently, the uncertainty of the dissolved Si from equation (6.9) is calculated by

$$m_{[\mathrm{Si}]_{\mathrm{dissolved}}} = \sqrt{\left(\frac{\partial[\mathrm{Si}]_{\mathrm{dissolved}}}{\partial[\mathrm{Si}]_{\mathrm{measured}}}\right)^2 m^2_{[\mathrm{Si}]_{\mathrm{measured}}} + \left(\frac{\partial[\mathrm{Si}]_{\mathrm{dissolved}}}{\partial[\mathrm{Si\,F}_6^{2-}]_{\mathrm{initial}}}\right)^2 m^2_{[\mathrm{SiF}_6^{2-}]_{\mathrm{initial}}} + \left(\frac{\partial[\mathrm{Si}]_{\mathrm{dissolved}}}{\partial[\mathrm{Si}]_{\mathrm{Water}}}\right)^2 m^2_{[\mathrm{Si}]_{\mathrm{water}}}}$$

$$= \sqrt{\left(1-[\mathrm{Si\,F}_6^{2-}]_{\mathrm{initial}}-[\mathrm{Si}]_{\mathrm{water}}\right)^2 m^2_{[\mathrm{Si}]_{\mathrm{measured}}} + \left([\mathrm{Si}]_{\mathrm{measured}}-1-[\mathrm{Si}]_{\mathrm{water}}\right)^2 m^2_{[\mathrm{SiF}_6^{2-}]_{\mathrm{initial}}} + \ldots.}$$

$$\sqrt{\ldots + ([\mathrm{Si}]_{\mathrm{measured}} - [\mathrm{Si\,F}_6^{2-}]_{\mathrm{initial}} - 1)^2 m^2_{[\mathrm{Si}]_{\mathrm{water}}}}$$

The uncertainty of $[\mathrm{Si}]_{dissolved}$ calculates to $1.6\cdot10^{-5}$ mmol/l, which is 23% with regard to a Si concentration of $7\cdot10^{-5}$ mmol/l.

Water dissolving oxidized porous silicon

Table F1: Development of the Si concentration in samples containing water and oxidized porous Si. Experimental data to Figure 57. The uncertainty is $1.6 \cdot 10^{-5}$ mmol/l. The data corresponds to $[Si]_{water}$ in equation (6.9).

Time [min]	pH 1 Si concentration [10^{-5} mmol/l]	pH 2 Si concentration [10^{-5} mmol/l]	pH 3 Si concentration [10^{-5} mmol/l]
0	0	0	0
0.33	0.23	0.05	0.01
0.66	0.19	0.18	0.02
1	0.15	0.10	0.02
1.33	0.24	0.26	0.04
1.66	0.29	0.10	0.03
2	0.33	0.18	0.01
5	0.47	0.46	0.10
10	0.53	0.37	0.35
30	0.65	1.50	1.10
60	1.24	2.81	1.83

Water dissolving non-oxidized porous silicon

Table F2: Development of the Si concentration in samples containing water and non-oxidized porous Si. Experimental data to Figure 57. The uncertainty is $1.6 \cdot 10^{-5}$ mmol/l. The data corresponds to $[Si]_{water}$ in equation (6.9).

Time [min]	pH 1 Si concentration [10^{-5} mmol/l]	pH 2 Si concentration [10^{-5} mmol/l]	pH 3 Si concentration [10^{-5} mmol/l]
0	0	0	0
0.33	0.32	0.27	0.33
0.66	0.33	0.20	0.67
1	0.37	0.07	0.42
1.33	0.46	0.20	0.44
1.66	0.59	0.09	0.46
2	0.56	0.44	0.44
5	0.70	0.12	0.35
10	0.75	0.27	0.38
30	1.44	0.84	1.62
60	2.09	0.96	1.98

Aqueous SiF_6^{2-} dissolving oxidized porous silicon

Table F3: Development of the Si concentration in samples containing aqueous SiF_6^{2-} and oxidized porous Si. Experimental data to Figures 58 and 59. The uncertainty is $1.6\cdot10^{-5}$ mmol/l. The data corresponds to $[Si]_{dissolved}$ according to equation (6.9).

Time [min]	pH 1 Si concentration [10^{-5} mmol/l]	pH 2 Si concentration [10^{-5} mmol/l]	pH 3 Si concentration [10^{-5} mmol/l]
0	-0.05	-0.05	-0.01
0.33	0.39	0.88	-0.41
0.66	0.77	0.84	0.73
1	1.76	1.08	0.32
1.33	1.93	1.45	0.48
1.66	2.52	2.07	0.20
2	3.43	2.31	1.49
5	3.49	1.95	1.68
10	4.39	2.35	1.84
30	6.24	3.02	2.58
60	7.01	2.68	3.41

Aqueous SiF_6^{2-} dissolving non-oxidized porous silicon

Table F4: Development of the Si concentration in samples containing aqueous SiF_6^{2-} and non-oxidized porous Si. Experimental data to Figure 60. The uncertainty is $1.6\cdot10^{-5}$ mmol/l. The data corresponds to $[Si]_{dissolved}$ according to equation (6.9).

Time [min]	pH 1 Si concentration [10^{-5} mmol/l]	pH 2 Si concentration [10^{-5} mmol/l]	pH 3 Si concentration [10^{-5} mmol/l]
0	-0.04	-0.20	-0.04
0.33	-0.13	-0.17	-1.58
0.66	-0.32	0.03	-2.26
1	-0.41	0.32	-1.91
1.33	-0.66	0.47	-2.33
1.66	-0.80	0.64	-2.44
2	-0.22	0.42	-2.63
5	-0.48	0.89	-1.99
10	-0.86	1.31	-2.39
30	-1.65	1.37	-2.69
60	-2.41	1.72	-2.18

Calculation of the amount of silicon oxide on porous silicon

The volume of the porous Si is calculated according to

$$V_{PSI} = \frac{m_{PSI}}{\rho_{PSI}} = \frac{m_{PSI}}{\rho_{Si}(1-P)} = 0.0549\ \mathrm{cm}^3\ .$$

Here, the porosity *P* is 22%, and the mass of the porous Si m_{PSI} is 0.1 g. The product of V_{PSI} and the surface of porous Si S_{SiO2} from [48], i.e., 230 m^2/cm^3, gives the area of the silicon oxide A_{SiO2}. Together with the thickness of the oxide t_{SiO2}, i.e., 0.6 nm [110], we calculate the volume of the silicon oxide to

$$V_{SiO_2} = A_{SiO_2} \cdot t_{SiO_2} = V_{PSI} \cdot S_{SiO_2} \cdot t_{SiO_2} = 7.6 \cdot 10^{-9}\mathrm{m}^3\ .$$

The mass of the silicon oxide on the porous Si is calculated taking the density of SiO_2 into consideration, ρ_{SiO2} = 2.65 g/cm^3.

$$m_{SiO_2} = V_{SiO_2} \cdot \rho_{SiO_2} = 20.1\ \mathrm{mg}$$

Finally, if all this silicon dioxide would dissolve during the reaction discussed in chapter 6, the concentration of the dissolved Si is

$$[Si]_{dissolved} = \frac{n_{SiO_2}}{V_{Sample}} = \frac{m_{SiO_2}/M_{SiO_2}}{V_{Sample}} = 3.5 \cdot 10^{-3}\ \frac{\mathrm{mol}}{\mathrm{l}}$$

with the sample volume of 96 ml.

Investigation of the standard potentials at increasing dissolved silicon concentration

Table F5: Development of the electrode potential for the anodic oxidation of Si with regard to the increased concentration of the reaction product SiF_6^{2-}. Calculated data to Figure 61.

Concentration of SiF_6^{2-} [mol/l]	Electrode potential [V]
0.001	-1.41
0.01	-1.40
0.1	-1.38
1	-1.37
10	-1.36

LIST OF PUBLICATIONS

REFEREED JOURNAL PAPERS

Julia B. Nehmann, Sarah Kajari-Schröder, Detlef W. Bahnemann. Analysis methods for meso- and macroporous silicon etching baths. *Nanoscale Res. Lett.* **2012**, *7*, 398.

Julia B. Nehmann, Nicole Ehrmann, Rolf Reineke-Koch, Detlef W. Bahnemann. Aluminum-doped zinc oxide sol-gel thin films: Influence of the sol's water content on the resistivity. *Thin Solid Films* **2014**, *556*, 168-173.

POSTERS AT NATIONAL AND INTERNATIONAL CONFERENCES

Julia B. Nehmann, Sarah Kajari-Schröder, Detlef W. Bahnemann. Analysis methods for meso- and macroporous silicon etching baths. In *Proceedings of the 16th Porous Silicon – Science and Technology (PSST)*, Malaga, Spain, March 2012.

Julia B. Nehmann, Sarah Kajari-Schröder, Detlef W. Bahnemann. Porosizierbad für PSI-Solarzellen: Analyse vn HF und Silicium mit IC. In *Proceedings of the 7th Conference über Ionenanalyse (CIA)*, Berlin, Germany, September 2013.

ACKNOWLEDGMENT

It is a pleasure to thank those who made this thesis possible. I owe my deepest gratitude to

… Prof. Dr. Detlef Bahnemann for many illuminating and informative discussions and his willingness to supervise this thesis.

… Prof. Dr. Rolf Brendel for making it possible to carry out this work in his institute and for the pleasant project meetings in the PSI project. Besides, for his willingness for being the co-supervisor.

… Prof. Dr. Carla Vogt for her willingness to complete the thesis committee.

… Dr. Sarah Kajari-Schröder for the many interesting meetings and discussions concerning “the chemical” and “the physical” point of view. Besides, for comprehensive reviewing of the manuscript. It was her spirit and enthusiasm that kept me motivated in challenging times.

… Dr. Martin Nese, Dr. Daniel N. Wright, Dr. Andreas Bentzen, and Dr. Erik Sauar for the warm recipience in the PSI project team and the congenial atmosphere during meetings and debriefings, occasionally accompanied by one or two glass of wine. The Renewable Energy Corporation (REC) for funding of the project.

… Renate Horbelt for opening the door to the PSI project to me.

… Bianca Gehring and Renate Winter for their assistance with the measurements, and especially Alwina Knorr for her contribution to our good work in the exciting and sometimes elaborate time of implementing the ion-chromatography system.

… Thomas Kolb, Werner Maßing, and Daniel Schwarzer from Metrohm for their uncomplicated and active support with test measurements and later on with all challenges concerning ion-chromatography. Their experience and suggestions cleared the way for the dissolved Si measurements in the PSI etching bath as being part of this thesis.

… Dr. Rolf Reineke-Koch, Dr. Nicole Ehrmann, Dr. Mircea Turcu, Catherin Gemmel, Christine Hein, Anja Hülsewig, Susanne Blankemeyer, Daniel Münster, Sascha Wolter, and Alexandra Pazidis for the pleasant atmosphere during lunchtime, in the office, and sometimes over coffee and cake.

… Verena Steckenreiter for her assistance with the preparation of the test items for the permeation experiment. In addition, her and Anja Nowack for distracting me from hydrofluoric acid with coffee and “girls’ matters” in ambitious phases of writing.

… Jan Hensen and Manuel Stratmann for the preparation of porous silicon samples and the numerous samples of the etching electrolyte. Sören Schäfer, Catherin Gemmel, and Sascha Wolter for exciting discussions about and insights into electrochemical etching processes that made considerable progress for this thesis. Besides, all of them for many diverting hours in the lab.

… all the colleagues at ISFH and TCI that I missed. It was and it is a great pleasure to work with you.

… my friends, my parents and my brother Alexander for the greatest support in all circumstances. I wouldn’t get here without your love. Besides, the love of my life, Sebastian, for his empathy, understanding, and his love in this turbulent time.

Thank you.

CURRICULUM VITAE

PERSONAL DATA

Name	Julia-Beatrix Nehmann
Date of birth	17th of September, 1983
Place of birth	Hanover
Nationality	German

EMPLOYMENT

Since 03/2010	Institute for Solar Energy Research Hamelin (ISFH) Research associate Photovoltaic Department, Workgroup Silicon Thin Films

EDUCATION

05/2009 - 11/2009	Diploma thesis at ISFH, Solar Thermal Department Workgroup Solar Thermal Materials
07/2007 - 01/2008	Study abroad semester, University of Wollongong, NSW, Australia
10/2004 - 12/2009	Studies of chemisty Gottfried Wilhelm Leibniz University of Hanover
09/2003 - 08/2004	Year of voluntary work in the environmental sector (FÖJ) Warmsen
1997 - 2003	Schiller-Gymnasium Hameln, Abitur